PROBING THE SOLUBILITY OF SELECTED NANOSCALE BUILDING BLOCKS USING MOLECULAR SIMULATION

By

Patrick Scott Redmill

Dissertation

Submitted to the Faculty of the

Graduate School of Vanderbilt University

in partial fulfillment of the requirements

for the degree of

DOCTOR OF PHILOPSOPHY

in

Chemical Engineering

December, 2008

Nashville, TN

Approved:

Peter T. Cummings

Clare McCabe

Scott Guelcher

Eugene LeBoeuf

M. Douglas LeVan

To Mom and Dad

SUPPORT LOCAL COLLEGE RADIO

WRVU 91.1 FM

ACKNOWLEDGEMENTS

This work has been possible through the financial support of the National Science Foundation. Additionally, the simulations in this work were done using the computational resources at NERSC and ACCRE.

I am grateful for the support, guidance, and patience I have received during my research from my advisors, Professor Peter T. Cummings and Clare McCabe. I would also like to thank the members of my Dissertation Committee for their time, valuable insights, and unique observations that they contributed to this work. Vanderbilt University, as a whole, deserves great thanks as well. I am very grateful for the exposure to some of the best educators in world that Vanderbilt provided. I truly consider Vanderbilt my academic home.

I would like to thank Dr. Alberto Striolo, who was absolutely instrumental in initiating me to this work. Shannon Capps is also due special thanks for all of her hard work (i.e. things I didn't want to do and passed off on a poor undergrad) while a student in the McCabe lab. Finally, I would like to thank my lab mates, in particular, Christina Payne, Peter Dyer, and Hugh Docherty. Without their daily perspective, humor, coffee breaks and lunch breaks, I would have killed somebody over all this.

TABLE OF CONTENTS

LIST OF TABLES

LIST OF FIGURES

Figure Page

CHAPTER I

INTRODUCTION

The interest in nanoscale engineered materials has been steadily increasing since Richard Feynman suggested at a 1959 talk to the American Physical Society that there is "plenty of room at the bottom", referring to the possibilities of nanoscale science [1], and has rapidly expanded in recent decades as more experimental tools that can characterize at the nanoscale have become available. The notion that an understanding of nanoscale interactions and the ability to manipulate those interactions to produce specific macroscopic physical qualities provided fresh inspiration to the scientific community and caught the attention of many outside of specific scientific disciplines.

Nanotechnology is an increasingly growing field; the percentage of goods sold incorporating nanotechnology has been estimated to increase from 0.1% in 2004 to 15% in 2014, representing a $2.6 trillion industry which will encompass 11% of the manufacturing workforce [2]. Currently, industry is benefiting from the renaissance of so-called "passive" nanotechnology, which implies the enhancement of existing materials via the simple addition of nanoparticles [3]. Common passive nanotechnology has resulted, for example, in significantly increased tensile properties of polymeric systems upon the addition of carbon nanotubes [4] and the enhanced flame retardancy characteristics of polypropylene when combined with montmorillonite particles [5].

"Active" nanotechnology is defined as applications that are typically built up from the nanoscale, as opposed to passive nanotechnology, which simply incorporates

nanoparticles into macroscale systems [3]. Defining systems on the nanoscale will result in a more sophisticated material, with a more distinct purpose. While the incorporation of nanomaterials in this fashion is at a much earlier stage than passive nanotechnology techniques, the large predicted growth in usage of nanotechnology is critically dependent on advances in active nanotechnology. While such a bottom-up approach seems radical, biological systems produce similarly detailed nanoscaled processes, via self-assembly, in order to carry out multitudes of biological processes [6]. Therefore, increasing knowledge of how biological systems assemble molecular machines and manipulate systems on the nanoscale should provide keys to the advancement of active nanoscience. Some strides in active nanoscience are already being realized, such as the discovery that fullerenes particles may be effective HIV inhibitors, where the particle has been shown to clog the protease inhibitor's active site, slowing the proliferation of the virus [7] or as a biological tag molecule for MRI imaging [8]. Synthetic nanoscale machines, such as gears, bearings, motors, pumps, and logic gates [9] have been proposed to influence nanoscale environments similar to how their macroscale counterparts effect large systems. Efforts towards developing nanoscale machines have already been realized, as evidenced by a successfully synthesized "nanocar", consisting of four C_{60} "wheels", alkynyl "axles", and a chassis that consists of fused aromatic rings [10].

To supplement the advancement of nanotechnology, an array of nanoparticles of varying size, shape, chemical and mechanical properties have been devised. Of the many classifications of nanoparticles, the fullerene family is one of the most studied and understood. Fullerene particles are carbon based and are comprised mostly of hexagonal graphene rings, much like graphite. What differentiates fullerenes from graphite is that

graphite has an effectively flat surface, while fullerenes exhibit a curved surface. The ability of the fullerene surface to curve results in the possibility of various nanoscaled geometric objects, or nanoscale building blocks (NBBs), such as spheres, tubes, cones, and horns [11]. Additionally, fullerenes have been shown to range from one nanometer to several nanometers in diameter and up to a millimeter in length [12]. Fullerenes have found a multitude of applications, particularly in their use in nanocomposites, such as incorporating fullerenes into polymer micelles that have potential as refined photovoltaic devices [13], in soft hydrogel polymers producing tunable and robust protein separators [14], and with poly(3-butylthiophene) to create high efficiency solar cells [15]. Beyond nanocomposites, fullerenes have been proposed as a next-generation logic gate [16] and as a delivery agent for therapeutics [17].

Quantum dots, colloidal gold, and hybrid inorganic-organic compounds are other types of nanoparticles that receive a significant degree of attention in the literature. Quantum dots are semi-conducting crystals composed of particles from periodic groups II-VI, III-V, or IV-VI and range from 2-10 nanometers in diameter [18]. Among other applications, quantum dots have shown potential as a fluorescent tag for sub-cellular structures in living organisms [19] and as a DNA sequence characterizing agents [20]. Gold nanoparticle suspensions, which can be as large as 75 nanometers in diameter [21], have also shown many potential applications. When coated with oligonucleotides, gold nanoparticles exhibit extraordinary stability in salt solutions and have therefore been classified as good candidates for protein interaction characterization [22]. Additionally, due to the relative ease in which organics can be fashioned on the surface in one, two, and three dimensions, the particles have been proposed as possible molecular electronic

devices [23]. Hybrid organic-inorganic nanoparticles generally consist of an inorganic constituent and an organic component, often maintaining the desirable materials properties of both groups [24]. The particles commonly exhibit inorganic constituents such as siloxanes [25], titanium, and aluminum [26]. Due to their highly ordered crystalline state, latex-based hybrid inorganic-organic particles have a very high refractive index, and therefore may prove useful for photonic applications [24]. Additionally, polymers grafted with hybrid inorganic-organic nanoparticles exhibit properties liquid crystals [27].

Given the multitudes of current and projected uses of nanoparticles, the manufacturing sector will undoubtedly be affected by the growing demand to produce these materials. Indeed, in 2001, the estimated production of all carbon-based nanoparticles was several hundred tons, whereas, by 2003, the production of carbon nanotubes alone was 900 tons [28]. So far, there are over 200 possible industrial fabrication techniques, practically all stemming from a so-called "top-down," or passive, approaches; meaning that the particles are created from macroscale synthesizing techniques [29]. Sophisticated "bottom-up" approaches are anticipated to increase the functionality of nanoparticles and are predicted to increase yield by several orders of magnitude by 2020 [29]. While the new innovations in materials that will be a result of heightened nanoparticle production is undeniably exciting, the growth in nanoparticle production will present the issue of occupational and environmental exposure. This is problematic, because the toxic effect for many nanoparticles is poorly understood, and mass production may have serious repercussions to workers in the manufacturing facility and the environment surrounding the facility. For many current production facilities,

information appearing on material data safety sheets (MSDS) for the nanoparticle in production or use is often substituted with the MSDS information for a bulk material of equivalent chemical composition, which is problematic as different isomeric forms of a particle may have different toxicological effects. Furthermore, detailed information regarding the size and chemical identity of nanoparticles can be difficult to obtain, as such information is often proprietary [30] or simply not known. These shortcomings highlight the fact that the growth in understanding of nanoparticles is being far outpaced by the production of new nanoparticle variants, which may result in unforeseen, negative environmental and toxic consequences.

In order to better understand the environmental and occupational implications of the looming increase in nanoparticle production, it is important to be familiar with existing literature regarding toxicology. Such reports provide insight into how to carry out the exhaustive studies required to satisfactorily characterize the toxic ramifications of the incorporation of nanotechnology into common consumer and commercial products. The current production of nanoparticles may already be exposing workers in manufacturing facilities and neighboring residents of the facility to unforeseen, deleterious chronic effects. Furthermore, significant increases in nanoparticle production, both in terms quantity and variety produced, practically guarantees occupational and environmental exposure. Once exposed to the environment, a potential toxin is capable of disrupting crucial cellular processes. This is possible, provided the toxin can traverse a very discriminating pathway, designed to supply water and nutrients to cells. Toxicology is the study of this path, and of the liklihood of a given compound being able to span it and disrupt cellular processes. Due to the highly varied nature and great potential of

customization of nanoparticles, both comprehensive experimental and rapid computational toxicology techniques will ultimately be required to sufficiently gauge the vast array of toxicological effects that will be introduced as new particles are introduced to the market.

Experimental toxicity is a proven means of discovering the effect of toxins on animal cells and the characterization to their route of disruption on cellular processes. There are two broad types of experimental toxicology: descriptive animal toxicology and mechanistic toxicology [31]. Many experimental toxicology efforts are so called "descriptive animal toxicity" tests. These studies observe the toxic effects of a material on animal test subjects on a dose per unit of body surface or mass basis. These studies are often applicable to humans, as humans commonly express similar toxicity reactions to that of laboratory test animals; however, humans are typically found to be a factor of 10 times more vulnerable to toxins than animals [31]. Therefore, such a technique is not an absolute means of determining human toxicity. Such studies have been standardized to produce toxicity parameters such as the median lethal dose (LD_{50}), the existence of skin or eye irritation (Draize test [32]), irregularities in reproduction, and persistent genetic alterations of several generations.

While descriptive animal toxicity can be very helpful in diagnosing the ultimate toxicity of a compound, a more detailed account of how the toxin travels from the environment to the point of disruption of cellular processes can often provide a more sophisticated means of limiting the toxic potential of the compound. The directed study of the route that a toxin enters an organism, how it interacts with target molecules, how it exerts the harmful effect, and how the organism adapts to the resulting damage is know

as “mechanistic toxicology [31].” Figure 1.1 shows a mechanistic toxicity study of the pesticide isofenphos in UK livestock [33].

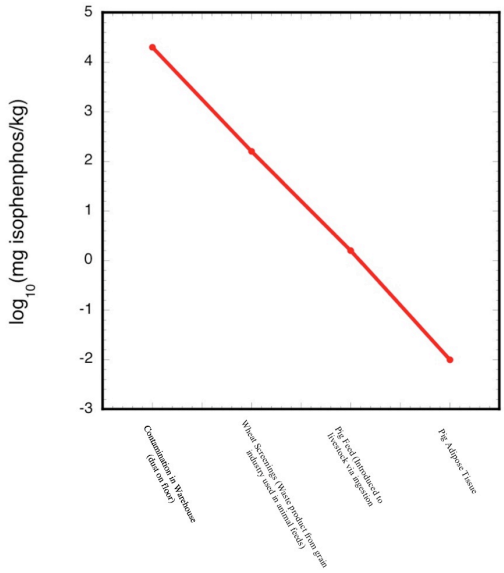

Figure 1.1: Exposure levels of isofenphos in UK livestock contamination [33]

Figure 1.1 shows the concentration of isophenphos at various levels of exposure, from the warehouse floor to the tissue of the livestock. This study highlights the various industrial and physiological barriers to isophenphos interrupting cellular processes. The figure shows that while the elimination of the toxin at each step is quite significant, even a minute exposure on the extracellular level can lead to serious, adverse effects.

The beginning of the route is typically characterized by the toxin being absorbed from the point of exposure (skin, lungs, stomach lining, etc.) into the circulatory system. At this point, the toxin may be reduced or eliminated from the organism via several barriers, such as the GI mucosal cells, liver, or lungs. An example of such an elimination would be the oxidation of ethanol by alcohol dehydrogenase [34]. If the toxin is not eliminated from the circulatory system, then it will likely be distributed into the tissue of

physiological systems. For the UK livestock case, it is shown that very little of the initial isofenphos exposure actually manifests into the tissue of the animal, as the concentration in the tissue is six magnitudes lower than the initial industrial concentration. The elimination of the majority of the pesticide present in the feed is likely due to the pesticide preferentially partitioning to the aqueous phase, as opposed to the organic phase, where cells reside. Generally speaking, a lipid bilayer separates the tissue (organic) phase from the water phase, therefore, the ability of a particle to partition and migrate through a lipid bilayer will determine if the toxin will accumulate in the tissue. Thermodynamic driving forces typically guide this process, as the toxin generally has an energetically favorable phase in which to partition. A popular gauge for this is the *octanol-water partition coefficient* ($K_{o/w}$) and is simply the ratio of the mole fractions of a given solute in octanol compared to its mole fraction in water. This is an apt description of the water/tissue environment due to the physical similarities between octanol and the lipids membranes covering tissue, namely a polar head with a non-polar tail. $K_{o/w}$ can be directly related the difference between the Gibbs free energy of solvation (ΔG^{solv}) between the phases when the particle is sparingly soluble in each solvent.

When present in tissue, the toxin may then have access to the intracellular space of the cell. There are a variety of routes that toxins may take to traverse the cellular membrane, which separates the intracellular and extracellular mediums. One such route is for the toxin to exploit voltage gated channels, intended for the transport of ions across the membrane. Furthermore, toxins gain access to the intracellular medium by binding to molecules in the extracellular environment that naturally target the cell, such as chloroquine binding to melanin, which ultimately results in retinal damage [35]. Once

inside the cell, toxins can hinder a variety of cellular processes, such as DNA transcription [36], signal transduction [37], or ATP synthesis [38].

The potential toxic impact of nanoparticles is a hotly debated topic, as a consensus answer has yet to be reached on the subject. In one study, it was found that juvenile largemouth bass in the presence of C_{60} suffered a 17-fold increase in brain tissue damage after just 48 hours of exposure [39]. It is believed that the toxic behavior of C_{60} is due to its tendency to produce free radicals in water, which in turn damage the lipids of the cellular membranes and ultimately destroy the cell. Theoretical studies, showing that C_{60} can bind to and deform DNA segments and in turn potentially hindering the ability of DNA to repair itself and replicate [40], further suggest the toxic potential of C_{60}. Another claim suggests that the C_{60} molecule exhibits no acute or subacute toxicity [41]. In this study, bare C_{60} did not have any observable effect on the proliferation rate of keratinocytes and fibroblasts. Additionally, *in vivo* tests in Swiss mice show no signs of lethality, toxicity, or growth inhibition [41]. The same study finds that a family of pyrrolidinium salt derivatives of C_{60} generally shows no signs of toxicity, although one compound did exhibit relatively acute toxicity on ddY female mice (a genetic strain with superior growth and reproductive performance). Fullerenes have even been proclaimed as possible antioxidants; it was found that C_{60} and carboxylic acid C_{60} derivatives actually bind with free radicals, which normally induce lipid peroxidation [42]. Other studies claim that fullerene toxicity is greatly dependent on functionalization [43, 44] and particle geometry [45]. One argument is that carbon based particles with small aspect ratios, such as carbon black, are more toxic than large aspect ratio materials, such as carbon nanotubes, because these materials contain a higher density of reactive dangling

bonds, which interfere with active sites on the cell surface [45]. However, Magrez et al. have shown that water-soluble fullerenes, typically functionalized with carbornyl, carboxyl, or hydroxyl groups, tend to show a decreased toxicity, as they do not induce cell death or activation of lymphocytes. These finding are in contrast with toxicity studies of undecorated carbon nanotubes [43].

These preliminary toxicology studies have alerted the scientific community to the possible toxicological ramifications of introducing nanoparticles into biological systems. Since these nanoparticles are relatively new and, their modifiable nature allows almost a limitless number of arrangements, we are presented with the problem of having a group of potentially biologically relevant compounds whose toxicological identity we know little about. To understand this problem more clearly, it is important to recognize the steps involved in how nanoparticles migrate through physiological systems. Furthermore, methodical study of each step in reference to a particular nanoparticle should help elucidate the particle's toxic potential and help the scientific community make informed decisions about their usage in biological systems and the environment.

Given the increasing rate at which new chemicals are being developed due to combinatorial chemistry and high throughput chemistry techniques, traditional, experimental toxicity analysis methods may be too costly or time consuming to be practical. Computational toxicology analysis techniques are becoming very important, as they often prove to be fast and inexpensive, while offering a high degree of accuracy. Two computational approaches have been developed that predict high-level toxicological parameters such as LD_{50} and maximum tolerated dose: so-called "knowledge based" and "statistically based" approaches.

Knowledge based programs include the DEREK [46], OncoLogic [46], and HazardExpert [47] codes. The term "knowledge based" refers to rules that are defined between molecular descriptors, such as structure and biological activity, and qualitative toxic potential, which is mined from expert opinion and toxicological data. Such a methodology provides a quick means of assigning toxic potential to novel compounds. Several studies [48-50] have shown that such a methodology has a relatively high success rate for identifying mutagens in a library of compounds.

Statistical methods, on the other hand, fit various calculated parameters and structural connectivity, via a statistical analysis, to a mathematical relationship, which can ascribe toxicity reports to various compounds relatively generically. This approach is often able to assign quantitative results regarding toxicity. Such methods have been shown to exhibit 68% accuracy in predicting the probability of a compound to be carcinogenic [51, 52]. Examples of programs that utilize such are methodology are TopCat [53] and MultiCase [54].

At present, the datasets in computational toxicology programs are insufficient to accurately predict specific toxicology parameters for any given compound. As a result, there is an interest in methodologies that can accurately and cheaply predict thermodynamic parameters that influence the toxic potential of a compound, without the reliance on preexisting, detailed toxicological experimental data. Group-contribution techniques, such as UNIFAC [55], and quantitative structure property relationship analyses (QSPR) [56] have been applied to to the calculation of $logK_{O/W}$ [57, 58], infinite dilution activity coefficients (γ^{∞}) [59, 60], and blood barrier partition coefficients (*logBB)* [61]. While not an absolute indicator of toxicity, such parameters are commonly

acknowledged to directly contribute to toxic potential, and these methods have shown a high degree of accuracy in estimating thermodynamic parameters over a large range of components [62], and complex systems, such as ionic liquids [63, 64].

While such methods are also dependent on experimental data, they are more established than many dedicated computational knowledge statistically based toxicology techniques. This data will be extendable to systems of many different solvents and perhaps to nanoparticle systems with some degree of accuracy. However, this will likely not be the case for unusual, or even hypothetical particles that may be synthesized in the future, as the existing datasets will likely not contain parameters for inorganic molecules. This is typical for many nanoparticles, as experimental phase equilibria measurements may be difficult to obtain due to very unusual molecular interactions. Alternatively, phase equilibria data may be missing due simply to the novelty of the compounds, as experiments may have yet to be performed on the systems of interest. Molecular simulation offers the unique opportunity to study the phase equilibria of novel, or even hypothetical nanoparticle systems. To combat the shortcomings of a lack of experimental data for nanoparticle systems, several predictive, computational techniques may be used to calculate solubility parameters of nanoparticles relative to toxicity studies. For instance, molecular dynamics (MD) simulation have been used in conjunction with thermodynamic integration (TI) to calculate the ΔG^{solv} for alkanes [65], aromatics [66], and amines [67]. In turn, ΔG^{solv} values for a solute in aqueous and organic phases can be used to find organic-water partition coefficients. Furthermore, the Gibbs free energy of transfer ($G(z)$) and the one-dimensional diffusivity function ($D(z)$) of simple molecules, such as benzene [68], and even complicated fullerenes [69, 70] have been calculated in

heterogeneous bilayers using MD and a potential of mean force (PMF) analysis. Alternative options include the parameterization of UNIFAC binary interaction parameters using an *ab initio* "supermolecule" approach [71], which may be used in an UNIFAC analysis to find solvation parameters. This approach has been successfully applied to find γ^{∞} for aqueous alcohol, ketone [72], and aldehyde [73] systems.

This work consists of three main thrusts, which contributes to the effort of efficient toxicology screening techniques for nanoparticle systems. One main objective of this work is the calculation of ΔG^{solv} for a variety of fullerenes in octanol and water using MD and TI. A major emphasis of this study is the impact of fullerene geometry on ΔG^{solv}. Thermodynamic integration studies of seven different fullerenes of varying sizes, aspect ratios, and cavity size have been conducted for both water and n-octanol solvents. These results agree with the current consensus that fullerenes are remarkably hydrophobic [74] and organophilic [75]. Furthermore, the results show that the fullerene particle geometry indeed has a significant effect on solubility in aqueous an organic phases, in particular, that larger fullerenes tend to be more hydrophobic/organophilic than smaller varieties. It is also observed that uncapped nanotubes, where internal wetability is possible, results in a significant hydrophobic shift relative to uncapped carbon nanotubes.

Secondly, this work quantitatively determines the effects of adding hydrophilic groups, to the bare nanoparticle unit, on the ΔG^{solv} in water. The particles of interest are the water-soluble $C_{60}(OH)_{32}$, H-POSS, F-POSS, and OH-POSS. In most cases, no particle geometry or force field information are available; therefore, such data is determined using density functional theory calculations. The resulting parameters are subsequently used in a thermodynamic integration analysis and values for ΔG^{solv} in water. The results

reflect the common perception that $C_{60}(OH)_{32}$ is hydrophilic [76, 77]. Additionally, the hydrophilic shift that could be expected from H-POSS to OH-POSS is noted in these calculations.

This work also gauges the practicability of using the group contribution method, UNIFAC, in terms of calculating $K_{O/W}$ for a variety of nanoparticle systems. As UNIFAC parameters are often not available for inorganic molecules, such as POSS, *ab initio* "supermolecule" calculations were performed to obtain needed binary interaction parameters. It will be shown that while infinitely dilute activity coefficients (γ^{∞}) from UNIFAC analyses may be artificially high due to very stong, negative solute-solute interactions, partitioning calculations cancel these effects, leading to reasonable estimations of $\log K_{O/W}$. Furthermore, functionalizing the nanoparticles with hydrophilic groups results in a hydrophilic shift from the bare unit, which corresponds to the shift observed for water-soluble nanoparticles in the TI study.

Finally, the partitioning of C_{60} and H-POSS in heterogenous lipid bilayers has been evaluated using molecular dynamics simulations and potential of mean force (PMF) calculations in a DPPC bilayer. This study calculated $\Delta G(z)$, which describes the energetic barriers to partitioning into the heterogeneous bilayer at varying depths from the bilayer center. These barriers are related to particle size, orientation, and particle/lipid interactions. The results indicate that C_{60} will likely partition into the bilayer phase, whereas the H-POSS encounters a large energy barrier at the bilayer/water interface, suggesting that the partitioning of H-POSS into the organic phase relatively low.

References

1. Hochella, M.F., *There's plenty of room at the bottom: Nanoscience in geochemistry*. Geochimica Et Cosmochimica Acta, 2002. **66**(5): p. 735-743.

2. Norden, M.M., Allard, K., Tinker, Nathen, M., Mark, K., J., Mills, S., and Paull, P., *The Nanotech Report 2004*. Investment Overview and Market Research for Nanotechnology. Vol. 1. 2004.

3. Tour, J.M., *Nanotechnology: The Passive, Active, and Hybrid Sides-Gauging the Investment Landscape from the Technology Perspective*. Nanotechnology Law and Business, 2007. **4**(3): p. 361-373.

4. Ajayan, P.M., and Tour, J.M., *Nanotube composities*. Nature, 2007. **447**: p. 1066-1068.
5. Qin, H., Zhang, S., Zhoa, C., Hu, G., and Yang, M., *Flame retardant mechanism of polymer/clay nanocomposites based on polypropylene*. Polymer, 2005. **46**(19): p. 8386 -8395.

6. Gazit, E., *NanoBioTechnology: BioInspired Devices and Materials of the Future*. 2008, Totowa, NJ: Human Press.

7. Osawa, E., *Recent progress in the developmental research of fullerenes and nanotubes*. Contemporary Studies in Advanced Materials and Processes, 2003. **413**: p. 1-6.

8. Toth, E., Bolskar, R. D., Borel, A., Gonzalez, G., Helm, L.,Merbach, A. E.,Sitharaman, B., Wilson, L. J, *Water-soluble gadofullerenes: Toward high-relaxivity, pH-responsive MRI contrast agents*. Journal of the American Chemical Society, 2005. **127**(2): p. 799-805.

9. Cagin, T., et al., *Molecular mechanics and molecular dynamics analysis of Drexler-Merkle gears and neon pump*. Nanotechnology, 1998. **9**(3): p. 143-152.

10. Shirai, Y., Osgood, A., J, Zhoa, Y., Yao, Y., S., Lionel, Y., Hanbiao, Y-H., Chiu, A., Lawrence, B., Sasaki, T., Morin, J-F., Guerrero, J.M., Kelley, K.F., and Tour, J.M., *Surface-Rolling Molecules*. J. Am. Chem. Soc., 2006. **128**(14): p. 4854-4864.

11. Inagaki, M., K. Kaneko, and T. Nishizawa, *Nanocarbons - recent research in Japan*. Carbon, 2004. **42**(8-9): p. 1401-1417.

12. Yakobson, M., and Smalley, R.E., *Fullerene Nanotubes: C1,000,000 and Beyond*. American Scientist, 1997. **85**(4): p. 324-327.

13. Wang, X. S., Metanawin, T., Zheng, X. Y., Wang, P. Y., Ali, M., Vernon, D.., *Structure-defined C-60/polymer colloids supramolecular nanocomposites in water.* Langmuir, 2008. **24**(17): p. 9230-9232.

14. Makamba, H., Huang, J. W., Chen, H. H., Chen, S. H., *Photopatterning of tough single-walled carbon nanotube composites in microfluidic channels and their application in gel-free separations.* Electrophoresis, 2008. **29**(12): p. 2458-2465.

15. Xin, H., F.S. Kim, and S.A. Jenekhe, *Highly efficient solar cells based on poly(3-butylthiophene) nanowires*. Journal of the American Chemical Society, 2008. **130**(16): p. 5424.

16. Colbert, D.T., and Smalley, R.E., *Fullerene nanotubes for molecular electronics*. Nanotechnology Law and Business, 1999. **17**(2): p. 46-50.

17. Klumpp, C., Kostarelos, K., Prato, M., and Bianco, A., *Functionalized carbon nanotubes as emerging nanovectors for the delivery of therapeutics*. Biochimica et Biophysica Acta, 2006. **1758**(3): p. 404.

18. Amiot, C.L., Xu, S., Liang, S., Pan, L., and Zhoa, J.X., *Near-Infrared Fluorescent Materials for Sensing of Biological Targets*. Sensors and Actuators B-Chemical, 2008. **8**: p. 3082-3105.

19. Derfus, A.M., Chan, W.C.W., and Bhatia, S.N., *Intracellular Delivery of Quantum Dots for Live Cell Labeling and Organelle Tracking*. Advanced Materials, 2004. **16**(12): p. 961-966.

20. Parak, W.J., *Biological applications of quantum dots*. European Biophysics Journal, 2003. **32**(3): p. 176.

21. Chithrani, B.D., Ghazani, A.A. and Chan, W.C.W., *Determining the Size and Shape Dependence of Gold Nanoparticle Uptake into Mammalian Cells*. Nano Letters. **6**(4): p. 662 -668.

22. Cao, Y.C., Jin, R., Nam, J-M., Thaxton, C., Shad, M.*, Chad A., *Raman Dye-Labeled Nanoparticle Probes for Proteins*. J. Am. Chem. Soc., 2003. **125**(48): p. 14676 -14677.

23. Rao, C.N.R., et al., *Metal nanoparticles and their assemblies*. Chemical Society Reviews, 2000. **29**(1): p. 27-35.

24. Gutmann, J.S., and Jonas, U., *Organic-Inorganic Hybrid Materials*. Supramolecular Architectures.

25. Mascia, L. and A. Kioul, *Influence of Siloxane Composition and Morphology on Properties of Polyimide-Silica Hybrids*. Polymer, 1995. **36**(19): p. 3649-3659.

26. Yamada, N., I. Yoshinaga, and S. Katayama, *Synthesis and dynamic mechanical behaviour of inorganic-organic hybrids containing various inorganic components*. Journal of Materials Chemistry, 1997. **7**(8): p. 1491-1495.

27. Provatas, A., Luft, M., Mu, J.C., White, A.H., Matisons, J.G., Skelton, B.W., *Silsesquioxanes: Part I: A key intermediate in the building of molecular composite materials*. Journal of Organometallic Chemistry, 1998. **565**(1-2): p. 159-163.

28. Kleiner, K., and Hogan, J., *How safe is nanotech? As the nanotech revolution gathers paces, few are giving a thought to the impact on health and environment*. New Scientist, 2003. **177**(2388): p. 14-15.

29. *Nanoscience and nanotechnologies: opportunities and uncertainties*. 2004, The Royal Society and The Royal Academy of Engineering: London.

30. Mulhall, D., *Nanotechnology and the Environment: Applications and Implications*, ed. B. Karn, Masciangioli, Tina, Zhang, Wei-xian, Colvin, Vicki, and Alivisatos. 2005, American Chemical Society.

31. Klaassen, C.D., *Casarett & Doull's Toxicology: The Basic Science of Poisons*. 1996: McGraw Hill.

32. Gelatt, K.N., *Textbook of Veterinary Ophthalmology*. 1981: Lea and Febiger.

33. Shaw, I.C., and Chadwick, J., *Principles of Environmental Toxicology*. 1998, London: Taylor and Francis.

34. Lim, R.T., Gentry, R.T., and Ito, D., *First-pass metabolism of ethanol is predominantly gastric*. Alcohol Clin Exp Res, 1993. **17**: p. 1337-1344.

35. Larsson, B.S., *Interaction between chemicals and melanin*. Pigment Cell Res, 1993. **6**: p. 127-133.

36. Heuchel, R., Radtke, F., and Georgiev, O., *The transcription factor MTF-1 is essential for basal and heavy metal-induced metallothionein gene expression*. EMBO J, 1994. **13**: p. 2870-2875.

37. Meyer, M., Schreck, R., Baeuerle, P.A., *H2O and antioxidants have opposite effects on activation of NF-KB and AP-1 in intact cells: AP-1 as secondary antioxidant-responsive factor*. EMBO J, 1993. **12**: p. 2005-2015.

38. Moreland, D.E., *Introduction to Biochemical Toxicology*, ed. a.L.P.E. Hodson E. 1994.

39. Eva, O., *Manufactured Nanomaterials (Fullerenes, C60) Induce Oxidative Stress in the Brain of Juvenile Largemouth Bass*. Environmental Health Perspectives, 2004. **112**(10): p. 1058-1062.

40. Zhao, X., Striolo, A., and Cummings, P.T., *C60 Binds to and Deforms Nucleotides*. Biophysical Journal, 2005. **89**(6): p. 3856–3862.

41. Da Ros, T., and Prato, M., *Medicinal Chemistry with fullerenes and fullerene derivatives*. Chem. Commun., 1999(8): p. 663-669.

42. Wang, C.I., Tai, L.A., Lee, D.D., Kanakamma, P.P., Shen, C.K-F., Luh, T-Y., Cheng, C-H., and Hwang, K.C., *c60 and Water-Soluble Fullerene Derivatives as Antioxidants Against Radical-Initiated Lipid Peroxidation*. J. Med. Chem., 1999. **42**(22): p. 4614-4620.

43. Dumortier, H., Lacotte, S., Pastorin, G., Marega, R., Wu, W., Bonifazi, D., Briand, J.-P., Prato, M., Muller, S., and Bianco, A., *Functionalized Carbon Nanotubes Are Non-Cytotoxic and Preserve the Functionality of Primary Immune Cells*. Nano Letters, 2006. **6**(7): p. 1522-1528.

44. Sayes, C.M., Fortner, J.D., Guo, W., Lyon, D., Boyd, A.M., Ausman, K.D., Tao, Y.J., Sitharaman, B., Wilson, L.J., Hughes, J.B., West, J.L., and Colvin, V.L., *The Differential Cytotoxicity of Water-Soluble Fullerenes*. Nano Letters, 2004. **4**(10): p. 1881 -1887.

45. Magrez, A., Kasas, S., Salicio, V., Pasquier, N., Seo, J.W., Celio, M., Catsicas, S., Schwaller, B., and Forro, L.,, *Cellular Toxicity of Carbon-Based Nanomaterials*. Nano Letters, 2006. **6**(6): p. 1121-1125.

46. Lhasa, l., *derek*, Lhasa limited: Leeds, UK.

47. Compudrug, *HazardExpert*, Compudrug.

48. Greene, N., Judson, P.N., Langowski, J.J., and Marchant, C.A., *Knowledge-based expert systems for toxicity prediction: DEREK, StAR and METEOR, SAR, QSAR*. Environ. Res., 1998. **10**: p. 299-314.

49. Ridings, J.E., Barratt, M.D., Cary, R., Earnshaw, C.G., Eggington, C.E., Ellis, M.K.,Judson, P.N., Langowski, J.J., Merchant, C.A., Payne, M.P., Watson, W.P., andYih, T.D., *Computer prediction of possible toxic action from chemical structure: an update on the DEREK system*. Toxicology, 1996. **106**: p. 267-279.

50. Sanderson, D.M., and Earnshaw, C.G., *The DEREK system*. Hum. Exp. Toxicol., 1991. **10**: p. 261-273.

51. Rosenkranz, H.S., and Klopman, G., *Prediction of the carcinogenicity in rodents of chemicals currently being tested by te US National Toxicology Program: structure-activity correlation*. Mutagenesis, 1990. **5**: p. 425-432.
52. Enslein, K., Blake, B.W., and Borgstedt, H.H.,, *Prediction of probability of carcinogenicity for a set of ongoing NTL bioassays*. Mutagenesis, 1990. **5**: p. 305-306.

53. Accelrys, *TopCat*. 2008, Accelrys: San Diego, Ca.

54. Multicase, I., *MultiCase*. 2008, Multicase, Inc.: Beachwood, OH.

55. Fredenslund, A., R.L. Jones, and J.M. Prausnitz, *Group-Contribution Estimation of Activity-Coefficients in Nonideal Liquid-Mixtures*. Aiche Journal, 1975. **21**(6): p. 1086-1099.

56. Karelson, M., V.S. Lobanov, and A.R. Katritzky, *Quantum-chemical descriptors in QSAR/QSPR studies*. Chemical Reviews, 1996. **96**(3): p. 1027-1043.

57. Park, S.J. and J.M. Back, *Prediction of partition coefficients for some organic compounds using UNIFAC*. Journal of Industrial and Engineering Chemistry, 2000. **6**(2): p. 100-106.

58. Lu, G.N., et al., *Estimation of n-octanol/water partition coefficients of polycyclic aromatic hydrocarbons by quantum chemical descriptors*. Central European Journal of Chemistry, 2008. **6**(2): p. 310-318.

59. Voutsas, E.C. and D.P. Tassios, *Analysis of the UNIFAC-type group-contribution models at the highly dilute region .1. Limitations of the combinatorial and residual expressions*. Industrial & Engineering Chemistry Research, 1997. **36**(11): p. 4965-4972.

60. Giralt, F., Espinosa, G., Arenas, A., Ferre-Gine, J., Amat, L., Girones, X., Carbo-Dorca, R., Cohen, Y., *Estimation of infinite dilution activity coefficients of organic compounds in water with neural classifiers*. Aiche Journal, 2004. **50**(6): p. 1315-1343.

61. Hou, T.J. and X.J. Xu, *ADME evaluation in drug discovery. 3. Modeling blood-brain barrier partitioning using simple molecular descriptors*. Journal of Chemical Information and Computer Sciences, 2003. **43**(6): p. 2137-2152.

62. Gmehling, J., J.D. Li, and M. Schiller, *A Modified Unifac Model .2. Present Parameter Matrix and Results for Different Thermodynamic Properties*. Industrial & Engineering Chemistry Research, 1993. **32**(1): p. 178-193.

63. Kato, R. and J. Gmehling, *Systems with ionic liquids: Measurement of VLE and gamma(infinity) data and prediction of their thermodynamic behavior using original UNIFAC, mod. UNIFAC(Do) and COSMO-RS(O1)*. Journal of Chemical Thermodynamics, 2005. **37**(6): p. 603-619.

64. Katritzky, A. R., Kuanar, M., Stoyanova-Slavova, I. B., Slavov, S. H., Dobchev, D. A., Karelson, M., Acree, W. E., *Quantitative structure-property relationship studies on Ostwald solubility and partitioncoefficients of organic solutes in ionic liquids*. Journal of Chemical and Engineering Data, 2008. **53**(5): p. 1085-1092.

65. Wescott, J.T., L.R. Fisher, and S. Hanna, *Use of thermodynamic integration to calculate the hydration free energies of n-alkanes*. Journal of Chemical Physics, 2002. **116**(6): p. 2361-2369.

66. Denti, T. Z. M., Beutler, T. C., vanGunsteren, W. F., Diederich, F., *Computation of Gibbs free energies of hydration for simple aromatic molecules: A comparative study using Monte Carlo and molecular dynamics computer simulation techniques*. Journal of Physical Chemistry, 1996. **100**(10): p. 4256-4260.

67. Wan, S.Z., R.H. Stote, and M. Karplus, *Calculation of the aqueous solvation energy and entropy, as well as free energy, of simple polar solutes*. Journal of Chemical Physics, 2004. **121**(19): p. 9539-9548.

68. Bemporad, D., Luttmann, C. and Essex, J.W., *Behaviour of small solutes and large drugs in a lipid bilayer from computer simulations*. BBA-Biomembranes, 2005. **1718**(1-2): p. 1-21.

69. Qiao, R., Roberts, A.P., Mount, A.S., and Klaine, S.J., *Translocation of C60 and Its Derivatives Across a Lipid Bilayer*. Nano Letters. **7**(3): p. 614-619.

70. Bedrov, D., Smith, G.D., Davande, H., and Li, L., *Passive Transport of C60 Fullerenes through a Lipid Membrane: A Molecular Simulation Study*. J. Phys. Chem., 2007. **112**(7): p. 2078-2084.

71. Lin, S.T. and S.I. Sandler, *Infinite dilution activity coefficients from ab initio solvation calculations*. Aiche Journal, 1999. **45**(12): p. 2606-2618.

72. Nanu, D.E. and T.W. De Loos, *Limiting activity coefficients of aqueous flavour systems at 298 K by the group contribution solvation (GCS) model*. Molecular Physics, 2004. **102**(3): p. 235-241.

73. Mendes, C.L.D., C.O. da Silva, and E.C. da Silva, *Parametrizing PCM to obtain solvation free energies from group contributions. 1*. Journal of Physical Chemistry A, 2006. **110**(11): p. 4034-4041.

74. Choudhury, N., *Dynamics of Water in the Hydration Shells of C60: Molecular Dynamics Simulation Using a Coarse Grained Model*. J. Phys. Chem. B., 2007. **111**(35): p. 10474-10480.

75. Bezmel'nitsyn, V.N., Eletskii, A V, and Okun, M V, *Fullerenes in Solution*. Physics-Uspeckt, 1998. **41**(11): p. 1091-1114.

76. Liu, W.-J., Jeng, U., Lin, T.-L., Lai, S,-H., Shih, M.C., Tsao, C.-S., Wanf, L.Y., Chiang, L.Y., and Sung, L.P., *Adsorption of doceahydroxylated-fullerene monolayers at the air-water interface*. Physica B, 2000. **2000**(283): p. 49-52.

77. Rincon, M.E., Hu, H., Campos, J., and Ruiz-Garcia, J., *Electrical and Optical Properties of Fullerenol Langmuir-Blodgett Films Deposited on Polyaniline Substrates*. J. Phys. Chem. B., 2003. **107**(17): p. 4111 -4117.

CHAPTER II

BACKGROUND & THEORY

General Methodology

Molecular dynamics (MD) is a tool used extensively in this work used to calculate the trajectories of a single solute molecule (the nanoparticle) in a system of either pure solvent (octanol or water) or in an explicit, hydrated phospholipid bilayer. This is achieved by simply applying Newton's laws of motion over a thermodynamically relevant timescale (femtoseconds-nanoseconds)

$$\mathbf{F}(\mathbf{q}) = m\frac{d^2\mathbf{q}}{dt^2} \tag{2.1}$$

where $\mathbf{F}$ is the force vector on each particle, m is the particle mass, $\mathbf{q}$ is the particle coordinate and t is time. Each molecular system is defined by an atomic force field that carries a set of bonded and non-bonded interactions that describes the potential between two or more atomistic sites. Equation 2.2 represents an inclusive list of all of the contributions to the atomistic force fields used in this work.

$$U(q) = \sum_{i=1}^{B} U_{bond} + \sum_{j=1}^{A} U_{angle} + \sum_{k=1}^{D} U_{dihedral} + \sum_{l=1}^{V} U_{vdW} + \sum_{m=1}^{E} U_{elec} \tag{2.2}$$

The first three terms in equation 2.2 describe intramolecular interactions, which means that they describe the interactions between atoms on the same molecule. The first term, U_{bond}, is the bond potential, which describes the energy associated with stretching the bond between two atoms. The second, U_{angle}, is the angle potential and describes the energy associated with flexing the angle about three consecutive atoms. The third term,

$U_{dihedral}$, is the torsional potential and represents the energy expended when four consecutive atoms are torqued.

The latter two terms in Equation 2.2 are intermolecular interaction terms, which for the most part describe interactions between atoms on differing molecules. All short-ranged non-bonded interactions for these studies, the van der Waals (vdW) interactions, are in the form of the 12-6 Lennard-Jones potential, defined by Equation 2.3

$$U(r) = 4\varepsilon_{ij}\left[\left(\frac{\sigma_{ij}}{r}\right)^{12} - \left(\frac{\sigma_{ij}}{r}\right)^{6}\right] \tag{2.3}$$

where ε_{ij} is the energetic well depth and σ_{ij} is the van der Waals radius of each atom. The long-ranged electrostatic (elec) interactions are modeled after a simple point-point Coulombic potential, where q_i represents the point charge for atom i in Coulombs and ε_0 is the permittivity of free space.

$$U(r) = \frac{1}{4\pi\varepsilon_0}\frac{q_i q_j}{r} \tag{2.4}$$

With the force field defined, we can determine the forces acting on the atoms and molecules, as shown in Equation 2.5.

$$\mathbf{F}(\mathbf{q}) = -\nabla U(\mathbf{q}) \tag{2.5}$$

Using Equations 2.2-2.5 and the Verlet leapfrog algorithm, Equation 2.1 can be integrated over discrete timesteps to produce the MD trajectories.

Thermodynamic integration and solubility calculations

Knowing the Gibbs free energy of solvation, ΔG^{solv}, for nanoparticles in octanol and water phases would greatly contribute to the understanding of nanoparticle partitioning in binary aqueous/organic systems. To understand how to manipulate the system in order to obtain ΔG^{solv}, an appropriate starting point is the isothermal-isobaric partition function (Δ) for a system containing one solute molecule in a solvent. This is the most convenient choice as the Gibbs free energy can be expressed in terms of this partition function [1], *viz.*

$$G = -k_b T \ln\left[\Delta(N,P,T)\right] \tag{2.6}$$

$$\Delta = \sum_U \sum_V \Omega(N,V,U) e^{-\beta U} e^{-\beta PV} \tag{2.7}$$

where Ω is the system degeneracy at a given number of particles (N), system volume (V), and system energy (U). For simplicity, we have considered the partition function in the case where the system has discrete energies and volumes. The partition function is defined by three constraints, namely system pressure (P), temperature (T), and the number of particles. Where $\beta = \frac{1}{k_B T}$, k_B is the Boltzmann constant, and h is Planck's constant. Describing he thermodynamic path of solvating a single nanoparticle in solution can be aided by adding an additional parameter, λ, into the partition function. Since the ΔG^{solv} is desired, the partition function should be modified by λ in the Hamiltonian, which describes solute-solvent interactions. If $U \rightarrow U(\lambda)$, and the derivative of Equation 2.7 is taken with respect to λ the following result is obtained.

$$\left(\frac{\partial G}{\partial \lambda}\right)_{N,P,T} = -\frac{1}{\beta}\frac{\partial}{\partial \lambda}\ln\Delta(N,P,T,\lambda) = -\frac{1}{\beta\Delta(N,P,T,\lambda)}\frac{\partial\Delta(N,P,T,\lambda)}{\partial\lambda}$$
$$= \frac{\sum_U\sum_V \Omega(N,V,U)\left(\frac{\partial U}{\partial\lambda}\right)e^{-\beta U(\lambda)}e^{-\beta PV}}{\sum_U\sum_V \Omega(N,V,U)e^{-\beta U(\lambda)}e^{-\beta PV}} = \left\langle\frac{\partial U}{\partial\lambda}\right\rangle_\lambda \tag{2.8}$$

This derivation shows that sampling the change in the Hamiltonian with respect to λ and averaging the result can appropriately calculate the derivative of the Gibbs free energy at a constant λ. We choose λ to be a coupling parameter for the solute-solvent interactions, so that when $\lambda = 0$ we have pure solvent and when $\lambda = 1$ the solute is fully coupled to the solvent; that is, $U(\lambda=1)$ includes the full solute-solvent interactions. Since the Hamiltonian is well defined by the selected force fields, the trajectories produced by the MD simulation can be easily sampled and $\left\langle\frac{\partial U}{\partial\lambda}\right\rangle_\lambda$ can be calculated. Finally, the ΔG^{solv} can be calculated by integrating over the thermodynamic path,

$$\Delta G^{solv} = \int_{\lambda=0}^{\lambda=1}\left(\frac{\partial G}{\partial\lambda}\right)_{N,P,T} d\lambda = \int_{\lambda=0}^{\lambda=1}\left\langle\frac{\partial U}{\partial\lambda}\right\rangle_\lambda d\lambda \tag{2.9}$$

where Equation 2.9 again shows that the boundaries of integration were chosen to be zero to one. This method for computing the ΔG^{solv} is known as thermodynamic integration (TI) [1]. With the theoretical framework for how ΔG^{solv} will be sampled via MD in place, the final hurdle in implementing the simulations is to explicitly embed λ into the system

Hamiltonian. The λ parameter is incorporated into the force fields in accordance with the boundaries ascribed to λ. That is, the solvent-solute interactions are zero when $\lambda = 0$ and the interactions are full at λ = 1.There are, however, technical details that must be addressed in order to make the simulations robust, efficient, and make the calculations as accurate as possible. One important detail of the simulations is that singularities be avoided; with softened parameters between the solvent and solute, there is a possibility that the potentials will tend towards infinity as the radius between atomistic sites approaches zero. Introducing λ into the van der Waals interaction in the following fashion eliminates such a problem [2].

$$U(r,\lambda) = 4\varepsilon_{ij}\lambda\left[\frac{1}{\left(\alpha(1-\lambda)^2+\left(\frac{\sigma_{ij}}{r}\right)^6\right)^2} - \frac{1}{\left(\alpha(1-\lambda)^2+\left(\frac{\sigma_{ij}}{r}\right)^6\right)}\right] \tag{2.10}$$

The extra parameters, α and n in Equation 2.10, are used to address singularity and accuracy issues. Generally speaking, a value of $n \geq 2$ is required, as a number less than this will have significant trajectory noise and the insertion of the solute molecule may not be gradual enough, resulting in inaccuracy in the calculation of ΔG^{solv}. The α parameter is a constant that is generally positive and less than unity. The selection of this parameter will directly effect the finite height of the potential as $r_{ij} \to 0$. For all simulations in this work, the commonly used values of $n = 2$ and $\alpha = 0.50$ were employed [2]. The application of these modified potentials is easily achieved by supplying tabulated short

ranged potentials to the MD code. Figure 2.1 illustrates the prototypical potential curve at various values of λ.

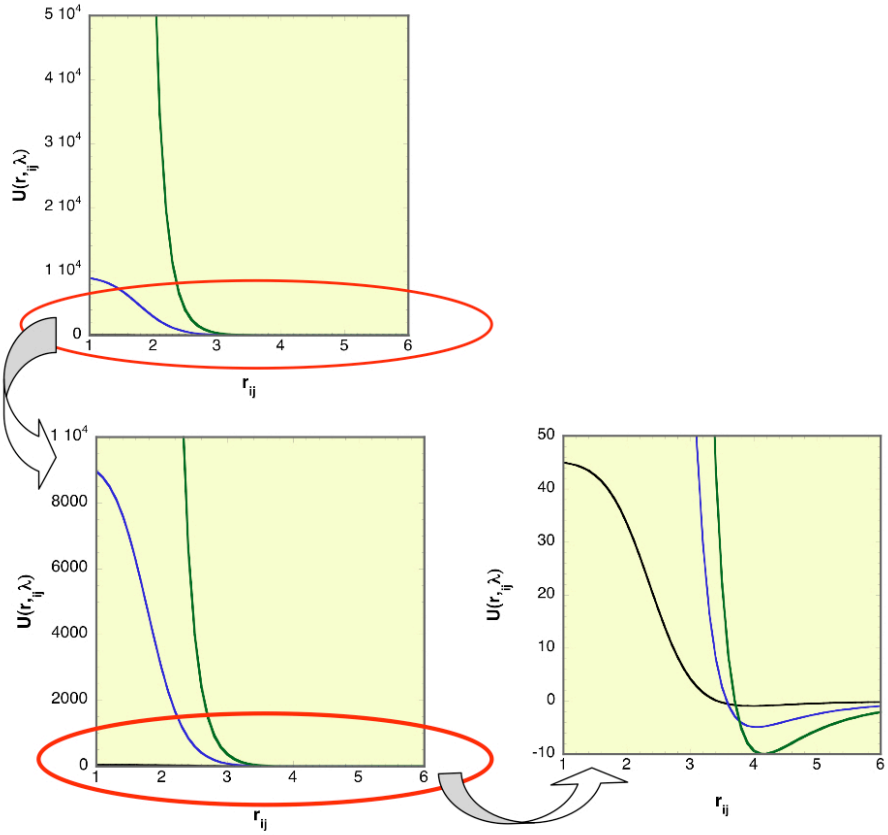

Figure 2.1: Prototypical softened van der Waals curves (soft, medium, hard)

Incorporating λ into the long-ranged Coulombic interactions without introducing singularities and noise errors is somewhat more difficult, as the electrostatic interactions cannot be presented in tabular form if periodic boundary conditions and Ewald summations are used in the simulations. Therefore, it is impossible to add the singularity eliminating term that is present in the denominator of the van der Waals interactions without modifying the DL_POLY [3] source code. As an alternative, the electrostatic potential has been modified by a simple λ^n coefficient, where again, $n = 2$.

$$U(r,\lambda) = \frac{\lambda^n q_i q_j}{4\pi\varepsilon_0 r} \tag{12.11}$$

While it is obvious that this form will not prevent singularities, as it is free to become undefined as $r_{ij} \rightarrow 0$, the solvation of the nanoparticle into solvent can be decoupled into two separate paths: one in which the nanoparticle has no partial charges and the van der Waals potentials are grown in and the other with the softened electrostatics and full van der Waals interactions. This approach effectively shields the electrostatically charged nanoparticle atomistic sites, eliminating singularities. This process can be expressed mathematically in the following fashion.

$$\Delta G^{solv} = \int_0^1 \left\langle \frac{\partial U}{\partial \lambda_1} \right\rangle_{vdw} d\lambda_1 + \int_0^1 \left\langle \frac{\partial U}{\partial \lambda_2} \right\rangle_{elec} d\lambda_2 \qquad (12.12)$$

As a result, the softened electrostatic potentials do not feature the plateaus at small r_{ij} as seen in the modified van der Waals potentials. However, since the repulsive van der Waals interactions are stronger than the electrostatic potentials at small r_{ij}, singularities are not encountered. Figure 2.2 shows typical softened electrostatic curves at various values of λ.

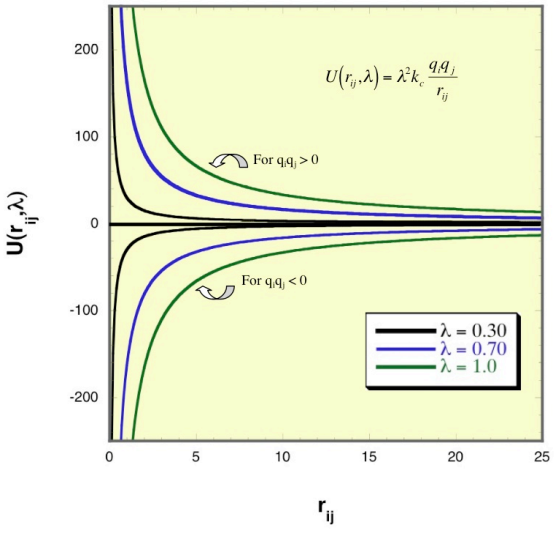

Figure 2.2: Prototype of softened electrostatic curves

Once softened non-bonded potentials are implemented, the MD trajectories are sampled and the derivative of the potentials with respect to λ is calculated. A symbolic derivation of Equations 2.10 and 2.11 yield the following, respectively

$$\left(\frac{\partial U}{\partial \lambda_1}\right)_{vdw} = 4\varepsilon_{ij}\lambda_1^n \left[\frac{4\alpha(1-\lambda_1)}{\left\{\left(\alpha(1-\lambda_1)+\left(\frac{\sigma_{ij}}{r}\right)^6\right)^3\right\}} - \frac{2(1-\lambda_1)}{\left\{\left(\alpha(1-\lambda_1)+\left(\frac{\sigma_{ij}}{r}\right)^6\right)^2\right\}} \right] + 4n\varepsilon_{ij}\lambda_1^{n-1} \left[\frac{1}{\left\{\alpha(1-\lambda_1)^2+\left(\frac{\sigma_{ij}}{r}\right)^6\right\}^2} - \frac{1}{\left\{\alpha(1-\lambda_1)^2+\left(\frac{\sigma_{ij}}{r}\right)^6\right\}} \right] \tag{2.13}$$

$$\left(\frac{\partial U}{\partial \lambda_2}\right)_{elec} = n\lambda_2^{n-1}\frac{q_i q_j}{4\pi\varepsilon_0 r} \tag{2.14}$$

It should be noted that both the short-ranged van der Waals and the long-ranged electrostatic thermodynamic integrations are not needed for all solutes. In this study, the POSS structures have partial charges assigned to the inner cage, so both steps are needed. However, unmodified fullerene structures have no partial charges, therefore, only the short ranged thermodynamic integration step is required.

To calculate the dynamic value of $\left(\frac{\partial U}{\partial \lambda_i}\right)$, the radial distance, *r*, between every solute-solvent atomic site interaction is calculated in a single time step. With the *r* values

and the equations above, the value of the derivative can be computed at that instant. Since there is appreciable statistical scatter, 100 samples are taken over a 1 nanosecond run without temperature scaling, ensuring that a well-converged average for the derivative is obtained. For each TI process a minimum of 10 separate MD runs are performed between $0.05 \leq \lambda_i \leq 1.0$ at discrete intervals of 0.05 or 0.10, depending on the softness of the potentials (note that with the form of U given in Equations 2.10 and 2.11, runs at $\lambda = 0$ yield no solute-solvent interactions, and since $\left(\frac{\partial U}{\partial \lambda_i}\right) = 0$ also, there is no contribution to ΔG^{solv}). Figure 2.3 is a protypical representation of a TI curve obtained from such calculations. The general behavior of positive derivative values at small λ and negative derivative values at large λ in the curve can be logically deduced from the force fields themselves, at low λ, the forces between atomistic sites are low and radii on the flat, positive potential curves in Figure 2.1 can be explored. However, at high values of λ, the radii are generally pushed out around σ_{ij}, resulting in negative derivative values. With a TI curve extending from $\lambda = 0$ to $\lambda = 1.0$, we can now compute the area under the curve, and determine ΔG^{solv}.

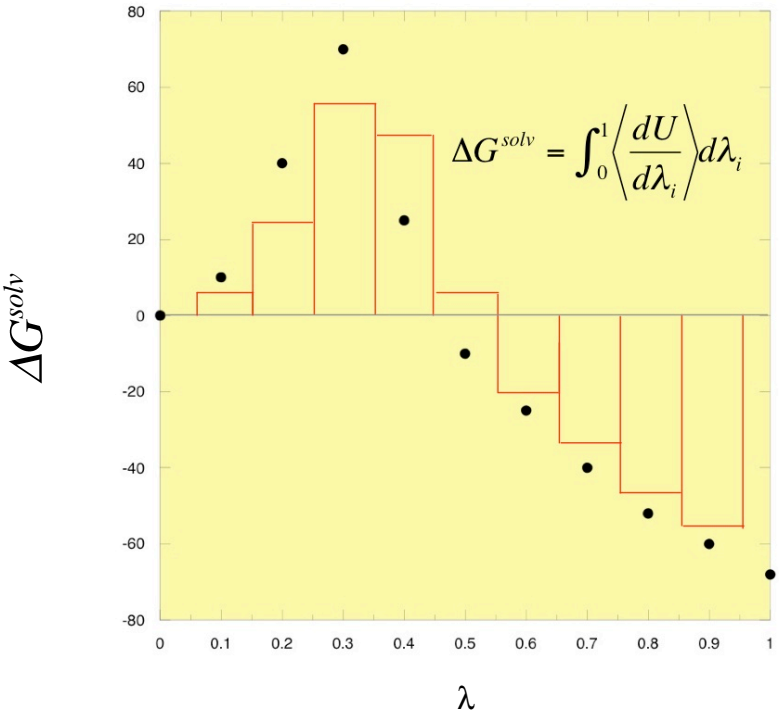

Figure 2.3: Prototypical TI curve

Although values of ΔG^{solv} for nanoparticles in solvents are useful quantities, the ultimate desire is to use these values to calculate common, industrially relevant, solubility parameters such as Henry's law constants ($H_{U,V}$) and $logK_{ow}$. Using common thermodynamic formulations, this can be accomplished. To find values for Henry's law coefficients from ΔG^{solv}, the Ben-Naim equation [4] is employed

$$H_{U,V} = \rho RTe^{\frac{\Delta G^{solv}}{RT}} \tag{2.15}$$

where H is the Henry's constant, U is the solute, V is the solvent, ρ is the molar density of the solvent, R is the universal gas constant and T is temperature.

Furthermore, since in the evaluation of K_{ow}, the octanol and water phases are in equilibrium, and we further assume that the solutes are in very dilute concentrations, the

fugacities of each phase are equal and each can be defined in terms of the Henry's law constant as given below

$$f_U^{oct} = f_U^{water} \tag{2.16}$$

$$f_U^{V} \rightarrow \lim_{x^V_U \rightarrow 0} H_{U,V} x^V_U \tag{2.17}$$

where f_U^V is the fugacity of the solute-solvent system and x^V_U is the mole fraction of solute in the solvent. Rearranging Equations 2.16 and 2.17, the definition of the octanol-partition coefficient can be derived in terms of Henry's law coefficients in octanol and water phases as,

$$K_{ow} = \frac{x_U^{octanol}}{x_U^{water}} = \frac{H_{U,water}}{H_{U,octanol}} \tag{2.18}$$

it is important to remember that this formulation of $K_{O/W}$ only holds if the solute is sparingly soluble in each solvent, otherwise the Equation 2.17 is invalidated and $K_{O/W}$ can no longer be expressed in terms of the ratio of Henry's constants. In the case of substantial solubility of the solute, the Krichevsky-Ilinskaya equation 2.17 [5], shown below, is required

$$f_U^V = H_{U,V} x_U^V e^{\frac{A\left(x_v^2 - 1\right)}{RT}} e^{\int_{P_U^{sat}}^{P} \frac{v_U^{\infty}}{RT} dP} \tag{2.19}$$

where $v_U\infty$ is the partial molar volume of the solute at the infinite dilution condition and A is the Margules expression constant. $v_U\infty$ can be calculated using liquid structure information from MD simulations by means of the Kirkwood-Buff solution theory [6], shown below

$$v = \frac{1 + \rho_2 (G_{22} - G_{12})}{\rho_1 + \rho_2 + \rho_1 \rho_2 (G_{11} - 2G_{12})} \tag{2.20}$$

where

$$G_{ij} = \int_0^\infty 4\pi r^2 \left[g_{ij}(r) - 1 \right] dr \tag{2.21}$$

and $g_{ij}(r)$ is the radial distribution function between particles i and j and ρ_i is the number density of particle i. Therefore, using radial distribution functions from dilute MD simulations, $v_U \infty$ can be obtained,and in turn, the pressure correction term in Equation 2.19 can be evaluated. Furthermore, if values of G_{ij} are obtained over the entire composition range of the binary system, the Margules constant can be fitted from fluctuation solution theory [7].

Calculation of UNIFAC Group-Contribution Parameters and Activity Coefficients

The ability to estimate $K_{O/W}$ for a variety of nanoparticles without performing expensive and costly experiments or simulations is very desirable. To achieve this end, an empirical correlation that ties various molecular attributes, such as interaction energy and molecular shape, could be very useful. The UNIFAC group-contribution method [8] is widely and effectively used to find activity coefficients. This is due in part, to the fact that UNIFAC parameters have been parameterized with a large library of binary and multiphase equilibria data, for many substances, including water, alcohol, chlorides, nitriles, ketones, and amides, among other compounds. Additionally, the UNIFAC method is widely applicable, as calculations are not dependent on parameterization of specific substances, but rather generic molecular "groups," from which specific systems can be built. As a result, calculations may be performed for which there is no prior experimental data. Due to these advantages, we have applied the UNIFAC group-contribution method to the

calculation of $K_{O/W}$ for C_{60} and POSS octa-functionalized with hydrogen ($(SiO_{1.5}H)_8$, designated H-POSS), and compared the results to TI studies to test the accuracy of the calculation. Additionally, the ability of UNIFAC to predict the hydrophilic shift observed in the TI studies of $C_{60}(OH)_{32}$, F-POSS ($(SiO_{1.5}F)_8$) and OH-POSS ($(SiO_{1.5}OH)_8$)from their respective bare particles was also tested.

The UNIFAC method divides the activity coefficient into a combinatorial and a residual portion, as seen in Equation 2.22

$$\ln \gamma_i = \ln \gamma_i^C + \ln \gamma_i^R \tag{2.22}$$

where, the combinatorial portion is defined as follows

$$\ln \gamma_i^C = \ln\left(\frac{\Phi_i}{x_i}\right) + \frac{z}{2} q_i \ln\left(\frac{\Theta_i}{\Phi_i}\right) + l_i - \frac{\Phi_i}{x_i}\sum_j x_j l_j \tag{2.23}$$

and the residual portion is defined as,

$$\ln \gamma_i^R = q_i\left[1 - \ln\left(\sum_j \Theta_j \tau_{ij}\right) - \sum_j \left(\frac{\Theta_j \tau_{ij}}{\sum_k \Theta_k \tau_{kj}}\right)\right] \tag{2.24}$$

in Equations 2.23 and 2.24, the parameter Φ_i is the segment fraction of component i and is a function of the mole fraction of i (x_i) and V_{wk}, the group volume.. Parameter Θ_i is the area fraction of group i and is a function of x_i and A_{wk}, the group area. Parameter z is the lattice coordination number, normally taken as a constant and $l = f(A_{wk}, V_{wk}, z)$. The τ_{ij} parameter is defined as,

$$\tau_{ji} = e^{-\left[\frac{(U_{ji} - U_{ii})}{RT}\right]} \tag{2.25}$$

where U_{ij} is the interaction energy due to short ranged and long ranged interactions between component i and component j [9]. U_{ij} has been defined as the minimum-energy of a molecular pair [10] and can be estimated using Sandler's *ab initio* "supermolecule" technique [11]. A "supermolecule" is defined as a minimum energy configuration of two or more molecules, where the interaction energy between the molecules can be calculated if the cluster energy and the energy of each isolated molecule in the cluster are known. The following equation calculates the interaction energy of a two-molecule cluster containing molecules A and B

$$U_{A\cdot B} = E_{A\cdot B}\{A\cdot B\} - E_A\{A\} - E_B\{B\} \tag{2.26}$$

where $E_{A\cdot B}\{A\cdot B\}$ is the *ab initio* energy of cluster $A\cdot B$ and E_i is the energy of molecule i, with the same conformation as molecule i in the cluster, in a vacuum. For the *ab initio* calculations to effectively account for dispersion interactions, a minimum of the MP2 level of theory is needed. The cluster geometries were optimized using a modest 6-31G basis set and the point energies used to determine U_{ij} used a 6-311++G** basis set. Due to the overlap of basis functions that are assigned to different molecules, the supermolecule calculations are subject to the so-called basis set superposition error (BSSE) [12]. This arises from the augmentation of orbitals on molecule A by basis functions allocated to molecule B, and vice versa. This results in an artificially high resolution for the orbital energies in question, which skews the results of Equation 2.26. To counteract this error, the full counterpoise method [13] was utilized. The counterpoise method cancels some of the error associated with BSSE by calculating the energy of

molecule A in vaccum with all the basis sets used in the $A \cdot B$ cluster and vice versa. These calculated energies replace the last two terms in Equation 2.26, resulting in the following equation

$$U_{A \cdot B} = E_{A \cdot B}\{A \cdot B\} - E_A\{A \cdot B\} - E_B\{A \cdot B\} \tag{2.27}$$

where $E_A\{A \cdot B\}$ is the energy of molecule *A* augmented by basis functions from both A and B and $E_B\{A \cdot B\}$ is the energy of molecule *B* augmented by basis functions from both *A* and B. These augmented energies should include the overlaps observed in the cluster calculation, therefore, subtracting these terms should effectively cancel the superposition error.

Intuitively, U_{ij} is the non-bonded interaction energy between like molecules. Additionally, it should be noted that $U_{ij} = U_{ji}$ The values of U_{ij} are widely available for most organic species of interest, however, supermolecule calculations were performed in order to determine the POSS binary interaction parameters.

The remaining parameters to evaluate are A_{wk} *and* V_{wk}, which are documented for a large number of molecular groups, including those appearing in the solvents of interest. However, for the solutes, the calculation of A_{wk} and V_{wk} will be necessary. The solvent accessible area for the solutes has been calculated via the Connolly technique [14] and the excluded volume is calculated by integrating over the space between adjacent Connolly surfaces.

To calculate the Connolly solvent accessible surface area, the solvent is modeled as a small sphere, or probe, with radius r_p that is rolled along the 2-dimensional profile at finite intervals along the molecule [15]. The total number of rotations the probe

experiences can then be mapped into the solvent accessible area of the molecule. The calculation of the excluded volume and Connoly solvent accessible area is present in some molecular visualization software packages, such as Chimera [16]. Figure 2.5 is a visual representation of the probe rolling along the surface of a molecule.

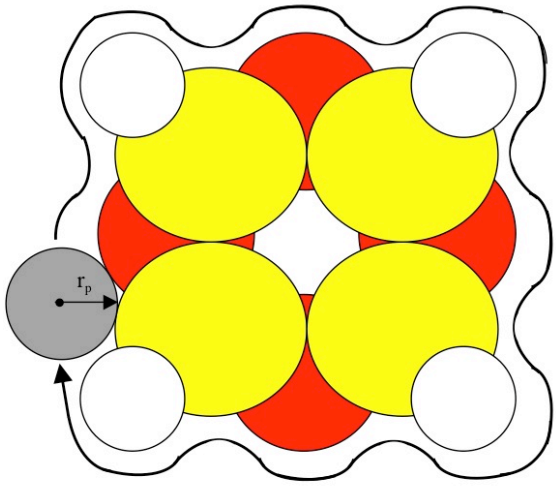

Figure 2.4: The probe path around the 2-D profile of a particle

Lipid Bilayer Perturbation Studies

Thermodynamic integration studies of nanoparticles in isotropic organic phases, such as octanol, do not take into the distinct barriers to partitioning along the heterogeneous axis of a structured system, such as a lipid bilayer. Such systems are ubiquitous in nature, and understanding how nanoparticle size, shape, and atomic composition are relate to solute partitioning in such systems is very important [17]. It is reasonable to hypothesize that, although the nanoparticle geometry may effect the partition coefficient due to differences in the amount of surface exposed to the solvent, that effect will not fully reflect the dependence of the partitioning into the bilayer on particle geometry. Considering the

limitations of a thermodynamic analysis in isotropic mediums, a partitioning study of a nanoparticle into an ordered organic phase is very beneficial.

A lipid bilayer has a varying atomic composition in the direction normal to its surface. Bilayers are commonly divided into four parts along this axis, which are defined by their distance away from the center of the bilayer (Figure 2.5). Region 1 is the perturbed water region, or in other words, the aqueous phase adjacent to polar head surface of the membrane. Region 2 is interfacial region, which is characterized a high density of phosphate complexes. Region 3 is the soft-polymer zone, which is comprised primarily of the high-density hydrocarbon chains of the phospholipids. Region 4 is the hydrophobic core of the membrane, where the structure of the hydrocarbon chains reduces from that of region 3, resulting in a lower hydrocarbon density [18]. The classifications of such regions are important, as the varying compositions will have a substantial effect on diffusivity in the z direction. Figure 2.5 illustrates the distinct regions in a lipid bilayer.

.

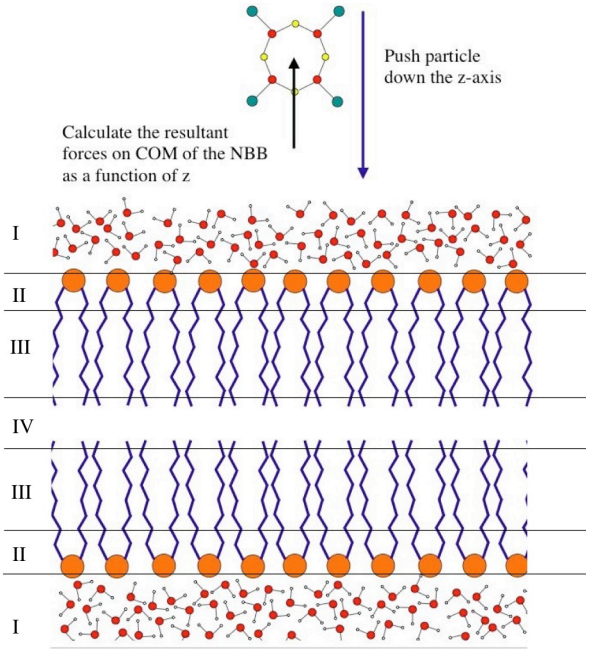

Figure 2.5: Perturbing the lipid bilayer with a particle

In an effort to understand the partitioning behavior of the C_{60} and H-POSS nanoparticles along the heterogeneous axis, the one-dimensional lipid/water partition function ($K(z)$) [17] has been calculated. The $K(z)$ parameter can be readily determined from the z-directed forces exerted on the solute by the water/lipid system on the nanoparticle, if the z-constrained partition function is considered. The equation below is the isothermal-isobaric partition function (Eq. 2.7), with one particle being constrained at a z value of z_2 [19]

$$\Delta(z_2) = \sum_U \sum_V \Omega(N,V,U)\delta(z_2 - z)e^{-\beta U} e^{-\beta PV} \tag{2.28}$$

if an additional partition function is taken at a reference depth, z_1, Equation 2.6 can be applied to yield to Gibbs free energy of transfer from depth z_1 to z_2

$$\Delta G(z_2) = -k_b T \ln\left[\frac{\Delta(z_2)}{\Delta(z_1)}\right] \tag{2.29}$$

If the derivative of Equation 2.29 is taken, the following result is noted

$$\frac{d\Delta G(z_2)}{dz_2} = -\frac{1}{\beta\Delta(z_2)}\frac{d\Delta(z_2)}{dz_2} \tag{2.30}$$

where

$$\frac{d\Delta(z_2)}{dz_2} = \sum_U \sum_V -\frac{1}{\beta}\Omega(N,V,U)\delta(z_2 - z)\frac{\partial U}{\partial z_2}e^{-\beta U}e^{-PV} \tag{2.31}$$

if Equation 2.31 and Equation 2.30 are combined, the result is similar to that of Equation 2.9. Therefore, $\Delta G(z_2)$ can be defined as

$$\Delta G(z_2) = \left\langle \frac{\partial U}{\partial z_2} \right\rangle = -\int_{z_1}^{z_2} \left\langle F_z(z_2) \right\rangle dz_2 \tag{2.32}$$

therefore the z-directed lipid/water partition function takes the following form.

$$K(z_2) = e^{-\Delta G(z_2)/RT} \tag{2.33}$$

In this study, $K(z)$ is obtained for the C_{60} and H-POSS nanoparticles by constrained them in one of the four regions of the phospholipids bilayer, where $F(z,t)$ is sampled every 50 fs, over a 2.5 ns production run.

References

1. McQuarrie, D.A., *Statistical Mechanics*. 2000, Sausalito, Ca: University Science Books.

2. Beutler, T.C., Mark, A.E., van Schaik, R.C., Gerber, P.R., and van Gunsteren, W.F., *Avoiding singularities and numerical instabilities in free energy calculations based on molecular simulations*. Chemical Physics Letters, 1994. **222**(6): p. 529-539.

3. Smith, W., Leslie, M., and Forester, T.R., *DL_POLY*. 2003, Daresbury Laboratory: Warrington, England.

4. Ben-Naim, A., *Solvation Thermodynamics*. 1987, Suffolf, NY: Springer.

5. Prausnitz, J.M., Lichtenthaler, Rudiger N., andGomes de Avezedo, Edmundo, *Molecular Thermodynamics of Fluid-Phase Equilibria*. Prentice Hall International Series in the Physical and Chemical Engineering Sciences, ed. N.R. Amundson, Upper Saddle River, NJ: Prentice Hall.

6. Newman, K.E., *Kirkwood-Buff Solution Theory: Derivation and Applications*. Chemical Society Reviews, 1994. **23**(1): p. 31-40.

7. Christensen, S., et al., *Thermodynamic models from fluctuation solution theory analysis of molecular simulations*. Fluid Phase Equilibria, 2007. **261**(1-2): p. 185-190.

8. Fredenslund, A., Jones, R.L., anf Prausnitz, *Group-Contribution Estimation of Activity Coefficients in Nonideal Liquid Mixtures*. AIChE Journal, 1975. **21**(6): p. 1086-1099.

9. Achard, C.D., Dussap, C.G., and Gros J. B., *Representation of vapour-liquid equilibria in water-alcohol-electrolyte mixtures with a modified UNIFAC group-contribtion method*. Fluid Phase Equilibria, 1994. **98**: p. 71-89.

10. Raabe, G., and Koehler, J., *Use of ab initio interaction energies for the prediction of phase equilibria in the system nitrogen-ethane*. Physical Chemistry Chemical Physics, 2002. **4**(6): p. 926-930.

11. Wu, H.S., and Sandler, Stanley I., *Use of ab Initio Quantum Mechanics Calculations in Group Contribution Methods. 1. Theory and Basis for Group Identifications*. Ind. Eng. Chem. Res., 1991. **30**(5): p. 881-889.

12. Kester, N.R., and Combariza, Jaime E., *Basis Set Superposition Errors: Theory and Practice*. Reviews of Computational Chemistry, ed. K.B. Lipkowitz, and Boyd, Donald B. Vol. 13. 1999: Wiley-VCH.

13. Simon, S., Duran, Miquel, and Dannenberg, J.J., *How does basis set superposition error change the potential surfaces for hydrogen bonded dimers?* Journal of Chemical Physics, 1996. **105**(24): p. 11024-11031.

14. Connolly, M.L., *Analytical Molecular Surface Calculation*. Journal of Applied Crystallography, 1983. **16**(5): p. 548-558.

15. Shrake, A. and J.A. Rupley, *Environment and Exposure to Solvent of Protein Atoms - Lysozyme and Insulin*. Journal of Molecular Biology, 1973. **79**(2): p. 351-371.

16. Pettersen, E.F., Goddard, T.D., Huang, C.C., Couch, G.S., Greenblatt, D.M., Meng, E.C., and Ferrin, T.E., *UCSF Chimera - A Visualization System for Exploratory Research and Analysis*. J. Comput. Chem., 2004. **25**(13): p. 1605-1612.

17. Bemporad, D., Luttman, C., and Essex, J.W., *Computer Simulation of Small Molecule Permeation across a Lipid Bilayer: Dependence on Bilayer Properties and Solute Volume, Size, and Cross-Sectional Area*. Biophysical Journal, 2004. **87**(1): p. 1-13.

18. Tieleman, D.P., Marrink, S.J., and Berendsen, H.J.C., *A computer perpective of membranes: molecular dynamics studies of lipid bilayer systems*. Biochemica et Biophysica Acta., 1997. **1331**: p. 235-270.

19. Marrink, S.-J., and Berendsen, J.C., *Simulation of Water Transport through a Lipid Membrane*. J. Phys. Chem., 1994. **98**(15): p. 4155-4168.

CHAPTER III

ON THE CALCULATION OF THE GIBBS FREE ENERGY OF SOLVATION FOR FULLERENE PARTICLES BY MOLECULAR DYNAMICS SIMULATIONS

Introduction

Fullerenes are among the most widely studied nanoparticles; in the past year alone, more than 2,500 papers have been published on the properties and potential applications of these materials. Like many other nanoparticles, there is a growing interest in incorporating fullerenes into biological systems, with applications including their use as HIV protease inhibitors [1], immunosensors for the detection of cancers and viruses [2], and light-mediated DNA cleaving agents [3].

Despite the potential of these carbon-based materials surprisingly, few studies have been reported that probe the environmental and physiological impact of fullerenes. Of particular interest is recent theoretical work that has demonstrated that C_{60} can bind to, and deform a DNA fragment [4], suggesting the potential for C_{60} molecules to disrupt replication and repair of DNA. However, this work [4] does not address whether C_{60} can enter the intracellular region of the cell and in turn expose DNA for potential damage. Of the experimental physiological studies performed [5-8], conflicting results regarding the toxicity of fullerene materials have been reported. While it is generally acknowledged [9-11] that fullerenes display a high level of aggregation, particularly in non-organic solvents, implying that the particles prefer carbon-rich environments to aqueous systems, several studies have shown that functionalizing fullerenes with hydrophilic groups [12, 13] or varying their aspect ratio [14], can lower tissue damage and hence toxicity. Since

both the addition of functional groups or molecular shape and size of a solute can significantly alter its partitioning between aqueous and organic phases, the lowered toxicity may be linked to the change in partitioning characteristics.

The almost limitless number of fullerene derivatives makes identifying the general partitioning behavior of fullerenes difficult. Furthermore, solubility data, which is key to understanding the partitioning of molecules between aqueous and organic phases, has been particularly difficult to measure accurately for fullerenes due to particle aggregation, particularly in polar fluids; the known agglomeration [15-17] behavior of buckyballs could explain the discrepancies observed in solubility data relative to temperature [18] and solvent chain length [19]. Experimental evidence suggests that buckyballs are effectively large, sticky spheres that can form very stable cluster configurations ranging from 13 to 147 particles [20] resulting in solubility shifts of up to two orders of magnitude compared to isolated particles in solution [21, 22].

In an effort to provide molecular level insight into the solubility and partitioning of fullerenes in this work, the Gibbs free energy of solvation has been determined for a family of fullerene particles in octanol and water solvents, through molecular dynamics simulation. From a comparison of the solubility of a particle in octanol to water, the octanol/water partition coefficient ($K_{O/W}$) can be determined. $K_{O/W}$ is commonly used in environmental and physiological studies to estimate the fate of the particle in the natural environment. The fullerenes studied in this work vary in volume, aspect ratio and solvent accessible surface area, which are attributes that are believed to impact particle solubility.

Simulation Details

Molecular dynamics simulations and thermodynamic integration have been used to determine the ΔG^{solv} for the fullerene particles of interest. The structures [23-25] of the particles studied are pictured in Figure 3.1 and their geometric attributes summarized in Table 3.1. As can be seen from Table 3.1 the particles studied were chosen to provide a range of aspect ratios and solvent accessible surface areas, in order to probe the effect of these quantities on the partitioning of fullerene materials.

Particle	**Diameter, Å**	**Length, Å**
C_{60}	7.0	7.0
Thick, Uncapped CNT	18.6	8.8
Thin, Uncapped CNT	6.1	28.6
Medium, Uncapped CNT	7.9	16.7
Thin, Capped CNT	7.9	23.7
Medium, Capped CNT	13.8	19.9
Thick, Capped CNT	15.1	16.9

Table 3.1: Geometries of the fullerene molecules studied in this work.

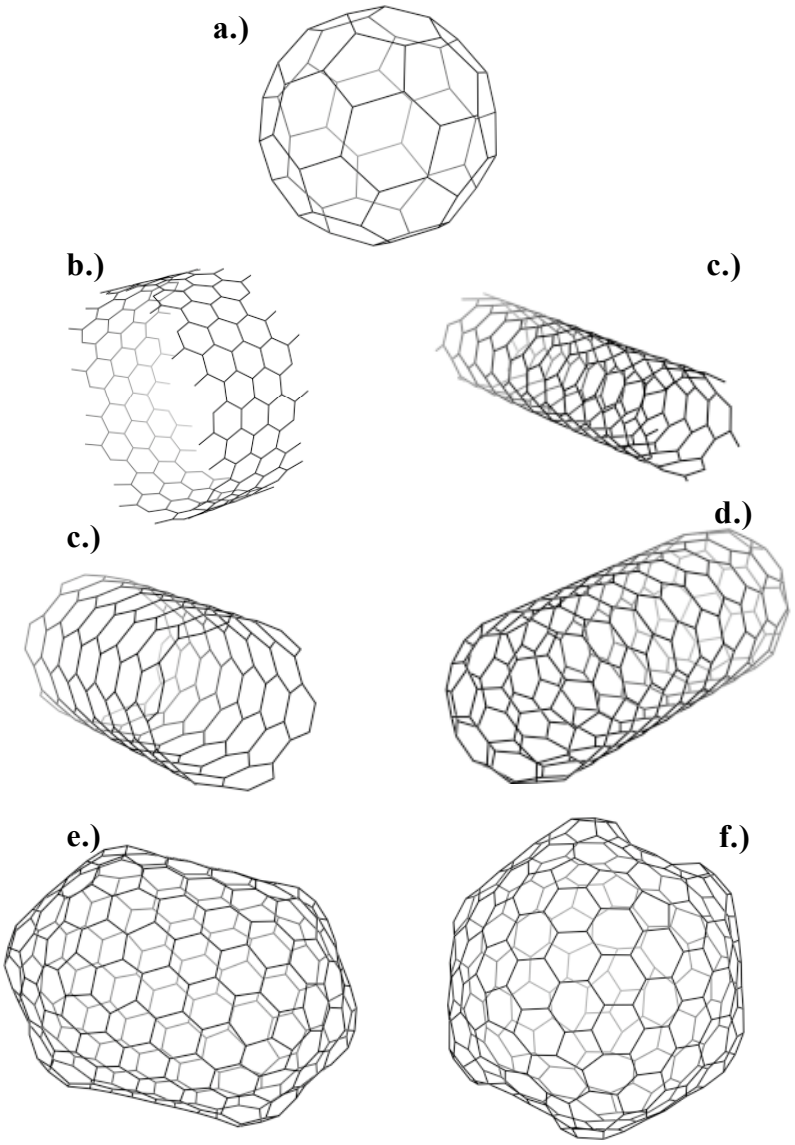

Figure 3.1: a) C_{60}, b) 15.1Å uncapped CNT, c) 6Å uncapped CNTsd) 8Å uncapped CNTs, e) 8Å capped CNTs, f) 13.5Å capped CNT and g) 15.1Å capped CNTs

The change in ΔG^{solv} for an isolated solute particle in solution can be calculated from molecular dynamics simulation using thermodynamic integration [26], in which the solute molecule is gradually "grown" into the solvent. The simulations are performed in the NPT ensemble, in which the number of solvent particles (N), the pressure (P) and the temperature (T) are held constant. For this ensemble it can be shown that [27],

therefore,

$$\left(\frac{\partial G}{\partial \lambda}\right)_{N,P,T} = \left\langle \frac{\partial U}{\partial \lambda} \right\rangle_{\lambda} \tag{3.1}$$

$$\Delta G^{solv} = \int_0^1 \left(\frac{\partial G}{\partial \lambda}\right)_{N,P,T} d\lambda = \int_0^1 \left\langle \frac{\partial U}{\partial \lambda} \right\rangle_{\lambda} d\lambda \tag{3.2}$$

where U is the potential between the solute and solvent and λ the coupling parameter, which is defined such that $\lambda = 0$ represents a pure solvent state and $\lambda = 1$ indicates a fully interacting particle in solution; all intermediate values of λ represent a "ghost" state for the solute particle, for which the solute-solvent-interactions are present but weakened. Hence, λ enters into the solvent-solute interactions. Given an explicit means of incorporating the λ parameter into the interactions between the solvent and the solute, from the trajectories produced from molecular dynamics simulations, the right hand side of Equation 3.2 can be computed. Thermodynamic integration therefore requires that the force fields used in the simulations be modified by the λ parameter in a fashion such that solvent/solute interactions are zero at $\lambda = 0$ and full at $\lambda = 1$.

The TraPPE united atom force field [28] was used to model the octanol solvent, the DREIDING force field [29] used to describe the fullerenes particles, and the SPC/E model [30] used to describe water. Below we discuss the choice of each of these potentials, with the reader is directed to the original references for full details of the potential models.

The TraPPE force field was chosen to describe the octanol molecules due to the accuracy of force field in describing liquid state properties and phase equilibria. In the TraPPE united atom force field the hydrogen atoms are not treated explicitly but

collapsed into a single site with the corresponding heavy atom. The bond stretching, bond angle bending, and torsional potentials between united atom sites are described by equations 3.3-3.5, are respectively

$$U_{stretch}\left(r_{ij}\right) = k_b\left(r_{ij} - r_o\right)^2 \tag{3.3}$$

$$U_{angle}\left(\theta_{ijk}\right) = k_\theta\left(\theta_{ijk} - \theta_o\right)^2 \tag{3.4}$$

$$U_{torsion}\left(\phi_{ijkl}\right) = c_o + c_1\left[1+\cos\left(\phi_{ijkl}\right)\right] + c_2\left[1-\cos\left(2\phi_{ijkl}\right)\right] + c_3\left[1+\cos\left(3\phi_{ijkl}\right)\right] \tag{3.5}$$

where k_b, k_θ, and c_i are the force constants, r_o is the equilibrium bond length, r_{ij} the length of the bond between adjacent bonded atoms i and j, θ_o the equilibrium bond angle and θ_{ijk} the angle between adjacent bonded atoms i, j, and k, and ϕ_{ijkl} the dihedral angle between the planes defined by four adjacent bonded atoms i, j, k, and l.

The SPC/E model is a commonly used three site water model that was chosen to describe the water molecules since it adequately describes the thermodynamic and structural properties of water [31] whilst being less computationally expensive than recent, more accurate models that incorporate more atomistic sites, such as TIP4P/2005 [32] , or effects such as explicit polarisability present in the GCPM water model [33].

The DREIDING force field has a similar functional form to the TraPPE force field; however in all simulations the solute is held fixed in the center of the simulation cell and is treated as a rigid body. Therefore only the non-bonded interactions are considered. For both the fullerene and solvent molecules the non-bonded interactions are modeled by a 12-6 Lennard-Jones (LJ) potential. In addition, a Coulombic term is used to describe electrostatic interactions between atoms i and j in the solvent molecules. The combined potential is therefore given by,

$$U_{ij}^{non-bonded}(r) = 4\varepsilon_{ij}\left[\left(\frac{\sigma_{ij}}{r}\right)^{12} - \left(\frac{\sigma_{ij}}{r}\right)^{6}\right] + \frac{1}{4\pi\varepsilon_0}\frac{q_i q_j}{r} \qquad (3.6)$$

where ε_{ij} is the LJ energy depth, σ_{ij} is the LJ diameter, ε_o is the permittivity of free space and q_i and q_j are partial charges on atoms *i* and *j*, and *r* is the distance between atoms *i* and *j*. For the fullerene/water cross interactions, the Bojan-Steele force field [34] is used, which has been noted for it's accuracy in modeling fullerenes in water [35, 36]. The cross terms for the fullerene/octanol interactions were obtained using Jorgensen's mixing rules, *viz*.

$$\varepsilon_{ij} = \sqrt{\varepsilon_i \varepsilon_j}; \sigma_{ij} = \sqrt{\sigma_i \sigma_j} \qquad (3.7)$$

As discussed above, in the molecular dynamics simulations a parameter λ is introduced to modifying the solute-solvent *inter*molecular interactions. In modifying the intermolecular potential it is important that the softened potentials exclude the possibility of numerical instabilities. To meet this end, the following form of the softened potentials was employed to ensure finite energies at small intermolecular radii [37]

$$U_{ij}^{LJ}(r,\lambda) = \lambda^n 4\varepsilon_{ij}\left(\frac{1}{\left[\alpha_{LJ}(1-\lambda)^2 + \left(\frac{r}{\sigma_{ij}}\right)^6\right]^2} - \frac{1}{\alpha_{LJ}(1-\lambda)^2 + \left(\frac{r}{\sigma_{ij}}\right)^6}\right) \qquad 3.8$$

where *n* is an integer and α_{LJ} is a positive constant, which are taken to be 2 and 0.50 respectively in this study.

The simulations were performed using the DL_POLY v. 2.13 [23] program at ambient conditions (i.e. P = 1 bar and T = 25 ˚C). Both the octanol and water simulations contain approximately 10,000 solvent atoms corresponding to 3,334 SPC/E water

molecules for the water solvent case and 1,000 TraPPE octanol molecules for the octanol solvent case. A Verlet integrator with a 10Å neighbor list was used to integrate the equations of motion. The Ewald summation method was implemented to calculate the long-ranged electrostatic interactions and a Nosè-Hoover thermostat and barostat were used to provide temperature and pressure.

The solute was held fixed in the center of the simulation cell as it has been found that allowing arbitrary conformational changes in the solute can lead to significant noise in the thermodynamic integration analysis [38]. This restricts the particle from translating, rotating, or flexing, which can be problematic if the solute has multiple, probable, conformations, in which case multiple simulations must be performed to account for each conformation of the solute. Fullerene molecules as large or larger than C_{60} are commonly acknowledged to be relatively rigid structures [39], due primarily to geometric constraints [40]. Thus, the assumption of a rigid structure is a reasonable approximation in our work.

Each thermodynamic integration analysis performed in this work has 15 samples at regular intervals of λ. The soft-potential (i.e. $\lambda \approx 0$) regimes of the thermodynamic integration curve are very sensitive to changes in λ. Therefore, for $\lambda \leq 0.50$, an increment of 0.05 was used. For $\lambda \geq 0.50$, the thermodynamic integration curve becomes linear with increasing λ and so larger increments (0.10) were implemented. After a 1 ns equilibration period, each λ value was sampled for an additional ns to ensure that an accurate value for $\langle \partial U(\lambda)/\partial \lambda \rangle_\lambda$ was obtained.

Results and Discussion

The ΔG^{solv} for each fullerene particle in water and octanol has been calculated and the change in solvent structure relative to the solute of interest analyzed. We first present the results for the particles in water and then in octanol before comparing the results and discussing the implications on solubility relative to particle geometry. Table 3.2 summarizes the solubility of each nanoparticle in water and octanol respectively in addition to reporting the calculated Connolly area and surface-enclosed volume, both of which were determined using a probe size of 1.4Å [41, 42].

Particle	**ΔG^{solv} (kcal/mol) water**	**ΔG^{solv} (kcal/mol) octanol**	**Diameter (Å)**	**Connolly Area (Å^2)**	**Excluded Volume (Å^3)**
C_{60}	10.97 +/- 7.5	-18.91 +/- 3.1	7	307	477.0
Thin, Capped CNT	21.58 +/- 4.0	-77.21 +/- 3.9	7.9	971.4	2220
Medium, Capped CNT	31.01 +/- 4.0	-82.19 +/- 4.4	13.75	1214	3673
Thick, Capped CNT	31.62 +/- 4.0	-77.96 +/- 6.4	15.1	1174	3534
Thin, Uncapped CNT	51.62 +/- 5.2	-56.42 +/- 6.0	6.1	1046	2034
Medium, Uncapped CNT	41.70 +/- 4.2	-82.32 +/- 5.8	7.9	1082	1454
Thick, Uncapped CNT	86.85 +/- 8.7	-66.38 +/- 5.8	18.6	1768	2195

Table 3.2:ΔG^{solv} in water and octanol with geometric attributes for fullerenes

Fullerenes in Water Solvent

The results in Table 3.2 clearly show that all of the fullerene particles exhibit a hydrophobic nature, regardless of their geometric attributes. The general expectation that inserting a large, hydrophobic particle into water will result in a higher ΔG^{solv} than the insertion of a chemically similar, smaller particle is observed; the free energy of solvation

of the C_{60} particle in water is by far the lowest as would be expected on the basis of the least disruption to the water hydrogen bonding network [43] and the smallest cavity volume needed to accommodate the nanoparticle. Perhaps surprisingly, we see a considerable increase the solvation free energy for the uncapped systems relative to similarly sized and shaped capped fullerenes. In Figure 3.2, we compare the thermodynamic integration curves for capped and uncapped carbon nanotubes with similar diameters, in water.

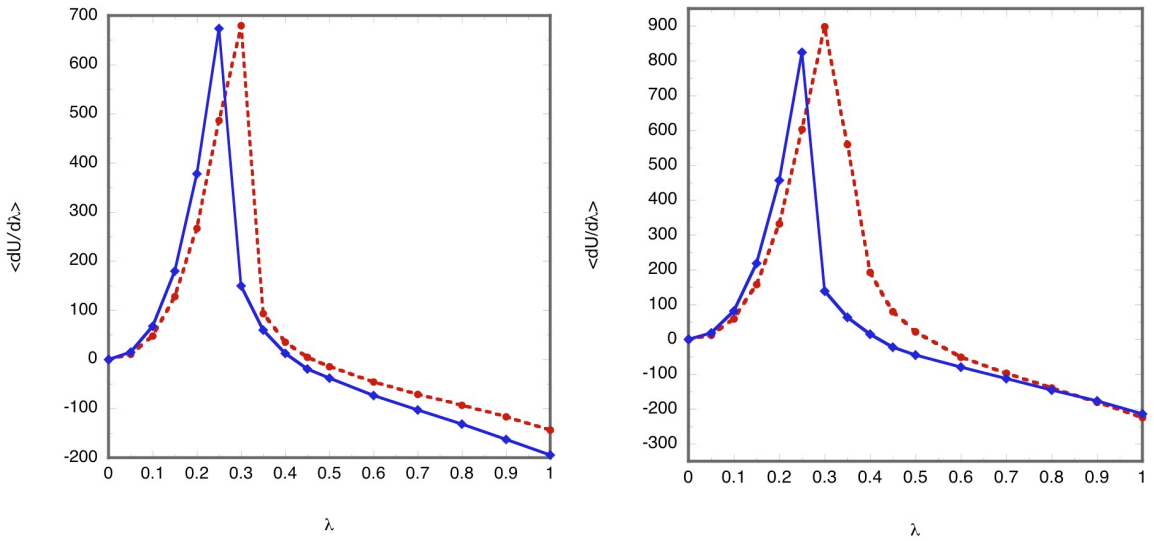

Figure 3.2: Thermodynamic integration curve for 8Å uncapped/capped carbon nanotubes (left) and 18.6Å uncapped and 15.1Å capped carbon nanotubes (right). Results for the capped particles are shown by the solid lines and the uncapped by the dotted lines

The curves shown in Figure 3.2 are representative of the behavior seen for all the fullerenes in water, in that the maxima are shifted for all uncapped fullerenes relative to their capped analogues, resulting in a positive shift in ΔG^{solv} for the uncapped fullerenes. This behavior can be understood if the possibility of water entering the cavity of the uncapped nanotube is considered.

In a series of papers, Hummer and coworkers [44-47] have studied the kinetics of the filling/emptying mechanism of water in carbon nanotubes and have shown that water

molecules can enter the core of an open 8.1Å diameter carbon nanotube. Additionally it was found that while the 6.1Å and 7.9Å open nanotubes did not allow water inside the tube at full potential, when the potential was softened ($\lambda \leq 0.40$) water did enter the tubes, resulting in an increase in energy (and hence positive $\langle \partial U(\lambda)/\partial\lambda \rangle_\lambda$). The increase in energy upon entry into of the water molecules into the nanotube was found to be due to the disruption of the hydrogen bonds of the water molecules with the *bulk* water. We also note that experimental studies [48] have demonstrated the same behavior for a 14.1Å open nanotube. We therefore attribute the shift in maxima seen in the thermodynamic integration curves for the uncapped nanotubes compared to their capped counter parts to the water solvent entering the interior of the uncapped nanotubes at low values of λ, while the water is excluded from the central cavity in the closed nanotubes. To illustrate, in Figure 3.3 we present the cross sectional water density averaged over the length of the nanotube, for the 7.9Å uncapped, 6.1Å uncapped, and the 7.9Å capped systems at λ = 0.30 are presented. The figure confirms that water enters the open nanotubes at the softened potentials, whereas water does not enter the capped nanotube, leading to the observed differences in ΔG^{solv}.

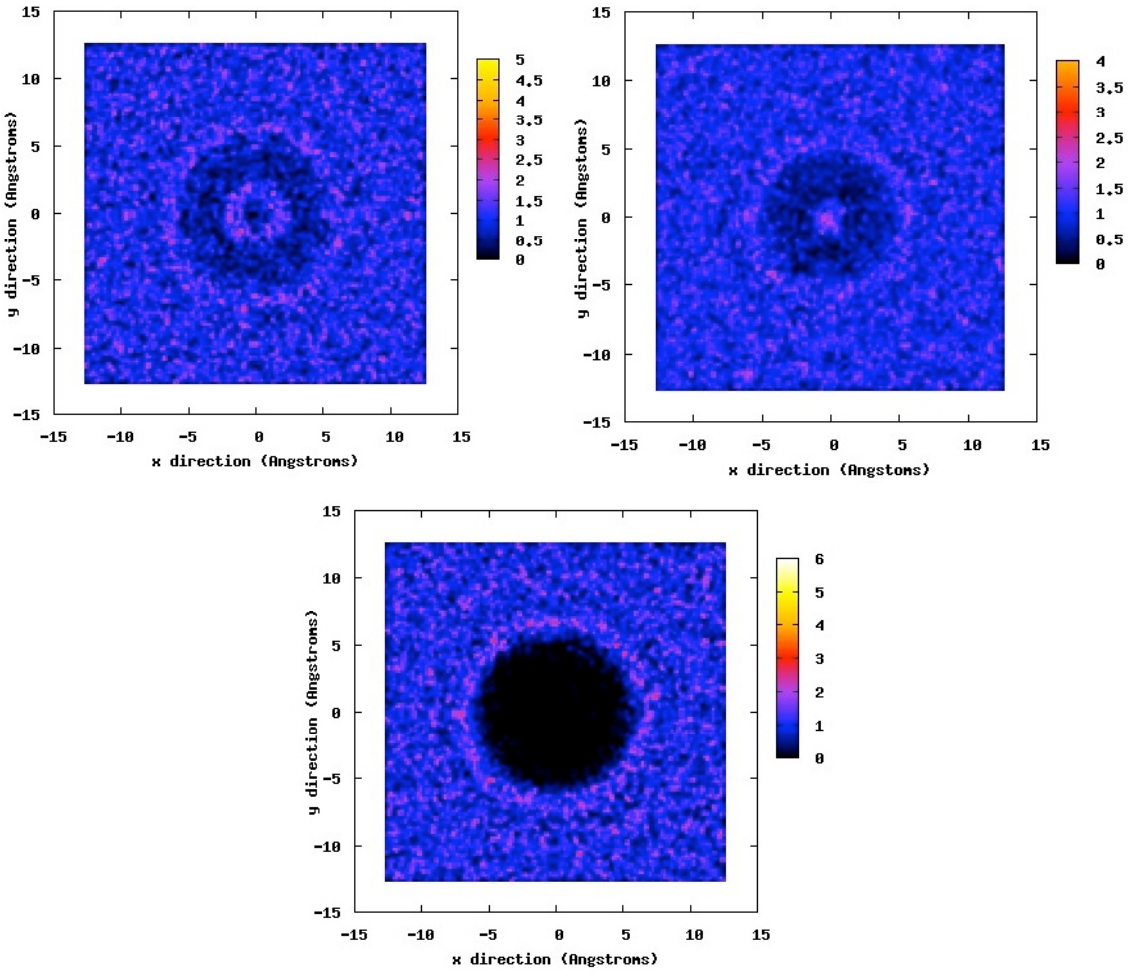

Figure 3.3**:** Water density profiles around 7.9Å uncapped (top left), 6.1Å uncapped (top right) and 7.9Å capped (bottom center) carbon nanotubes obtained form molecular dynamics simulations with λ = 0.30. Scale in g/cm^3.

We now consider the connection between the molecular topology of the solute and ΔG^{solv}. In particular, we consider the surface areas as implicit solvation methods, such as the generalized Born/surface area (GBSA)[49], have linked ΔG^{solv} of an uncharged particle to its surface area *viz*,

$$\Delta G^{solv} = \sum_k \sigma_k SA_k \tag{3.9}$$

where σ_k is an empirical parameter and SA_k is the surface area of atom k. The solvent-accessible surface area and solute-excluded volume for the fullerene particles in water have been calculated with a spherical probe of radius 1.4Å, using the Connolly and surface-enclosed volume techniques, respectively [41, 42]. The Connolly surface area is generated by rolling the solvent probe along the surface of the particle, and the area is determined from the number of times the probe has turned while rolling over the surface. The surface enclosed volume is simply generated by numerically integrating the Connolly surface area over the enclosed volume. In Figure 3.4, we show the relationship between ΔG^{solv} and Connolly area and in Figure 3.5 the relationship between ΔG^{solv} and excluded volume for the capped fullerenes [41, 42].

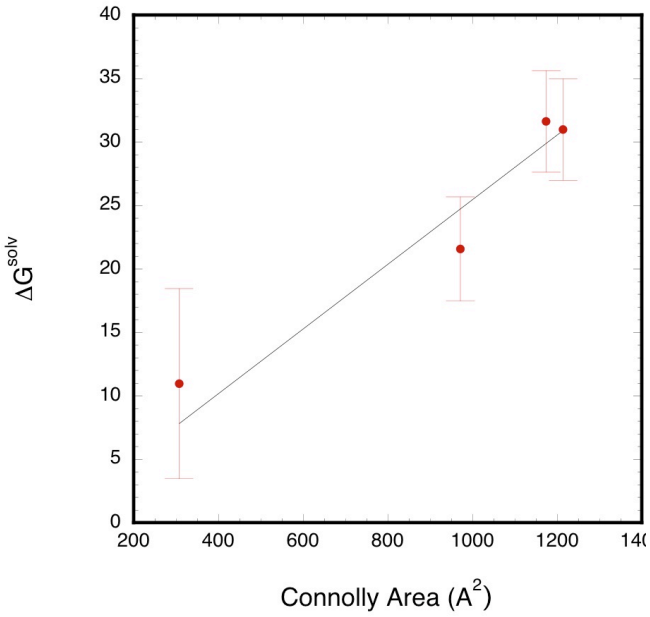

Figure 3.4: ΔG^{solv} vs. Connolly surface area for capped fullerenes in water

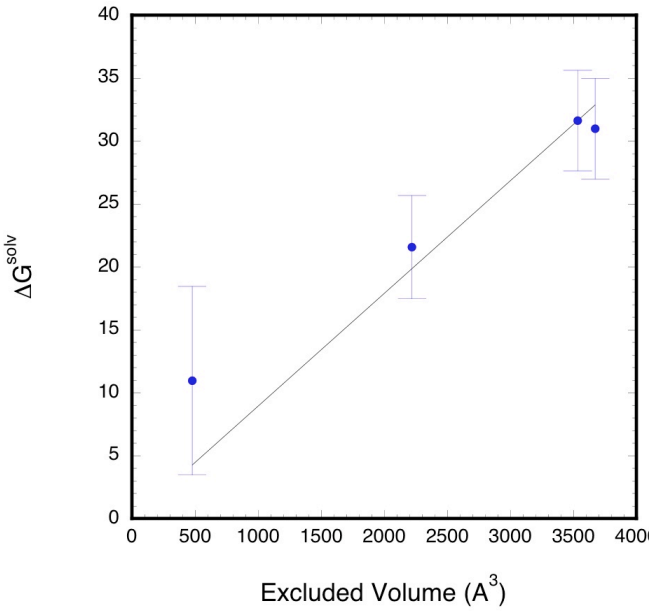

Figure 3.5: ΔG^{solv} vs. excluded volume for capped fullerenes in water

As can be seen from the figures both the solvent accessible surface area and the excluded volume exhibit an approximately linear trend, indicating a correlation between the size of the solute and ΔG^{solv}. The interfacial surface tension is often substituted σ_k in Equation 3.9 for the calculation of $\Delta G^{solv}$of flat particles, where approximately 30% of the interfacial surface tension can be used for curved surfaces [50]. The slope of the fitted line in Figure 4 gives a value of 19.1 mJ/m^2, which is within reasonable agreement with 30% of the interfacial surface tension of graphite/water, which is 28.6 mJ/m^2 [51].

A similar comparison is difficult for the uncapped nanotubes, due to the influence of water accessing the core of the nanotube on ΔG^{solv}. It is noteworthy that a moderate jump in energy is observed between the 7.9Å and 6.1Å uncapped nanotubes despite the fact that both tubes have almost identical Connolly areas, while the latter has a significantly larger excluded volume. This provides evidence that the excluded volume also effects ΔG^{solv} and is not due to the fact that the excluded volume often increases with an increase in accessible surface area.

Fullerenes in Octanol Solvent

The thermodynamic integration analysis of the 7 fullerenes studied in octanol indicates a more conventional relationship between the ΔG^{solv} and solute geometry, particularly for the capped fullerenes, than that observed in water. Although, there is a jump in energy for the uncapped nanotubes compared to the capped nanotubes, the energetic effect of the caps in the octanol solvent is considerably smaller than in a water solvent. This is likely a result of varying degrees of partial wetting due to the chain nature of the solvent and the diameter of the given nanotube. From a CH_x density study for the capped nanotubes, similar to that performed for water and reported in Figure 3.3, we find that the capped fullerenes are completely devoid of interstitial octanol at low values of λ. For the uncapped nanotubes at $\lambda = 0.25$ the interior of the 6.1Å uncapped nanotube is found to be relatively devoid of organic carbon, the 7.9Å uncapped nanotube has a low, yet finite CH_x concentration and the 18.6Å nanotube can easily accommodate the octanol solvent. This suggests that neither the 6.1Å nanotube nor the 7.9Å will exhibit an extended region of increasing $\langle \partial U(\lambda)/\partial\lambda \rangle_\lambda$, as was the case in the water systems. The 18.6Å nanotube will potentially be subject to the energy penalty, as its diameter is large enough to easily accommodate octanol molecules. However, this penalty is likely to be relatively small, as hydrogen-bond breakage for transitioning an octanol molecule from bulk to the interior of the nanotube will be much smaller than that for water. Figure 3.6 compares the TI curves for the uncapped nanotubes. Note that all the $\langle \partial U(\lambda)/\partial\lambda \rangle_\lambda$ curves peak at approximately the same value of λ, with the largest nanotube exhibiting a shoulder on the right hand side, which is consistent with the observations discussed above.

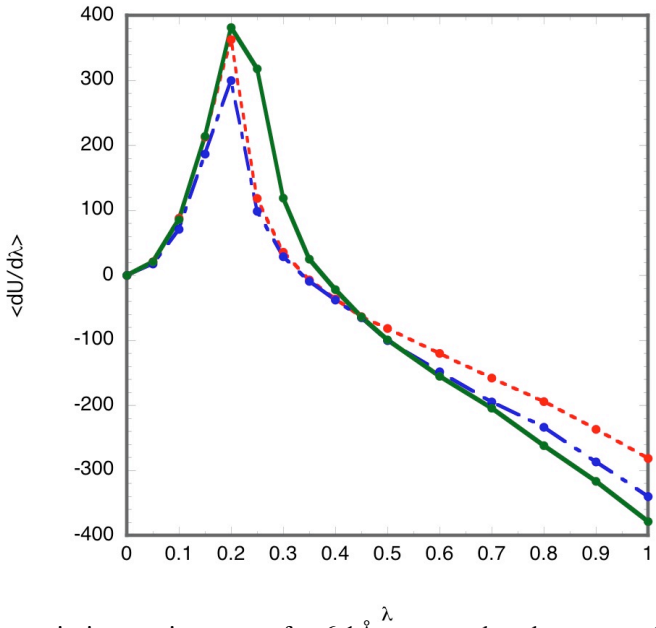

Figure 3.6: Thermodynamic integration curve for 6.1Å uncapped carbon nanotubes (dotted line), 7.9Å uncapped carbon nanotube (dash-dotted line) and 18.6Å uncapped carbon nanotube (solid line)

From the figure we note that the 7.9Å thermodynamic integration curve has a lower tail at high λ regimes than the 6.1 Å curve, indicating a greater negative free energy contribution. This is likely due to the interior of the 7.9Å nanotube being more accessible to octanol than the 6.1Å nanotube. Considering the very similar solvent accessible surface areas reported in Table 1.1 for the 6.1Å and 7.9Å nanotubes, it is likely that either the Connolly solvent-accessible surface area for the interior of 6.1Å nanotube has been overestimated, or the interior accessible area for the 7.9Å nanotube had been underestimated. The likelihood of a misrepresentative Connolly surface area for a particle in an anisotropic solvent, such as octanol, will be greater than in water since the analysis is done with a spherical probe. Interestingly, the thermodynamic integration curve for the 18.6Å nanotube is somewhat pronounced at $\lambda = 0.25$ and 0.30 values, which is similar to the shift observed in the TI graphs for uncapped nanotubes in water. It is reasonable to expect that since the thick uncapped nanotubes are wide enough to accommodate many

octanol molecules, this effect is also due to solvent molecules entering the cavity of the nanotube and hydrogen bonds being broken resulting in higher energy.

In Figures 3.7 and 3.8 we present the relationship between ΔG^{solv} and the Connolly surface area and excluded volume for capped fullerenes in octanol.

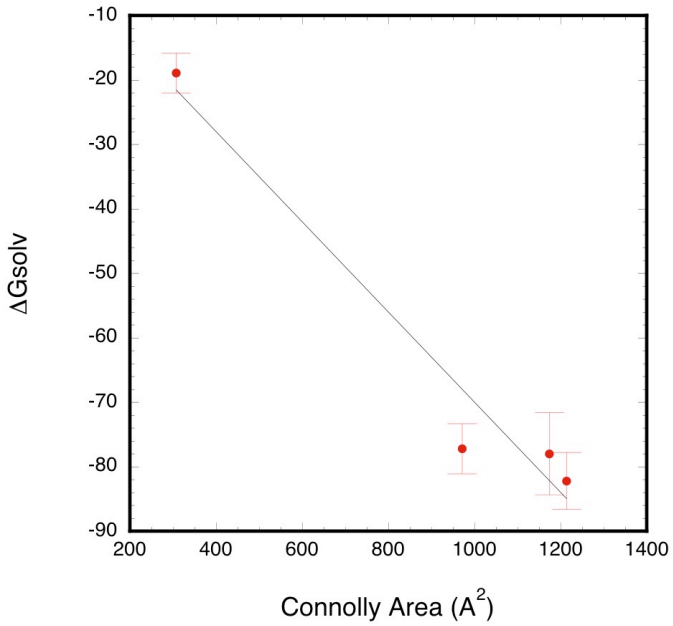

Figure 3.7: ΔG^{solv} vs. Connolly area for capped fullereznes in octanol

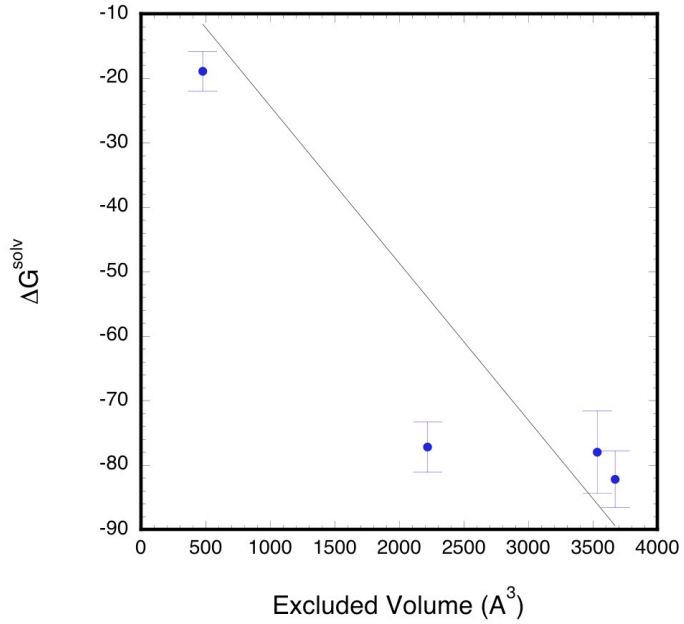

Figure 3.8: ΔG^{solv} vs. excluded volume for capped fullerenes in octanol

Again, Figure 3.7 indicates an approximately linear relationship between ΔG^{solv} Connolly surface area, whereas Figure 3.8 shows a decaying relationship between ΔG^{solv} and excluded volume. Again, the GBSA model appears to be applicable to the fullerene systems.

Conclusion

The ΔG^{solv} for 7 different fullerene molecules of differing molecular geometry has been calculated using molecular dynamics simulation and thermodynamic integration. The findings in this work generally support previous findings in the literature that report strong hydrophobicity for fullerene molecules and a relatively high solubility in many organics [19, 52, 53]. This is evidenced by the consistently positive ΔG^{solv} values for fullerenes in water and negative ΔG^{solv} values for fullerenes in octanol. Furthermore, general trends between ΔG^{solv} and geometric attributes, such as the Connolly area and excluded volume, are seen for capped fullerenes. The results generally fit within the constructs of simple implicit solvation models, such as GBSA; additionally, the linear fit of ΔG^{solv} versus solvent accessible surface area for capped fullerenes in water gives an approximation to the interfacial water/graphite surface tension [50, 51], which is often used for the empirical constant in the GBSA equation. For capped nanotubes, it is observed that ΔG^{solv} in water increases as the Connolly surface area and the excluded volume increase. The ΔG^{solv} for capped carbon nanotubes in octanol decays with increasing solute size, with larger particles having significantly lower solvation energies. Therefore, it seems likely that large, capped fullerenes may partition into organic phases more readily. No general correlation is noted for uncapped fullerenes relative to solute

geometry due to the solute entering the cavity of the nanotube in the systems studied. Solute density maps show that, depending on particle diameter; water can enter the interior cavity at various degrees and form "water wires." We believe, the entry of water molecules into the interior of the tube results in an overall loss of hydrogen bonds between the water molecules, resulting in a larger ΔG^{solv} for the uncapped tubes compared to the capped tubes.

References

1. Da Ros, T., Prato, M., *Medicinal Chemistry with Fullerenes and Fullerene Derivatives*. Chem. Commun,, 1999: p. 663-669.

2. Veetil, J.V., and Ye, K, *Development of Immunosensors Using Carbon Nanotubes*. Biotechnol. Prog., 2007. **23**: p. 517-531.

3. Tokuyama, H., Yamago, S., and Nakamura, E., *Photoinduced Biochemical Activity of Fullerene Carboxylic Acid*. J. Am. Chem. Soc., 1993. **115**: p. 7918-7919.

4. Zhao, X., Striolo, A., Cummings, P.T., *C60 Binds to and Deforms DNA. Biophysical Journal, 2005*. Biophysical Journal, 2005. **89**(6): p. 3856-3662.
5. Oberdöster, E., *Manufactured Nanomaterials (Fullerenes, C60) Induce Oxidative Stress in the Brain of Juvenile Largemouth Bass*. Environmental Health Perspectives, 2007. **112**(10).

6. Szendi, K., and Varga, Csaba, *Lack of genotoxicity of carbon nanotubes in a pilot study*. Anticancer Research, 2008. **28**(1A): p. 349-352.

7. Miyawaki, J., Yudasaka, Masako, Azami, Takeshi, Kubo, Yoshimi, and Lijima, Sumio, *Toxicity of Single-Walled Carbon Nanohorns*. ACS Nano, 2008. **2**(2): p. 213-226.

8. Dhawan, A., Taurozzi, Julian S., Pandey, Alok K., Shan, Wenqian, Miller, Sarah M., Hashsham, Syed A., and Tarabara, Volodymyr V., *Stable Colloidal Dispersions of C60 Fullerenes in Water: Evidence for Genotoxicity*. Environ. Sci. Technol., 2006. **40**(23): p. 7394-7401.

9. Terashima, T., and Negao, S., *Solubilization of [60]Fullerene in Water by Aquatic Human Substances*. Chemistry Letters, 2007. **36**(2): p. 302-303.

10. Boarke, A.D., and Patnaik, A., *Self-Organization of Nanoparticles in Carbon Disulfide Solution*. J. Phys. Chem. B., 2003. **107**(25): p. 6079-6086.

11. Rudalvevige, T., Francis, A.H., and Zand, R., *Spectroscopic Studies of Fullerene Aggregates*. J. Phys. Chem. A., 1998. **102**(48): p. 9797-9802.

12. Sayes, C.M., Fortner, J.D., Guo, W., Lyon, D., Boyd, A.M., Ausman, K.D., Tao, Y.J., Sitharamann, B., Wilson, L.J., Hughes, J.B., West, J.L., and Colvin, V., *The Differential Cytotoxicity of Water-Soluble Fullerenes*. Nano Letters, 2004. **4**(10): p. 1881-1887.

13. Dumortier, H., Lacotte, S., Pastorin, G., Marega, R., Wu, W., Bonifazi, D., Briand, J-P., Prato, M., Muller, S., and Bianco, A., *Functionalized Carbon Nanotubes and Non-Cytootoxic and Preserve the Functionality of Primary Immune Cells*. Nano Letters, 2006. **6**(7): p. 1522-1528.

14. Magrez, A., Kasas, S., Salicio, V., Pasquier, N., Seo, J.W., Celio, M., Catsicas, S., Schwallerm, B., and Forro, Laslo, *Cellular Toxicity of Carbon Based Nanomaterials*. Nano Letters, 2006. **6**(6): p. 1121-1125.

15. Chen, B., Siepmann, J.I., Karaborni, S. and Klein, K., *Vapor-Liquid and Vapor-Solid Phase Equilibria of Fullerenes: The Role and Potential Shape on the Triple Point*. J. Phys. Chem. B., 2003. **104**(44): p. 12320-12323.

16. Hagen, M.H.J., Meijer, E.J., Mooij, G.C.A.M., Frenkel, D. and Lekkerlerker, H.N.W., *Does C60 Have a Liquid Phase?* Nature, 1993. **365**: p. 425-426.

17. Brant, J., Lecoanet, H., and Wiesner, M., *Aggregation and Deposition Characteristics of Fullerene Nanoparticles in Aqueous Systems*. Journal of Nanoparticle Research, 2005. **7**: p. 545-553.

18. Hansen, C.M., and Smith, A.L., *Using Hansen Solubility Parameters to Correlate Solubility of C60 Fullerene in Organic Solvents and in Polymers*. Carbon, 2004. **42**: p. 1591-1597.

19. Sivaraman, N., Dhamodarenn, R., Kaliappen, I., Srinivasan, T.G., Vasudeva Rao, P.R., and Mathes, C.K., *Solubility of C60 in Organic Solvents*. J. Org. Chem., 1992. **57**(22): p. 6077-6079.

20. Branz, W., Malinowski, N., Enders, A., and Martin, T.P., *Structural Transitions in (C60)n Clusters*. Physical Review B., 2002. **66**(094107): p. 1-14.

21. Avramenko, N.V., Korobov, M.V., Parenova, A.M., Dorozhko, P.A., Kiseleva, N.A., and Dolgov, P.V., *Thermochemistry of C60 and C70- Fullerene Solvates*. J. Therm. Anal. Cal., 2006. **84**: p. 259-262.

22. Marcus, Y., Smith, A.L., Korobov, M.V., Mirakyan, A.L., Avramenko, N.V., and Stukalin, E.B., *Solubility of C60 Fullerene*. J. Phys. Chem. B., 2001. **105**(13): p. 2499-2506.

23. Smith, W., and Forrester, T.R., *DL_POLY*. 2003, Daresbury Laboratory: Warrington, England.

24. Pedretti, A., Villa, L., and Vistoli, G., *VEGA: A Versatile Program to Convert, Handle and Visualize Molecular Structures on Windows-based PCs*. J. Mol. Graph., 2002. **21**: p. 47-49.

25. Ni, B., Andrews, R., Jacques, D., Qian, D., Wijesundara, M.B.J., Choi, Y., Hanley, L., Sinnott, S.B., *A Combined Computational and Experimental Study of Ion-Beam Modification on Carbon Nanotube Bundles*. J. Phys. Chem. B., 2001. **105**(51): p. 12719 - 12725.

26. Frenkel, D., and Smit B., *Understanding Molecular Simulation: From Algorithms to Applications*. 2002: Academic Press.

27. McQuarrie, A., *Statistical Mechanics*. 2000, Saucilito, Ca: University Science Books.

28. Chen, B., Pottoff, J.J, and Siepmann, J.I., *Monte Carlo Calcultions for Alcohols and their Mixtures with Alkanes. Transferable Potentials for Phase Equilibria. 5. United-Atom Description of Primary, Secondary, and Tertiary Alcohols*. J. Phys. Chem. B., 2001. **105**(15): p. 3093-3104.

29. Mayo, S.L., Olafson, B.D. and Goddard III, W.A., *DREIDING: A Generic Force Field for Molecular Simulations*. J. Phys. Chem., 1990. **94**(26): p. 8897-8909.

30. Rick, S.W., Stuart, S.J., and Berne, B.J., *Dynamical Fluctuating Charge Force Fields: Application to Liquid Water*. J. Chem. Phys., 1994. **101**(7): p. 6141-6156.

31. Jedlovszky, P., et al., *Analysis of the hydrogen-bonded structure of water from ambient to supercritical conditions*. Journal of Chemical Physics, 1998. **108**(20): p. 8528-8540.

32. Abascal, J.L.F. and C. Vega, *A general purpose model for the condensed phases of water: TIP4P/2005*. Journal of Chemical Physics, 2005. **123**(23).

33. Paricaud, P., et al., *From dimer to condensed phases at extreme conditions: Accurate predictions of the properties of water by a Gaussian charge polarizable model*. Journal of Chemical Physics, 2005. **122**(24).

34. Bojan, M.J., and Steele, W.A., *Interactions of Diatomic Molecules with Graphite*. Langmuir, 1987. **3**(6): p. 1123-1127.

35. Walther, J.H., Raffe, R., Halicioglu, T., and Koumoutsakos, P., *Carbon nanotubes in Water: Structural Characteristics and Energetics*. J. Phys. Chem. B., 2001. **105**(41): p. 9980 - 9987.

36. Walther, J.H., Jaffe, R.L., Kotsalis, E.M., Werder, T., Halicioglu, T., Koumoutsakos, P., *Hydrophobic Hydration of C60 and Carbon Nanotubes in Water*. Carbon, 2004. **42**: p. 1185-1194.

37. Beutler, T.C., Mark, A.E., van Schaik, R.C., Gerber, P.R., and van Gunsteren, W.F., *Avoiding Singularities and Numerical Instabilities in Free Energy Calculations Based on Molecular Simulations*. Chemical Physics Letters, 1994. **222**: p. 524-539.

38. Wescott, J.T., Fisher, L.R., and Hanna, S., *Use of Thermodynamic Integration to Calculate Hydration Free Energies of n-Alkanes*. J. Chem. Phys., 2002. **116**(6): p. 2361-2369.

39. Liu, X., and Chen, Z., *Curved Pi-Conjugation, Aromaticity, and Related Chemistry of Small Fullerenes (<C60) and Single-Walled Carbon Nanotubes*. Chem. Rev., 2005. **105**(10): p. 3643-3696.

40. Kroto, H.W., *The Stability of Fullerenes, C-24, C-28, C-32, C-36, C-50, C-60, and C-70*. Nature, 1987. **329**(8): p. 529-531.

41. Sanner, M.F., Olson, A.J. and Spehner, J.C., *Reduced Surface:An Efficient Way to Compute Molecular Surfaces*. Biopolymers, 1996. **38**(3): p. 305-320.

42. Pettersen, E.F., Goddard, T.D., Huang, C.C., Couch, G.S., Greenblatt, D.M., Meng, M.C., and Ferrin, T.E., *UCSF Chimera - A Visualization System for Exploratory Research and Analysis*. J. Comput. Chem., 2004. **25**(13): p. 1605-1612.

43. McCabe, C., Galindo, A., and Cummings, P.T., *Anomalies in the Solubility of Alkanes in Near-Critical Water*. J. Phys. Chem. B., 2003. **107**(44): p. 12307-12314.

44. Hummer, G., Rasaiah, J.C., and Noworyta, J.P., *Water Conduction Through the Hydrophobic Channel of a Carbon Nanotube*. Nature, 2001. **414**: p. 188-190.

45. Waghe, A., Rasaiah, J.C., and Hummer, G., *Filling and Emptying Kinetics of Carbon Nanotubes in Water*. J. Chem. Phys., 2002. **117**(23): p. 10789-10795.

46. Andreev, S., Reichman, D., Hummer, G., *Effect of Flexibility on Hydrophobic Behavior of Nanotube Water Channels*. J. Chem. Phys., 2005. **123**(19): p. 194502-194502-9.

47. Sriraman, S., Kevekidis, I.G., and Hummer, G., *Coarse Nonlinear Dynamics and Metastability of Filling-Emptying Transitions: Water in Carbon Nanotubes*. Physical Review Letters, 2005. **95**(130603): p. 1-2.

48. Kolesnikov, A.I., Zanotti, Jean-Marc, Loong, Chun-Keung, Thiyagarajan, Pappannan, Moravsky, Alexander P., Loutfy, Raouf O., and Burnham, Christian J., *Anomalously Soft Dynamics of Water in a Nanotube: A Revelation of Nanoscale Confinement*. Physical Review Letters, 2004. **93**(3): p. 035503-1-035503-4.

49. Still, W.C., Tempczyk, A., Hawley, R.C., and Hendrickson, T., *Semianalytical Treatment of Solvation for Molecular Mechanics and Dynamics*. J. Am. Chem. Soc., 1990. **112**(16): p. 6127-6129.

50. Moore, J.W., and Pearson, R.G., *Kinetics and Mechanism*. 1981: John Wiley and Sons.

51. Helmy, A.K., Ferreiro, E.A., de Bussetti, S.G., *The Water/Graphitic-carbon Interaction Energy*. Applied Surface Science, 2007. **253**(11).

52. Beck, M.T., *Solubility and molecular state of C60 and C70 in solvents and solvent mixtures*. Pure and Applied Chemistry, 1998. **70**(10): p. 1881-1887.

53. Kulkarni, P.P.a.J., Chad T., *Solubility of C60 in Solvent Mixtures*. Environ. Sci. Technol., 2008. **42**(3): p. 845-851.

CHAPTER IV

ESTIMATING INFINITELY DILUTE ACTIVITY COEFFICIENTS FOR SELECTED NANOPARTICLES USING GROUP-CONTRIBUTION METHODS AND AB INITIO CALCULATIONS

Introduction

Accurate models for the estimation of activity coefficients are essential in many fields of science and engineering, such as process design and the modeling of the fate of chemicals in the environment. With the burgeoning interest in nanoscience [1], there is a growing need for data on the solubility of these particles in common solvents, such as water and octanol, and their partitioning between phases in equilibrium. In particular, accurate descriptions of the infinite dilution activity coefficient of these particles in water and octanol solvents would allow for the calculation of the octanol-water partition coefficient, $K_{O/W}$, which is one of the key parameters used in modeling of the fate of chemicals in the environment. For a given solute, labeled U, $K_{O/W}$ is defined as follows: assume that U is present in two immiscible liquid phases, one octanol-rich, the other water-rich, in equilibrium with each other. If the mole fraction of U in the octanol-rich liquid phase is $x_U^{octanol}$ and the mole fraction of U in the water rich phase is x_U^{water}, then

$$K_{O/W} = \frac{x_U^{octanol}}{x_U^{water}} \tag{4.1}$$

Clearly, as in any liquid-liquid immiscibility problem, activity coefficients will play a key role in the calculation of $K_{O/W}$, as discussed below.

Many empirical methods such as UNIFAC [2], QSAR [3], and AlogPS [4] have been developed for the direct estimation of $K_{O/W}$ or indirectly through the estimation of activity coefficients. These techniques use a variety of approaches, such as empirical linear combinations of physiochemical properties deemed to effect $K_{O/W}$ (QSPR) or the use of associative neural networks with input from large physiochemical databases (AlogPS). Alternatively, some molecular-simulation-based techniques, such as thermodynamic integration or Widom particle insertion [5] have been developed for the calculation of the chemical potential of a solute. Such techniques can often yield very accurate solubilities, but can also be limited due to the size of the particle, the lack of relevant force fields, and computational expense.

From a practical standpoint, group-contribution activity coefficient methods seem to be the optimal choice, as the calculations take little computational effort compared to molecular-simulation-based methods, and the group parameters are intended to be applicable, and thus predictive, for many molecular species. Furthermore, molecular-simulation based studies may be insufficient for the calculation of $K_{O/W}$ in instances where the solute is largely or completely miscible in the solvent. For miscible solutes, parameters describing infinite dilution often need to be extrapolated from experimental phase equilibrium data. Liquid activity models, such as UNIFAC or the Margules equation, are often well suited for such a problem [6]. One drawback to a standard group-contribution approach is that it does not take into account the thermodynamic implications of different isomeric structures. This is a particularly significant shortcoming, as many nanoparticles have several isomeric forms that can have unique wetting properties. For instance, a curved surface typically has a Gibbs free energy of

solvation (ΔG^{solv}) that is about 30% of the corresponding flat surface value [7]. Therefore, it would follow that C_{60} would be considerably less hydrophobic than a 60 particle graphene sheet. Given the sensitivity of wetting properties to particle shape and the multitudes of isomeric structures for many nanoparticles, the application of a group-contribution method is inherently limited. However, if shape and energy parameters are defined for the entire bare nanoparticle unit, as opposed to small groups of atoms, the error due to this simplification can be minimized. Although this is contrary to one of the main intentions of the UNIFAC method, specifically parameterizing volume, area, and energy factors for a given nanoparticle may sufficiently distinguish it from an isomer. Binary interaction energies can be obtained from *ab initio* supermolecule calculations [8], that include the entire bare nanoparticle unit and the given solvent group. UNIFAC shape factors can be obtained from Connolly surface areas [9, 10] and excluded volume calculations.

Due to the highly modifiable nature of many nanoparticles, many variants will be of interest for various applications. The ability to use a simple group-contribution method to calculate various solvation parameters, such as γ^{∞} and $\log K_{O/W}$, would greatly assist in providing thermodynamic parameters for such a large array of particles. In this work, the $K_{O/W}$ parameter for the C_{60} fullerene has been estimated using UNIFAC with standard aromatic carbon parameters, which gives results that lie within range of experimental and theoretical studies. The methodology is extended to the H-POSS nanoparticle, where, due to the lack of experimental data, binary interaction parameters between H-POSS and solvent groups must be calculated by *ab initio* methods. Thermodynamic integration studies of $C_{60}(OH)_{32}$, H-POSS, OH-POSS, and F-POSS in

water were also performed in order to obtain ΔG^{solv}. It was found that attaching hydrophilic groups, such as –OH, to the bare nanoparticle surface resulted in a significant shift towards hydrophilicity. The application of the UNIFAC method towards these systems also indicates a strong hydrophilic shift, further confirming the applicability of UNIFAC to dilute nanoparticle systems.

Methodology

The UNIFAC-FV group-contribution model

Using liquid phase equilibria expressions, the $K_{O/W}$ of a compound can be estimated if γ^{∞} is known for both phases, as shown below. We begin with the standard equations for liquid-liquid equlibria for octanol and water containing a solute dissolved in both phases. Focusing on the solute U, if the mole fraction of U in the octanol-rich liquid phase is $x_U^{octanol}$ and the mole fraction of U in the water-rich phase is x_U^{water}, then equilibrium requires that

$$\gamma_U^{octanol} x_U^{octanol} f_U^0 = \gamma_U^{water} x_U^{water} f_U^0 \tag{4.2}$$

where f_U^0, the standard state fugacity of the solute, is the same for both phases, and $\gamma_U^{octanol}$ and γ_U^{water}, are the activity coefficients of the solute in the octanol-rich and water-rich phases, respectively. $K_{O/W}$ can be calculated by rearranging Equation 4.3 to give

$$K_{O/W} = \frac{x_U^{octanol}}{x_U^{water}} = \frac{\gamma_U^{water}}{\gamma_U^{octanol}} \tag{4.3}$$

In principle, $x_U^{octanol}$ and x_U^{water} will be computed as part of an overall liquid-liquid equilibrium calculation, in which three equations (Equation 4.2 plus two additional equations similar to Equation 4.2, but for octanol and water) are solved. Under the assumptions that the water-rich phase contains no octanol, and the octanol phase contains no water, and that the solute is at low dilution in each phase, we can approximate Equation 4.2 by

$$K_{O/W} = \frac{\gamma_U^{\infty,water}}{\gamma_U^{\infty,octanol}} \tag{4.4}$$

where $\gamma_U^{\infty,octanol}$ and $\gamma_U^{\infty,water}$ are the activity coefficients of the solute at infinite dilution in pure octanol and pure water respectively.

The standard UNIFAC model simplifies the calculation of the activity coefficient of a chemical species in a mixture using a linear combination of two contributions, the combinatorial contribution (γ_i^C), which accounts for the size of the molecules in the system, and the residual contribution (γ_i^R), which accounts for the intermolecular interactions. The standard UNIFAC formulation is as follows

$$\ln \gamma_i = \ln \gamma_i^C + \ln \gamma_i^R \tag{4.5}$$

where the combinatorial term takes the following form

$$\ln \gamma_i^C = \ln \frac{\Phi_i}{x_i} + \frac{z}{2} q_i \ln \frac{\theta_i}{\Phi_i} + l_i - \frac{\Phi_i}{x_i} \sum_j x_j l_j \tag{4.6}$$

and the residual term takes the form.

$$\ln \gamma_i^R = q_i \left[1 - \ln \left(\sum_j \theta_j \tau_{ji} \right) - \sum_j \left(\frac{\theta_j \tau_{ij}}{\sum_k \theta_k \tau_{kj}} \right) \right] \tag{4.7}$$

$$l_i = \frac{z}{2}(r_i - q_i) - (r_i - 1) \tag{4.8}$$

$$\theta_i = \frac{q_i x_i}{\sum_j q_j x_j}; \quad \Phi_i = \frac{r_i x_i}{\sum_j r_j x_j} \tag{4.9}$$

$$\tau_{ji} = e^{-\left[\frac{u_{ji} - u_{ii}}{RT}\right]} \tag{4.10}$$

In these equations, x_i is the mole fraction of species i, z is a constant commonly taken as 10, and τ_{ij} is a binary interaction parameter between groups i and j, which is commonly obtained by fitting to experimental data. The group shape parameters, r_i and q_i represent molecular volume and area respectively, and are calculated from the following expressions

$$r_i = \sum_k \nu_k R_k; \quad q_i = \sum_k \nu_k Q_k \tag{4.11}$$

where R_k and Q_k are the group volume and area for group k, and ν_k is an integer that describes how many times group k appears in molecule i. The group shape parameters are often estimated by van der Waals group volume and area as proposed by Bondi [11].

Ab initio calculations

The binary interaction parameters between functional groups used in group-contribution methods are generally conditional on the availability of experimental phase equilibria data for mixtures containing the needed functional groups. However, for many systems, no such data exists. Nanoparticle systems, in particular, are underrepresented in terms of

phase equilibria, as unusually strong solute-solute interactions result in large aggregates, which often do no reflect the true phase behavior of the solute [12-14]. Additionally, many nanoparticle variants have yet to be studied as a result of their novelty.

The *ab initio* "supermolecule" approach of Sandler et .al [8, 15] is a means by which to obtain energetic binary interaction parameters for use in group-contribution methods, when no fitted parameters are available. This approach has shown improved UNIQUAC phase equilibria predictions for a variety of polar mixtures [15] and greatly improved infinite dilution activity coefficients for binary systems containing water, n-hexane, n-octanol and acetonitrile [16]. The supermolecule consists of a cluster of at least two molecules, with each species of interest being represented. The larger the number of molecules in the cluster, the more representative it is of the bulk solution. To find the interaction energy between groups i and j, $u_{ij,}$ that appears in Equation 4.10, the following expression may be used

$$u_{ij} = E_{ij} - \left(E_i + E_i\right) \tag{4.12}$$

where E_{ij} is the calculated *ab initio* energy of the cluster of molecules i and j, and E_i is the energy of the molecule i from cluster ij, in vacuum. Commonly, *ab initio* cluster calculations are susceptible to so-called basis set superposition error (BSSE) [17]. This occurs when the basis function on molecule j is used to optimize basis functions on molecule i, and vice versa, resulting in an artificially low cluster energy. The counterpoise correction accounts for BSSE that is inherent in *ab initio* cluster calculations [18]. This method corrects the interaction energy by calculating the energy of the isolated molecules, i and j, with all of the basis functions used in the cluster calculation. This introduces the same, artificial optimization of orbitals on the lone molecules that is

present in the cluster calculations. Therefore, when Equation 4.12 is applied with this correction, the errors associated with BSSE should cancel. The following expression describes the *ab initio* interaction energy with the counterpoise method applied

$$u_{ij} = E_{ij}\{i \cdot j\} - E_i\{i \cdot j\} - E_j\{i \cdot j\} \tag{4.13}$$

where the notation $\{i \cdot j\}$ indicates that all of the basis functions from the ij cluster calculation are being used.

All first principles calculations in this work are carried out using the NWChem software package [19]. Given, the size of some of the nanoparticle clusters studied, careful consideration was needed to obtain an optimum between the efficiency of the calulation, and the accuracy of the interaction energies. The geometry of each cluster is optimized with the MP2 level of theory and the 6-31G basis set. Once an optimized cluster geometry is obtained, the cluster and individual molecule energies are obtained using the MP2 level of theory with a minimum of the 6-311++G** basis set with the counterpoise correction method [17]. The binary interaction energy is then calculated by comparing the cluster energy to the combined energies of the isolated molecules in the cluster. Since the calculations in this work require first principle calculations of large nanoparticle systems, only the minimum requisite of two molecules per cluster are calculated, as adding more particles is computationally infeasible. The water molecule is also treated as a single group, which is in accordance with common UNIFAC parameterization. The octanol molecule is broken up into a methanol (CH_3OH) and methane (CH_4) groups. The methanol group describes the terminal alcohol unit in octanol and methane group describes the methyl/methylene units in octanol.

Thermodynamic integration technique

One major hurdle in establishing group-contribution methods as an effective tool for calculating $K_{O/W}$ parameters for nanoparticle systems is the general lack of solubility data. Some work correlating the solubility of a bare C_{60} using QSPR [20, 21] has been published, along with some experimental partitioning data of the C_{60} and C_{70} fullerene in water [22] and C_{60} in organic solvents [23]. However, solubility data for novel nanoparticles, such as POSS, or functionalized fullerenes is very limited. In order to verify that group-contribution techniques can adequately model systems of nanoparticles at infinite dilution, an alternate means of estimating nanoparticle solubility is desirable. In this work, the Gibbs free energy of solvation (ΔG^{solv}) for three POSS variants ($(SiO_{1.5}H)_8$ referred to as H-POSS, $(SiO_{1.5}F)_8$ referred to as F-POSS, and $(SiO_{1.5}OH)_8$ referred to as OH-POSS), and $C_{60}(OH)_{32}$ in a water solvent have been calculated using molecular dynamics simulations and thermodynamic integration (TI) [5]. Figure 4.1 shows the nanoparticle variants in the TI study.

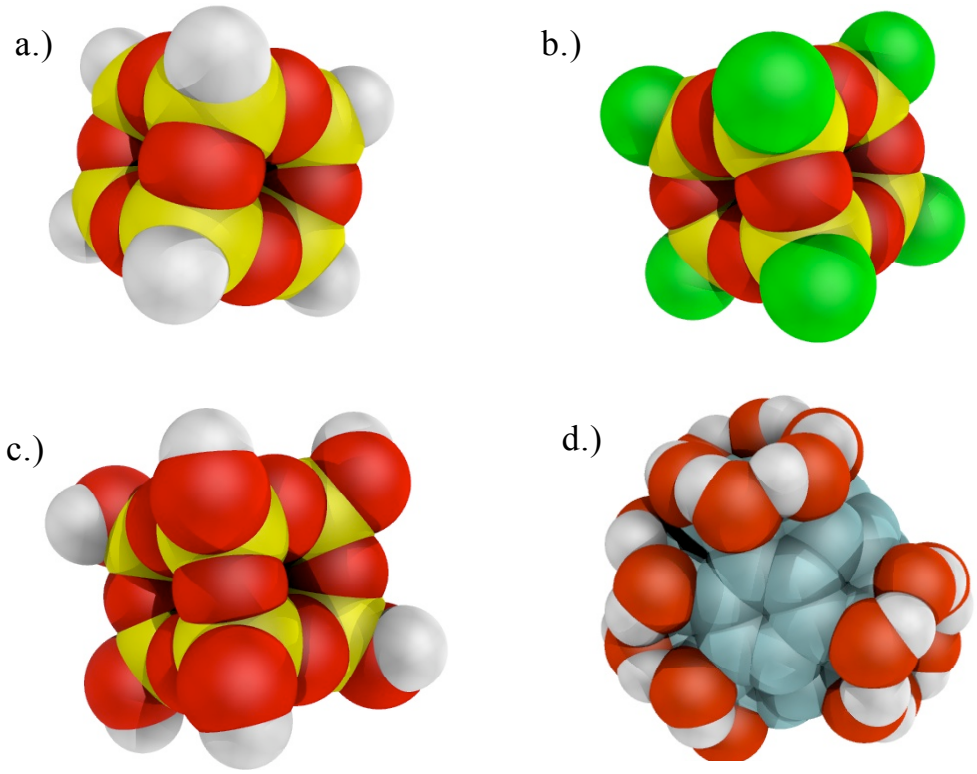

Figure 4.1: Nanoparticles in TI study a.) H-POSS b.) F-POSS, c.) OH-POSS d.) $C_{60}(OH)_{32}$

The simulations were performed in the NPT ensemble, in which the number of particles (N), the system pressure (P), and the system temperature (T) are constant. In order to maintain ambient conditions at which many $K_{O/W}$ studies are performed, the system pressure is held constant at 1 bar and the temperature at 298K. In an NPT system, the ΔG^{solv} can be expressed as follows

$$\left(\frac{\partial G}{\partial \lambda}\right)_{N,P,T} = \left\langle \frac{\partial U}{\partial \lambda} \right\rangle_{\lambda} \tag{4.14}$$

so that,

$$\Delta G^{solv} = \int_0^1 \left(\frac{\partial G}{\partial \lambda}\right)_{N,P,T} d\lambda = \int_0^1 \left\langle \frac{\partial G}{\partial \lambda} \right\rangle_{\lambda} d\lambda \tag{4.15}$$

where U is the potential between the solute and solvent and λ is an arbitrarily defined variable that is defined such that $\lambda = 0$ represents a pure solvent state and $\lambda = 1$ represents a full nanoparticle in solution. All intermediate values of λ indicate a "ghost" state for the solute particle, in which the solvent-solute interactions are softened. Therefore, ΔG^{solv} can be derived given an explicit form of the solvent-solute potential, which decays to 0 at $\lambda = 0$ and reduces to the standard potential form at $\lambda = 1$, and the resulting trajectories from MD simulations.

When possible, a CHARMM compatible forcefield was used to model the systems [24]. The CHARMM forcefield was chosen due to the fact that it has been extended to a wide array of compounds, which eliminates the need to mix forcefields. Additionally, due in large part to its explicit atom nature, CHARMM is considered superior to most common force fields in terms of phase equilibria calculations [25]. In all simulations, the TIP3P force field [26] was used to model water, as it is the only water potential optimized for CHARMM. For systems with a POSS solute, a CHARMM compatible force field for silica/water systems [27] was used to model the inner cage, using surface type III parameters for the oxygen atom. For the functionalized groups in POSS, the CHARMM fluorocarbon potential [28] was used to model van der Waals interactions of the fluorine group and the CHARMM22 force field for lipids [24] was used to model the van der Waals interactions of the functional groups for H-POSS and OH-POSS.

Since there is no CHARMM parameterization for graphitic materials, the potential of Jiang and Sandler [29], which utilizes the Bojan/Steel force field for graphene atoms [30] and the TraPPE force field [31] hydroxyl groups, was used for

applied to the $C_{60}(OH)_{32}$ simulations. When cross terms were unavailable, Berthelot mixing rules were employed, shown below.

$$\sigma_{ij} = \frac{\sigma_i + \sigma_j}{2}; \varepsilon_{ij} = \sqrt{\varepsilon_i \varepsilon_j} \tag{4.16}$$

It has been shown that allowing conformational changes in the solute can lead to significant noise in the thermodynamic integration [32], therefore, all solutes in this study have been fixed rigidly in the center of the simulation cell. The lowest energy configuration for each nanoparticle was found using a DFT level optimization with a minimum 6-31G basis set and a B3LYP exchange/correlation functional. The $C_{60}(OH)_{32}$ particle is believed to exhibit several hydroxyl adsorption patterns on its surface. For this work, the lowest energy $C_{60}(OH)_{32}$ structure, calculated by Rodriguez-Zavala et al. [33], was used for the initial configuration for the DFT optimization.

Most of the solutes in this study have no corresponding electrostatic force field parameters. Using the DFT optimized structures, partial atomic charges were obtained by performing a Mulliken population analysis on a DFT/6-311G** point energy calculation. There is a considerable amount of debate regarding the validity of using the Mulliken population analysis [34] for the calculation of partial atomic charges instead of other methods [35], which typically base partial charges on the fitting of electrostatic surfaces, such as the ChelpG [36] or Merz-Kollman [37] schemes. However, these methods often fail for large molecules, as they often predict unrealistic charges for atoms that lie far away from the electrostatic potential surface (ESP) [38]. Given the unrealistic charges computed in this work for the nanoparticles of interest using ESP techniques, it seems likely that such methods are inadequate due to an inability to fit the separate inner and

outer surfaces of the cage-like particles; hence, the partial charges in this work are calculated using Mulliken population analysis.

The integration in Equation 4.15 was performed in two steps. First, the van der Waals interactions between the solute-and solvent were grown in, with no solute partial charges, using the following modified 12-6 LJ potential [39]

$$U_{ij}^{LJ}(r,\lambda_1) = \lambda_1^n 4\varepsilon_{ij}\left(\frac{1}{\left[\alpha_{LJ}\left(1-\lambda_1^2\right)^2+\left(\frac{r}{\sigma_{ij}}\right)^6\right]^2}-\frac{1}{\alpha_{LJ}\left(1-\lambda_1^2\right)^2+\left(\frac{r}{\sigma_{ij}}\right)^6}\right) \tag{4.17}$$

where r is the distance between particles i and j λ_1 is the van der Waals softening parameter defined before, ε_{ij} is the well depth of the LJ interaction between particles i and j, σ_{ij} is the interaction radius between particles i and j, α_{LJ} is a positive constant, chosen to be 0.25 and n is an integer, chosen to be 2. This particular modification was chosen, as it gives finite energies at low distances for soft potentials, minimizing numerical instabilities. The thermodynamic analyses tend to be very sensitive to changes in λ_1 at soft potentials, therefore, for $\lambda_1 \le 0.5$, an increment of 0.05 is used, whereas for $\lambda_1 > 0.5$, an increment of 0.10 is used. The solvent-solute electrostatic contribution is calculated, with full van der Waals interactions, using a simple variation of the point-point Coulombic interaction

$$U_{ij}^{elec}(r,\lambda_2) = \lambda_2^n \frac{q_i q_j}{r} \tag{4.18}$$

where λ_2 is the electrostatic softening parameter. Since $\left\langle \frac{dU^{elec}}{d\lambda} \right\rangle_{\lambda}$ is generally less sensitive relative to λ_2, λ_2 is sampled in increments of 0.10 over $0.1 \le \lambda_2 \le 1.0$. Using Equations 4.15, 4.17, and 4.18 the ΔG^{solv} can be calculated as follows

$$\Delta G^{solv} = \int_0^1 \left\langle \frac{dU^{vdW}}{d\lambda_1} \right\rangle_{\lambda_1, \lambda_2 = 0} d\lambda_1 + \int_0^1 \left\langle \frac{dU^{elec}}{d\lambda_2} \right\rangle_{\lambda_1 = 1, \lambda_2} d\lambda_2 \qquad (4.19)$$

where λ_1 is the vdW interaction softening parameter, λ_2 is the electrostatic softening parameter, and the $\langle \cdots \rangle$ denotes the time average of the summation of all solute-solvent interactions. For both the vdW and electrostatic analyses, each data point is sampled over a 1 ns MD run and the equations of motion are integrated using the DL_POLY [40] program.

Results and Discussion

Application of ab initio supermolecule/UNIFAC method of computing $K_{O/W}$ for alkanes and alcohols

Table 4.1 shows interaction energies for UNIFAC alcohol and water groups, as calculated using the *ab intio* supermolecule technique.

Cluster	$\Delta E_{A \cdot B}\left(\frac{kcal}{mol}\right)$
MeOH•MeOH	-5.07
MeOH•CH_4	-0.520
MeOH•H_2O	-5.17
CH_4• CH_4	-0.150
CH_4• H_2O	~0
H_2O • H_2O	-5.77

Table 4.1: Interaction energies for water and alcohol groups

The $\log K_{O/W}$ obtained from Equation 4.3, with infinite dilution activity coefficients calculated using the UNIFAC method with binary energy parameters computed using the supermolecule calculations (Table 4.1) for alkanes and alcohols are shown in Figures 4.2a and 4.2b. Also shown for comparison are experimental results and results from several dedicated $\log K_{O/W}$ algorithms [41].

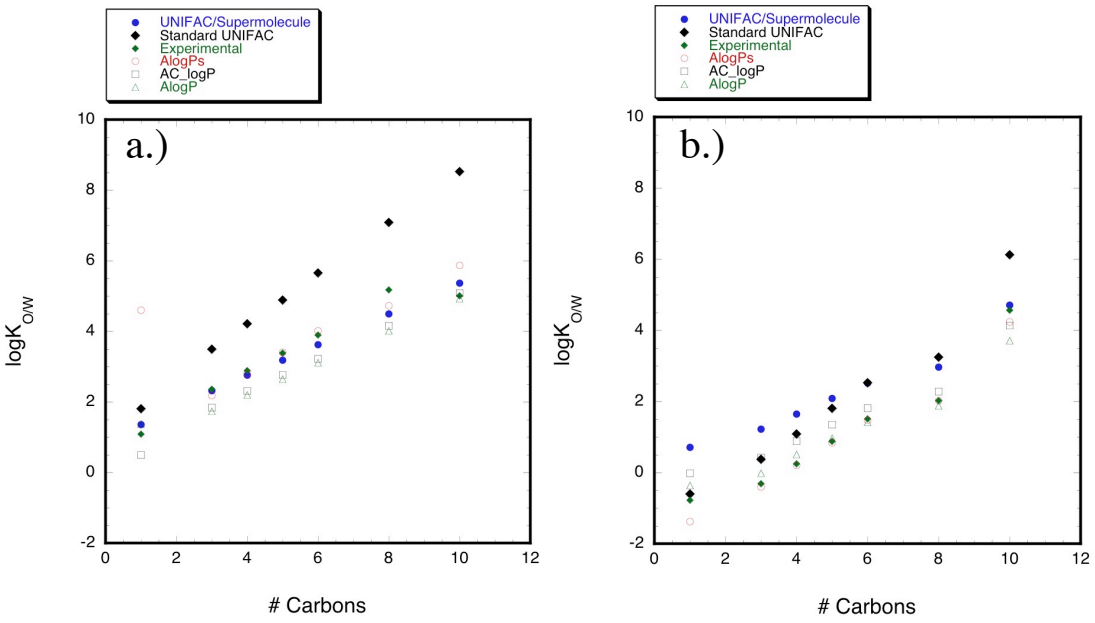

Figures 4.2a and 4.2b: Comparison of calculated $\log K_{O/W}$ values for (a) linear alkanes and (b) normal alcohols as a function of carbon number

Figure 4.2a shows that the UNIFAC method with binary interaction parameters derived from *ab initio* supermolecule studies predicts $\log K_{O/W}$ values for linear alkanes that are in better agreement with the experimental values than the other techniques considered. The agreement with experiment may be due to the fact that the alkane solutes are only composed of one group, thus reducing errors due to UNIFAC's inability to distinguish between isomers. However, it is shown that the standard UNIFAC calculation produces generally poor results, which diverge away from experimental values as the alkane chain becomes larger. Figure 4.2b illustrates that, for small alcohol solutes, the supermolecule UNIFAC study predicts octanol-water partitioning that deviates by 1 order of magnitude from experiment. As the carbon chain of the solute alcohol becomes larger, the calculated $\log K_{O/W}$ values converge towards the experimental $\log K_{O/W}$, with the calculated value for decanol being closer to experiment than any other. This limitation tends to indicate

that the methanol binary interaction energies may not be fully representative of methanol interactions in the bulk phase. Methanol, as opposed to methane, will form a very defined, hydrogen bonded, structure with other polar molecules. When in a bulk system, these hydrogen bonds may be disrupted by competing interactions of neighboring molecules and, as a result, a simple binary cluster may overpredict the attractive energy between two polar molecules. Since binary clusters cannot account for structure defects due to the energetics of many interacting molecules, the binary interaction energies involving polar species may be over estimated. However, the $\log K_{O/W}$ predictions for larger solutes, which are the focus of this work, are satisfactory.

Application of UNIFAC to C_{60} in octanol and water systems

Despite the well-known hydrophobicity of C_{60}, the $\gamma^{\infty}_{C_{60}/water}$ appears high. However, the values are more conservative than those predicted from prediction from regular solution theory [43]. Using the heat of complete vaporization and specific volume data for C_{60} [44, 45] and the solvents [46, 47], regular solution theory gives $\gamma^{\infty}_{C_{60}/water} = 4.5\text{x}10^{59}$ and $\gamma^{\infty}_{C_{60}/octanol} = 362.3$. Additionally, considering the favorable ΔG^{solv} of C_{60} in octanol [42], the $\gamma^{\infty}_{C_{60}/octanol}$ also seems unreasonably high. The large values of $\gamma^{\infty}_{C_{60}/water}$ and $\gamma^{\infty}_{C_{60}/octanol}$ are directly attributable to the large negative solute-solute energy ($u_{ii} = u_{C_{60}C_{60}}$) appearing in Equation 4.10. The value of $u_{C_{60}C_{60}}$ affects both $\gamma^{\infty}_{C_{60}/water}$ and $\gamma^{\infty}_{C_{60}/octanol}$; however, the ratio of the two, yielding $K_{O/W}$, is independent of $u_{C_{60}C_{60}}$. Hence, the value of $K_{O/W}$ reported is being diven by solute-solvent interactions.

UNIFAC/supermolecule analysis of H-POSS and water/octanol systems

The binary interaction parameters for a H-POSS system in water or octanol solvents have been parameterized using the ab initio supermolecule approach. The area (Q_k) and volume (R_k) factors were obtained by calculating the Connolly area and the excluded volume [49], respectively; where $Q_k = 6.45 \frac{cm^2}{mol}$ and $R_k = 14.24 \frac{cm^3}{mol}$. Table 4.2 indicates the interaction energies found for all H-POSS complexes.

Cluster	$\Delta E_{A \cdot B} \left(\frac{kcal}{mol} \right)$
H-POSS•H-POSS	-14.23
H-POSS•CH_4	-0.68
H-POSS•MeOH	-3.24
H-POSS•H_2O	-3.18

Table 4.2: Interaction energies for H-POSS

It is seen that H-POSS interacts quite favorably with groups that have polar constituents, such as water or methanol. However, the interaction energy between two H-POSS particles is far greater, indicating that H-POSS system may also be subject to solute-solute interaction artifacts in infinite dilution calculations. A UNIFAC analysis of H-POSS in water yields $\gamma^{\infty}_{POSS/water}$ = 1.00x10^{66} and $\gamma^{\infty}_{POSS/octanol}$ = 1.19x10^{55}, resulting in a $\log K_{O/W} = 10.9$.

Calculation of ΔG^{solv} for benzene in water using Mulliken Charges

As a test of our molecular-simulation based methodology for computing $K_{O/W}$, we compute ΔG^{solv} for benzene in water using thermodynamic integration with the CHARMM force field and electrostatics for benzene derived from a DFT/6-311G** Mulliken population analysis. The ΔG^{solv} for benzene in water has been calculated using thermodynamic integration with the CHARMM force field and electrostatics for benzene derived from a DFT/6-311G** Mulliken population analysis. Since the solubility of benzene in water is well known, the accuracy of the calculation should indicate the efficacy of using Mulliken partial charges in a TI study. The resulting partial charges are shown in Table 4.3

CHARMM atom name	**(Mulliken)** q_i	**GROMOS 43A1** q_i [50]	**GROMOS 53A6** q_i [51]
CA	-0.15	-0.10	-0.14
HP	0.15	0.10	0.14

Table 4.3: Mulliken partial charges for benzene

Table 4.3 shows that the Mulliken partial charges are comparable to that of the GROMOS potential, and in particular, close in value to the recent GROMOS 53A6 parameterization. A 250 ps thermodynamic integration of a CHARMM benzene with Mulliken partial charges produces the vdW and electrostatic TI curves, shown in Figure 4.3.

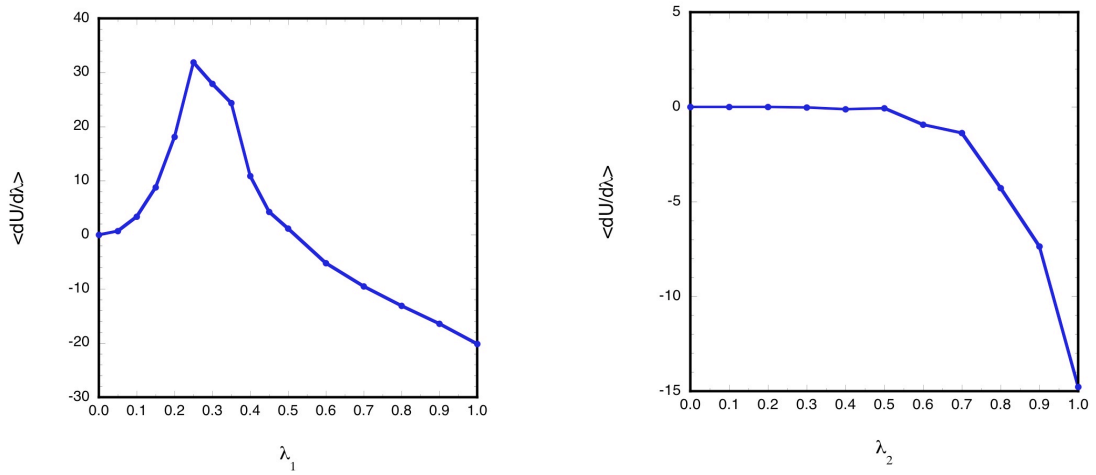

Figure 4.3: TI curves for CHARMM benzene with Mulliken charges a) step 1 b)step 2

Integrating (Figure 4.3a) over λ_1 yields the first term in Equation 4.19, resulting in a $\Delta G_{vdW}^{solv} = +1.29$ kcal/mol, where integrating Figure 4.3b over λ_2 gives a $\Delta G_{Coulombic}^{solv} =$ - 2.03 kcal/mol. Therefore, $\Delta G^{solv} = -0.74\ kcal/mol$, which is in better agreement with the experimental value of $\Delta G^{solv} = -0.86\ kcal/mol$, than either GROMOS 43A1 $\Delta G^{solv} = -1.15\ kcal/mol)$ or GROMOS 53A6 ($\Delta G^{solv} = -1.60\ kcal/mol)$[52].

Solubility response associated with adding hydrophilic groups using thermodynamic integration and UNIFAC

The partial charges for a $C_{60}(OH)_{32}$ were parameterized using a Mulliken population analysis in order to carry out a thermodynamic integration of the particle in a water solvent. The partial charges are documented in Table 4.4, along with the partial charges for similar atoms in a TraPPE alcohol molecule, in an effort to compare the parameterization to an established potential.

Atom	Mulliken q_i	TraPPE q_i
CAd	0.09000	0.00
CB	0.26125	0.265
O	-0.73000	-0.700
H	0.39000	0.435

Table 4.4: Comparison of Mulliken $C_{60}(OH)_{32}$ partial charges and TraPPE partial charges

In Table 4.4, CB represents a carbon atom bonded to an oxygen atom and CAd is a carbon atom bonded to a CB, but not bonded to an oxygen atom. Despite the often-cited limited applicability of the Mulliken technique [53] and the fundamental differences between the hydroxyl group on a fullerenol and the hydroxyl group on a normal alcohol, the partial charges are quite comparable.

The thermodynamic integration of $C_{60}(OH)_{32}$ in water yields a $\Delta G_{elec}^{solv} = +8.11 \frac{kcal}{mol}$ and a $\Delta G_{vdW}^{solv} = -53.00 \frac{kcal}{mol}$, resulting in a $\Delta G^{solv} = -44.89 \frac{kcal}{mol}$. This result is in accordance with experimental studies suggesting that fullerenols with more than 12 hydroxyl groups are water soluble [54, 55]. Therefore, the lowered energy of solvation relative to the undecorated C_{60} is due solely to more favorable solvent-solute interactions. A UNIFAC analysis of a $C_{60}(OH)_{32}$ in water yields a $\gamma_{C_{60}(OH)_{32}}^{\infty,water} = 1.88 \gamma^{\infty}_{\text{C60(OH)32/water}} = 1.88$, which is in stark contrast to the bare fullerene solubility. This response is at least a qualitative indicator that the UNIFAC method can distinguish between strongly hydrophobic and hydrophilic fullerenes.

A similar thermodynamic integration analysis has been done for H-POSS, F-POSS, and OH-POSS. Table 4.5 summarizes the partial charges found from the Mulliken population analysis.

Atom	H-POSS	F-POSS	OH-POSS
Si	1.19000	0.21005	0.57505
OP	-0.64000	-0.06670	-0.27170
HP	-0.23000	N/A	N/A
FP	N/A	-0.11000	N/A
O	N/A	N/A	-0.44500
H	N/A	N/A	0.27750

Table 4.5: Mulliken partial charges for H-POSS, F-POSS, and OH-POSS

The thermodynamic integration study produced solvation energies for H-POSS, F-POSS, and OH-POSS, shown in Table 4.6. Also given are γ^{∞} calculated from UNIFAC for each particle in a water solvent.

Solute	ΔG_{vdW}^{solv} (kcal/mol)	ΔG_{elec}^{solv} (kcal/mol)	ΔG^{solv} (kcal/mol)	γ^{∞}
H-POSS	-6.78	-2.04	-8.82 +/- 3.9	1.00×10^{66}
OH-POSS	-7.51	-12.43	-19.94 +/- 4.5	1.02×10^{54}
F-POSS	-9.02	-1.96	-10.96 +/- 3.1	1.65×10^{66}

Table 4.6: Solubility parameters for POSS molecules in H_2O

The UNIFAC predictions are crude estimations, as there are no binary interaction parameters for the intramolecular interactions between POSS and the functional groups. As an approximation, the POSS•H_2O interaction was used for the POSS•OH interaction,

and the POSS•CH_4 interaction for the POSS•F interaction. All other UNIFAC interactions were available from either the supermolecule calculation or from experimental fitting [56]. The approximations were used because the H_2O•OH and CF•CH_4 binary interaction parameters were relatively close to 0. The UNIFAC calculation reflects the increase of relative solubility of OH-POSS in water in comparison to that of H-POSS, which in agreement with the thermodynamic integration analysis. However, the UNIFAC analysis is unable to indicate the more subtle shift in relative solubility in water from H-POSS to F-POSS, as shown in the thermodynamic integration analysis.

Conclusions

The ability of the UNIFAC group contribution method to accurately estimate the $\log K_{O/W}$ for C_{60} and H-POSS. It was found that the UNIFAC method gives estimations of $\log K_{O/W}$ for C_{60} that are comparable to theory and experiment. Additionally, thermodynamic integration studies were performed on $C_{60}(OH)_{32}$, H-POSS, F-POSS, and OH-POSS in water using parameterizations from *ab initio* studies. The hydrophilic shift from the base nanoparticle unit to the functionalized particle was tested with both the thermodynamic integration method and the UNIFAC method. For particles with significant water association, such as $C_{60}(OH)_{32}$ and OH-POSS, both techniques indicate significant shifts in hydrophilicity from their base counterparts. In the instance of the F-POSS/water system, the subtle hydrophilic shift from H-POSS that was shown in the thermodynamic integration was not captured in the UNIFAC analysis. This shortcoming

may be due to the approximations used to model the F-POSS/water system in UNIFAC, or simply the inability of UNIFAC to distinguish between such similar solutes.

The results of these findings present a fast, simple, and inexpensive means of obtaining $\log K_{O/W}$ for nanoparticle systems. The methodology is not meant to replace theoretical or experimental means of obtaining $\log K_{O/W}$ values for nanoparticle systems; rather, it is to be used as a tool to quickly estimate octanol/water partitioning for novel, functionalized nanoparticles. Given the rate at which new nanoparticle variants are being synthesized, this is a powerful tool in terms of tuning the solubility of new particles.

References

1. Roco, M.C., *International perspective on government nanotechnology funding in 2005*. Journal of Nanoparticle Research, 2005. 7: p. 707-712.

2. Fredenslund, A., Jones Russell L., and Prausnitz, John M., *Group-Contribution Estimation of Activity Coefficients in Nonideal Liquid Mixtures*. AIChE Journal, 1975. 21(6): p. 1086-1099.

3. Hansch, C., and Leo, Albert, *Substituent Constants for Correlation Analysis in Chemistry and Biology*. 1979, New York: John Wiley and Sons.

4. Tetko, I.V., Tanchuk, Vsevolod Yu., and Villa, Alessandro E.P., *Prediction of n-Octanol/Water Partition Coefficients from PHYSPROP Database Using Artificial Neural Networks and E-State Indices*. J. Chem. Inf. Comput. Sci., 2001. 41(5): p. 1407-1421.

5. Frenkel, D., and Smit, Berend, *Understanding Molecular Simulation:From Algorithms to Application*. Computational Science Series. Vol. 1. 2002, San Diego: Academic Press.

6. Smith, F.L., and Harvey, Allan H., *Avoid Common Pitfalls when Using Henry's Law*. Chemical Engineering Progess, 2007. Sept.: p. 33-39.

7. Moore, J.W., and Pearson, Ralph G., *Kinetics and Mechanism*. 1981: John Wiley and Sons.

8. Wu, H.S., and Sandler, Stanley I., *Use of ab Initio Quantum Mechanics Calculations in Group Contribution Methods. 1. Theory and the Basis for Group Identifications*. Ind. Eng. Chem. Res., 1991. 30(5): p. 881-889.
9. Connolly, M.L., *Solvent-Accessible Surfaces of Proteins and Nucleic Acids*. Science, 1983. 221(4612): p. 709-713.

10. Richards, F.M., *Areas, Volumes, Packing, and Protein Structure*. Ann. Rev. Biophys. Bioeng., 1977. 6: p. 151-176.

11. Bondi, A.A., *Physical Properties of Molecular Crystals, Liquids, and Gases*. 1968, New York: Wiley.

12. Chen, B., Siepmann, J. Ilja, Karaborni, Sami, and Klein, Michael L., *Vapor-Liquid and Vapor-Solid Equilibrium of Fullerenes: The Role of the Potential Shape on the Triple Point*. J. Phys. Chem. B., 2003. 107(44): p. 12320-12323.

13. Hagen, M.H.J., Meijer, E.J., Mooij, G.C.A.M., Frenkel, D., and Lekkerkerker, H.N.W., *Does C60 have a liquid phase?* Nature, 1993. 365: p. 425-426.

14. Brant, J., Locanet, Helene, and Wiesner, Mark R., *Aggregation and deposition characteristics of fullerene nanoparticles in aqueous systems*. Journal of Nanoparticle Research, 2005. 7: p. 545-553.

15. Sum, A.K., Sandler, Stanley I., *Use of ab initio methods to make phase equilibria predictions using activity coefficient models*. Fluid Phase Equilibria, 1999. 158-160: p. 375-380.

16. Lin, S.-T., and Sandler, Stanley I., *Infinite Dilution Activity Coefficiets from Ab Initio Calculations*. AIChE Journal, 1999. 45(12): p. 2606-2618.

17. Simon, S., Duran, Miquel, and Dannenberg, J.J., *How does basis set superposition error change the potential surfaces for hydrogen bonded dimers?* Journal of Chemical Physics, 1996. 105(24): p. 11024-11031.

18. Boys, S.F. and F. Bernardi, *Calculation of Small Molecular Interactions by Differences of Separate Total Energies - Some Procedures with Reduced Errors*. Molecular Physics, 1970. 19(4): p. 553-560.

19. Kendall, R.A., Apra, E., Bernholdt, D.E., Bylaska, E.J., Dupuis, M., Fann, G.I., Harrison, R.J., Ju, J.; Nichols, J.A., Nieplocha, J., Straatsma, T.P., Windus, T.L., and Wong, A.T., *High Performance Computational Chemistry: An Overview of NWChem a Distributed Parallel Application*. Computer Phys. Comm., 2000. 128: p. 260-283.

20. Marcus, Y., Smith, Allan L., Korobov, M.V., Mirakyan, A.L., Avramenko, N.V, and Stukalin, E.B., *Solubility of C60 Fullerene*. J. Phys. Chem. B., 2001. 105(13): p. 2499-2505.
21. Hansen, C.M., and Smith, Allan L., *Using Hansen solubility parameters to correlate solubility of C60 fullerene in organic solvents and polymers*. Carbon, 2004. 42: p. 1591-1597.
22. Heymann, D., *Solubility of Fullerenes C60 and C70 in Water*. Lunar and Planetary Institute, 1996. 27: p. 543-544.
23. Heymann, D., *Solubility of C60 in Alcohols and Alkanes*. Carbon, 1995. 34(5): p. 627-631.
24. Merz, K.M., and Roux, Benoit, *Biological Membranes: A Molecular Perspective from Computation and Experiment*. 1996, Boston: Birkhauser.
25. Martin, M.G., *Comparison of the AMBER, CHARMM, COMPASS, GROMOS, OPLS, TraPPE and UFF force fields for prediction of vapor-liquid coexistence curves and liquid densities*. Fluid Phase Equilibria, 2006. 248(1): p. 50-55.
26. Jorgensen, W.L., Chandrasekhar, Jayaraman,Madura, Jeffry D., Impey, Roger W., and Klein, Michael L., *Comparison of simple potential functions for simulating liquid water*. J. Chem. Phys., 1983. 79(2): p. 926-935.
27. Cruz-Chu, E.R., Aksimentiev, Aleksei, and Schulten, Klaus, *Water-Silica Force Field for Simulating Nanodevices*. J. Phys. Chem. B., 2006. 110(43): p. 21497-21508.
28. Chen, I.J., Yin, Daxu, MacKerell, Alexander D., *Combined Ab initio/Empirical Approach for Optimization of Lennard Jones Parameters for Polar-Neutral Compounds*. Journal of COmputational Chemistry, 2001. 23(2): p. 199-213.
29. Jiang, J., and Sandler, Stanley, I., *Adsorption and phase transitions on nanoporous carbonanceous materials: insights from molecular simulations*. Fluid Phase Equilibria, 2005. 228-229: p. 189-195.
30. Bojan, M.J., and Steele, William A., *Interactions of Diatomic Molecules with Graphite*. Langmuir, 1987. 3(6): p. 1123-1127.
31. Chen, B., Pottoff, Jeffrey J., and Siepmann, J. Ilja, *Monte Carlo Calculations for Alcohols and Their Mixtures with Alkanes. Transferable Potentials for Phase Equilibria. 5. United-Atom Description of Primary, Secondary, and Tertiary Alcohols*. J. Phys. Chem. B., 2001. 105(15): p. 3093-3104.

32. Wescott, J.T., Fisher, L.R., and Hanna, S., *Use of Thermodynamic Integration to calculate the hydration free energy of n-alkanes*. Journal of Chemical Physics, 2001. 116(6): p. 2361-2369.
33. Rodriguez-Zavala, J.G., and Guirado-Lopez, R.A., *Stability of Highly OH-Covered C60 Fullerenes: Role of Coadsorbed O Impurities and the Charge State of the Cage in the Formation of Carbon-Opened Structures*. J. Phys. Chem. A, 2006. 110(30): p. 9459-9468.

34. Mulliken, R.S., *Electronic Population Analysis on LCAO-MO Molecular Wave Functions*. J. Chem. Phys., 1955. 23: p. 1833, 1841, 2338, 2343.

35. Wiberg, K.B., and Rabien, Paul R., *Comparison of Atomic Charges Derived via Different Procedures*. Journal of Computation Chemistry, 1993. 14(12): p. 1504-1518.

36. Breneman, C.M., and Wiberg, Kenneth B., *Determining Atom-Centered Monopoles from Molecular Electrostatic Potentials. The Need for High Sampling Density in Formamide Conformational Analysis*. Journal of Computation Chemistry, 1990. 11(3): p. 361-373.

37. Besler, B.H., Merz, Kenneth M., and Kollman, Peter A., *Atomic Charges Derived from Semiempirical Methods*. Journal of Computational Chemistry, 1990. 11(4): p. 431-439.

38. Martin, F., and Zipse, H., *Charge Distribution in the Water Molecule-A Comparison of Methods*. Journal of Computational Chemistry, 2004. 26(1): p. 97-105.

39. Beutler, T.C., Mark Alan E., van Schaik, Rene C., Gerber, Paul R., and van Gunsteren, Wilfred F., *Avoiding singularities and numerical instabilites in free energy calculations based on molecular simulations*. Chemical Physics Letters, 1994. 222: p. 529-539.

40. Smith, W., and Forrester, T.R., *DL_POLY*. 2003, Daresbury Laboratory: Warrington, England.

41. Tetko, I.V., Gasteiger, J., Todeschini, R., Mauri, A., Livingstone, D., Palyulin. V.A., Radchenko, E.V., Zefirov, N.S., Makerenko, A.S., Tanchuk, V.Y., Prokopenko,, *Virtual computational chemistry laboratory - design and description*. J. Comput. Aid. Mol. Des., 2005. 19(453): p. 453-63.

42. Redmill, P.S., Capps, Shannon C., Cummings, Peter T., and McCabe, Clare, *On the Calculation of the Gibbs Free Energy of Solvation for Fullerene Particles by Molecular Dynamics Simulation*. 2008.

43. Prausnitz, J.M., Lichtenthaler, Rüdiger N., de Azevedo, Edmundo Gomes, *Molecular Thermodynamics of Fluid-Phase Equilibria*. 3rd ed. 1999, Upper Saddle River, NJ: Prentice Hall.

44. Pan, C., et al., *Heats of Sublimation from a Polycrystalline Mixture of C60 and C70*. Journal of Physical Chemistry, 1991. 95(8): p. 2944-2946.

45. David, W.I.F., et al., *Crystal-Structure and Bonding of Ordered C60*. Nature, 1991. 353(6340): p. 147-149.

46. Kulikov, D., S.P. Verevkin, and A. Heintz, *Enthalpies of vaporization of a series of aliphatic alcohols - Experimental results and values predicted by the ERAS-model*. Fluid Phase Equilibria, 2001. 192(1-2): p. 187-207.

47. Felder, R.M., and Rousseau, Ronald W., *Elementary Principles of Chemical Processes*. 3rd ed. 2000, New York, Chichester, Brisbane, Toronto, Singapore: John Wiley & Sons.

48. Marmur, A., *Dissolution and Self Assembly: The Solvophobic/Hydrophobic Effect*. J. Am. Chem. Soc., 2000. 122(9): p. 2120-2121.

49. Pettersen, E.F., Goddard, T.D., Huang, C.C., Couch, G.S., Greenblatt, D.M., Meng, E.C., and Ferrin, T.E., *UCSF Chimera - A Visualization System for Exploratory Research and Analysis*. J. Computational Chemistry, 2004. 25: p. 1605-1612.

50. Berendsen, H.J.C., Postma, J.P.M., van Gunsteren, W.F., and Hermans, J., *Intermolecular Forces*, ed. B. Pullman. 1981, Dordrecht. 331-342.

51. Oostenbrink, C., Villa, Alessandra, Mark, Alan E., and van Gunsteren. William F., *A biomolecular force field based on the free enthalpy of hydration and solvation: The GROMOS force-field parameter sets 53A5 and 53A6*. Journal of Computational Chemistry, 2004. 25(13): p. 1656-1676.

52. Schravendijk, P., and van der Vegt, Nico F.A., *From Hydrophobic to Hydrophilic Solvation: An Application to Hydration of Benzene*. Journal of Chemical Theory and Computation, 2005. 1(4): p. 643-652.

53. DeProft, F., Martin, J.M.L, and Geerlings, P., *On the performance of density functional methods for describing atomic populations, dipole moments and infrared intensities*. Chemical Physics Letters, 1996. 250(3-4): p. 393-401.

54. Liu, W.-J., Jeng, U., Lin, T.-L., Lai, S,-H., Shih, M.C., Tsao, C.-S., Wanf, L.Y., Chiang, L.Y., and Sung, L.P., *Adsorption of doceahydroxylated-fullerene monolayers at the air-water interface*. Physica B, 2000. 2000(283): p. 49-52.

55. Rincon, M.E., Hu, H., Campos, J., and Ruiz-Garcia, J., *Electrical and Optical Properties of Fullerenol Langmuir-Blodgett Films Deposited on Polyaniline Substrates*. J. Phys. Chem. B., 203. 107(17): p. 4111-4117.

56. Gmehling, J., Rasmussen, and Fredenslund, Aage, *Vapor-Liquid Equilibria by UNIFAC Group Contribution. Revision and Extension. 2*. Ind. Eng. Chem. Process Des. Dev., 1982. 21(1): p. 118-127.

CHAPTER V

BEHAVIOR OF SELECTED NANOSCALE BUILDING BLOCKS IN A LIPID BILAYER: A MOLECULAR DYNAMICS STUDY

Introduction

Many toxins function by attacking biological systems at a cellular level and disrupting cellular structure or function, resulting in apoptosis (programmed cell death) or necrosis (abnormal cell death). Toxins can, for example, alter the structure of the cellular membrane, resulting in cell wall loosening and rupture (i.e. cell lysis) [1] or enter the intercellular region and induce abnormal cell function, such as increased mitochondrial function or ATP production [2], inducing apoptosis. Toxins often access the cell via active transport or facilitated diffusion, by mechanisms such as ion channel permeation [3] and binding with transport proteins [4], while some small particles are able to migrate across the cell membrane unassisted.

Partitioning of solutes into a lipid bilayer is a complex process influenced in large part by energetic considerations. By comparing the free energy of solvation in octanol and water phases, qualitative conclusions about the partitioning of particles between aqueous/organic phases can be made, which by extension can provide some insight into the fate of the particles in analogous systems, such as soil/water [5] or tissue/water interfaces [6]. A common parameter used to quantify organic/water partitioning is the octanol-water partition coefficient ($K_{O/W}$). However, $K_{O/W}$ coefficients describing partitioning of a molecule between an isotropic aqueous phase and an isotropic organic phase, such as octanol, may be insufficient to describe the partitioning of the between an

aqueous phase and an anisotropic, semi-ordered organic phase, such as a phospholipids membrane. In the case of a highly structured, heterogeneous membrane, the diffusivity of the particle is dependent on the location within the membrane, which contributes to partitioning behavior. Additionally, complex membrane systems may exhibit many more phases, which have significant effects on solute partitioning, over a relatively small range of conditions. For example, the partitioning of benzene in dimyristoylphosphatidylcholine (DMPC) model bilayer systems decreases by an order of magnitude when the temperature is lowered below the phase transition temperature of 23.5°C [7, 8], which increases the surface density of the bilayer, in turn making the insertion of the solute into the membrane more difficult.By contrast, the partitioning of benzene in an octanol water system only changes by 2.5% when the temperature is lowered from 25°C to 15°C [9]. Due to the fact that octanol, as well as many other isotropic hydrocarbons, does not undergo any significant phase transition between these temperatures, the true partitioning of the solute in the DMPC membrane is lost with a simple $K_{O/W}$ study. Furthermore, it has been suggested that geometric characteristics of the solute, such as molecular volume, will have a fundamental role in passive transport across a structured membrane [10].

In light of the growing interest in incorporating nanoparticles into biological systems for various applications such as MRI contrasting agents [11] and drug delivery [12], the determination of their toxic potential has become a key issue. The particles in this study (Figure 5.1) for example, which were chosen due to their compact size and highly symmetric shape, have been proposed as nanoscale building blocks (NBBs) for many applications, including structural materials, thus significantly increasing the

liklihood of occupational exposure to these nanoparticles. In addition, functionalized versions of the nanoparticles in Figure 5.1 have been proposed as possible HIV protease inhibitors [13], light-mediated DNA cleaving agents [14], dental restorative composites [15], and vascular prostheses [16]. Several studies have shown that these nanoparticles exhibit some toxic traits; buckyballs have been shown to cause oxidative stress in the brain tissue of juvenile large mouth bass [17], bind to and deform DNA fragments [18], and partition significantly in the organic phase of octanol/water systems [19]; and it has been shown that a cationic variant of the POSS molecule can diffuse across the cellular membrane and gain access to the cytosol [20], where it would be hypothetically capable of interfering with intracellular processes.

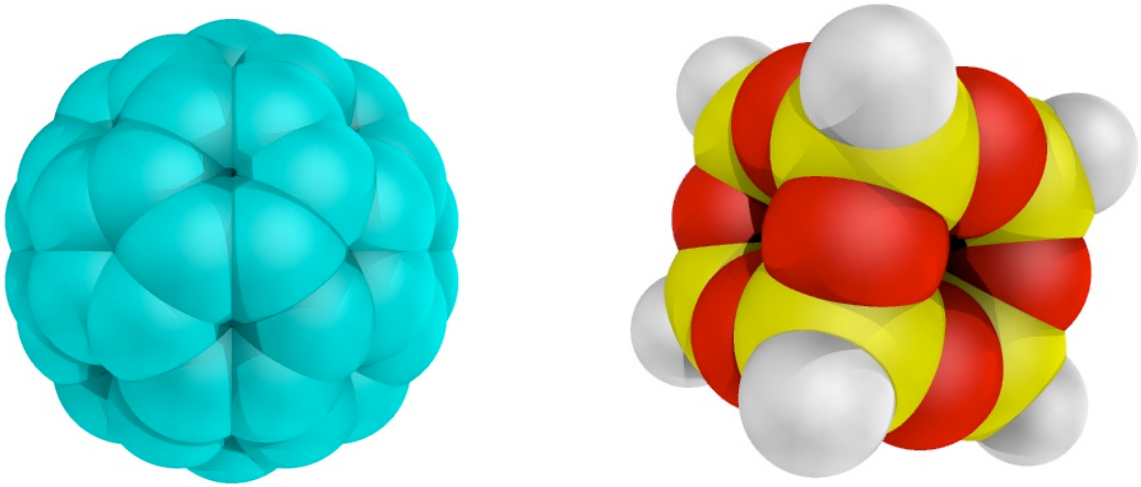

Figure 5.1: C_{60} and H-POSS $(SiO_{1.5})_8$

In this work, the Gibbs free energy required to insert the nanoparticle at various depths normal to the bilayer plane (hitherto referred to as the z direction), ($\Delta G(z)$), has been calculated for these particles in a fully hydrated DPPC (Figure 5.2) bilayer using molecular dynamics (MD) simulations and potential of mean force (PMF) calculations.

The DPPC molecule was chosen since it is commonly used to study model bilayers by molecular simulation[21-26]. The common usage of DPPC is a result of human membranes consisting of over 90% phospholipids, 60% of which is DPPC [27].

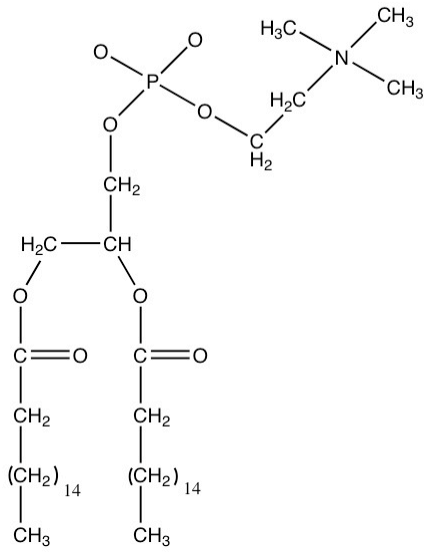

Figure 5.2**:** dipalmitoylphosphatidylcholine

The calculated $\Delta G(z)$ functions describe the partitioning behavior of the particle in the bilayer and therefore providing insight into the likelihood of a C_{60} or H-POSS molecule penetrating the cell. Furthermore, the permeability of the particles can be compared to that of similarly sized polymers and biomolecules, in order to ascertain the significance of solute geometry on bilayer partitioning.

Simulation Details

Molecular dynamics simulations have been performed and potential of mean force calculations used to determine the z-directed Gibbs free energy and diffusivity functions for C_{60} and H-POSS molecules in a fully hydrated DPPC phospholipid bilayer. Bilayer systems are commonly separated into 4 distinct groups along the heterogeneous z axis [28][29] as shown in Figure 5.3.

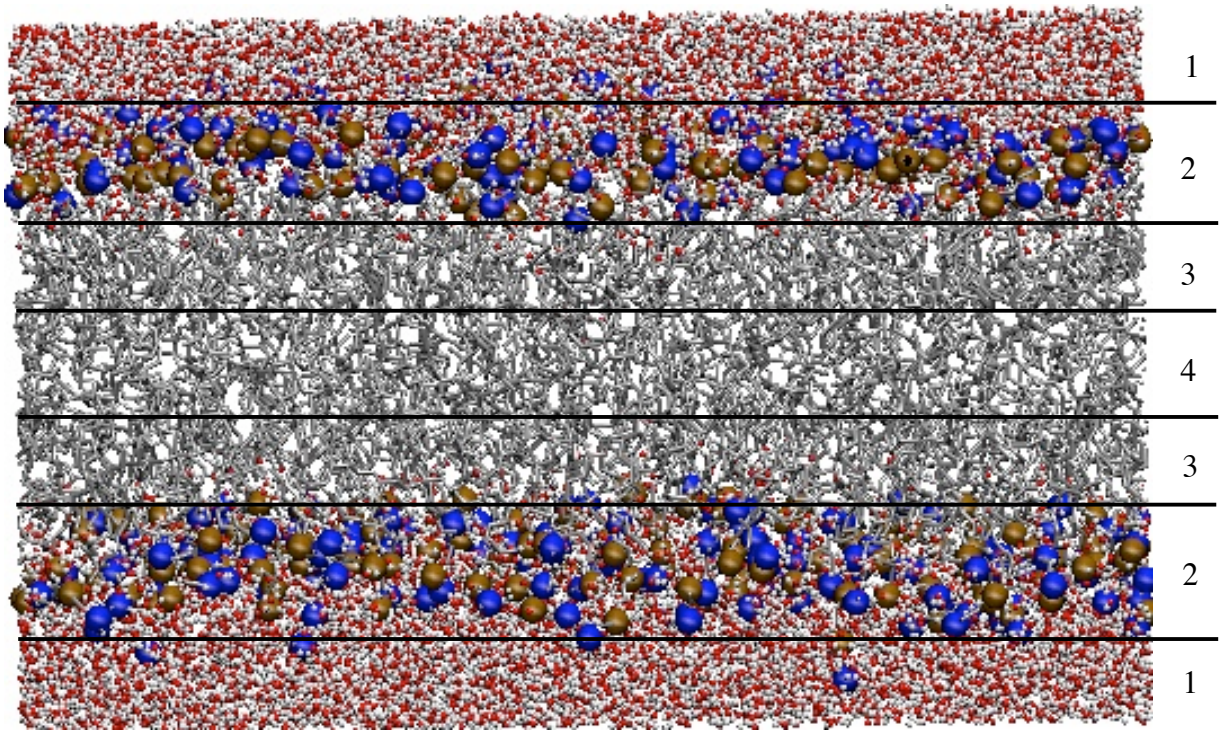

Figure 5.3**:** The four-region model of a fully hydrated DPPC bilayer: water O (red), water H (white), nitrogen head group (blue), phosphorus head group (brown), hydrocarbon chain (silver)

Region 1 is the so called 'perturbed water" region that encompasses the depth from roughly 8Å above the bilayer surface (at which point the water structure is that of bulk water), to the depth where the lipid and water densities become equal. Region 2, the "interfacial" region, is characterized by a dramatic drop in water density and is comprised

primarily of DPPC choline and phosphate groups. Region 3 is the "soft polymer" region, which is also about 8Å thick, and is comprised primarily of partially ordered hydrocarbon chains, starting at the carbonyl groups of the DPPC molecules and extending to the depth where the hydrocarbons are roughly at the density of n-hexadecane. Region 4 is the hydrophobic region and exhibits low structure and a low density, comparable to that of decane.

The overall resistance (R) associated with solute permeation crossing a heterogeneous bilayer of depth dz, defined as the inverse of the permeability coefficient (P), is connected to the diffusivity function, $D(z)$, and $\Delta G(z)$ through the following relations [30]

$$R = \frac{1}{P} = \int_0^d \frac{dz}{K(z)D(z)} \tag{5.1}$$

$$K(z) = e^{\frac{-\Delta G(z)}{RT}} \tag{5.2}$$

where $K(z)$ is the lipid/water partitioning function, which describes the ratio of the concentration of solute in the lipid and in water. The $\Delta G(z)$ function can be obtained by performing a potential of mean force study on the solutes in each of the four regions in Figure 5.3. The potential mean force calculation is performed by fixing the center of mass of the solute at a given z-depth of the bilayer, while the molecule is able to freely translate in the *x* and *y* directions and individual atoms on the solute can move about on the *z*-axis. The forces acting upon individual atoms in the solute can be obtained and, in turn, can provide the force on the center of mass ($\mathbf{F}(z,t)$) required to keep the solute fixed at the chosen depth. The $\Delta G(z)$ function is obtained from Equation 5.3 [31],

$$\Delta G(z) = -\int_{zref}^{z} \left\langle \mathbf{F}(z') \right\rangle_t dz' \tag{5.3}$$

where z_{ref} is the region from which the change in energy will be in reference to, which in this study is region 1 of Figure 5.3 and $\langle \cdots \rangle_t$ indicates a time average. To simplify the calculation of $\mathbf{F}(z,t)$, both the C_{60} and H-POSS structures were held rigid by fixing all intramolecular bonds and angles using the SHAKE algorithm. This simplification is justified, as both H-POSS [32-34] and C_{60} [35, 36] have been found to be somewhat rigid structures. The simulations were performed using the LAMMPS [37] molecular dynamics code, employing the particle-particle-particle mesh method for long-ranged interactions and a velocity-Verlet integrator with an 8Å Lennard-Jones cutoff and a 10Å electrostatic real space cutoff.

The simulations are performed in the NPAT ensemble, in which the number of particles (N), pressure normal to the bilayer (P), cross sectional-area of the bilayer surface (A), and temperature (T) are held constant. In order to accurately model a membrane, either a knowledge of the surface area per lipid or the surface tension of the membrane must be applied [29]; therefore, practically all lipid bilayer simulations use either the NPAT or NPγT ensemble. Since there is a considerable amount of literature debating the appropriate value of the water/membrane surface tension to be applied to NPγT ensembles [23, 38-41], the NPAT ensemble was employed with the well defined constant area of $61.8 Å^2$/lipid [29]. The simulation contained 288 DPPC molecules and 8375 water molecules. In order to mimic ambient conditions, the temperature was held constant at 298.15 K and the pressure was held at 1 atm. The simulations were relaxed for 1 ns, and then the trajectories were sampled over an additional 2.5 ns at 0.5 ps intervals.

The CHARMM27 force field [42] was used to model the hydrated phospholipid system with the standard TIP3P [43] force field to describe the water. To model the C_{60} molecule we used the van der Waals parameters for aromatic carbons in the CHARMM27 force field. For H-POSS, the water-silica force field of Cruz-Chu et. al was used. [44]. This force field was chosen due to the fact it has been optimized to be compatible with the CHARMM force field and has been shown to reproduce wetting characteristics of water on a silica surface, a phenomena that strongly correlates to the Gibbs free energy of solvation (ΔG^{solv}) [45]. Partial atomic charges for H-POSS were obtained using a Mulliken population analysis from a B3LYP-DFT/6-311G** point energy calculation with a structure obtained from a B3LYP-DFT/6-31G geometry optimization. All DFT studies in the work were executed using the NWCHEM program [46]. Geometry and partial charge information for H-POSS are provided in Tables 5.1 and 5.2.

Geometry	r_{ij} **(Å)**	θ_{ijk} **(degrees)**	ϕ_{ijkl} **(degrees)**
Si-O	1.63	-	-
Si-H	1.45	-	-
O-Si-O	-	108.97	-
Si-O-Si	-	109.47	-
H-Si-O	-	109.97	-
Si-O-Si-O	-	-	59.3
H-Si-O-Si	-	-	178.60

Table 5.1**:** Results from a B3LYP-DFT/6-311G** geometry optimization of H-POSS

Atom	q_i
Si	1.83
O	-1.15
H	0.105

Table 5.2: Partial charges for H-POSS derived from Mulliken population analysis

Results and Discussion

As discussed above, the energetic behavior of the particles along the heterogeneous axis of the DPPC bilayer has been calculated. A 1 ns MD simulation of an unperturbed hydrated DPPC bilayer was first performed to confirm that the simulated model bilayer is consistent with those used in earlier simulation studies [28]. In Figure 5.4 we present density profiles for pertinent atom groups in the unperturbed DPPC bilayer.

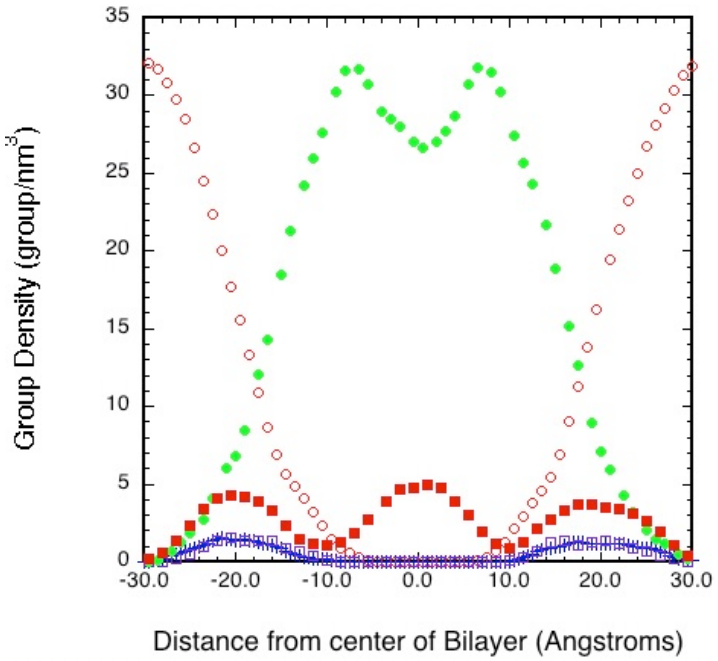

Figure 5.4: Atom group densities in an unperturbed DPPC bilayer: H_2O (○), CH_2 (●), CH_3 (■), phosphorus (□), and nitrogen (+)

We note that the density profiles closely resemble those of similar systems [29, 47, 48] for DPPC bilayers. Additionally, Figure 5.3 reflects the characteristics of each region as described in the four-region model. Namely, the system approaches that of pure water around 24Å away from the center of the bilayer, a significant presence of polar heads is observed between the depths of 16Å - 24Å and the system exhibits a relatively low aliphatic density in the center.

Study of C_{60} in DPPC

The $\Delta G(z)$ function for the C_{60} particle along the heterogeneous axis of the gel-phase DPPC bilayer, along with Gibbs free energies of transfer for C_{60} in liquid crystalline DPPC and DMPC systems are shown in Figure 5.5.

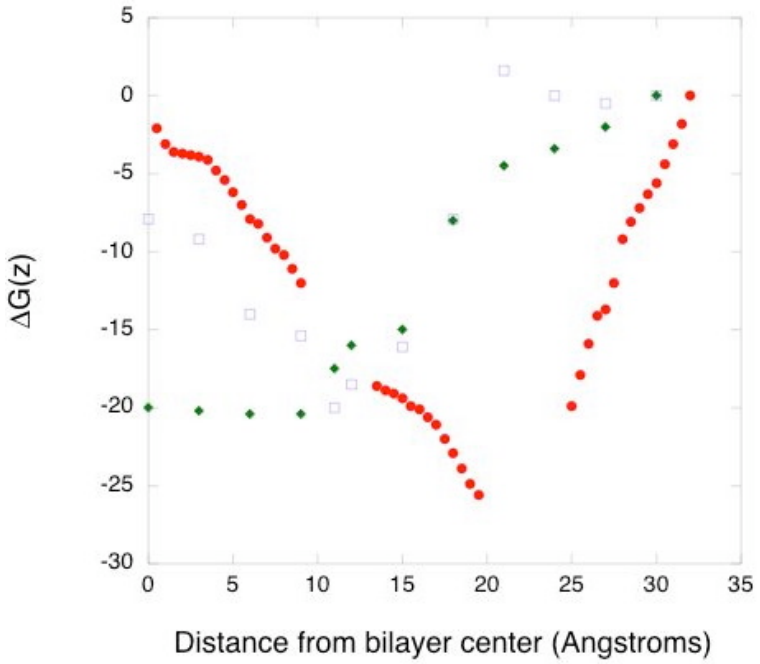

Figure 5.5: $\Delta G(z)$ of C_{60} in a gel-phase DPPC bilayer ●, a liquid crystalline DPPC bilayer □, and a liquid crystalline DMPC bilayer ◆

Figure 5.5 represents the change in Gibbs free energy associated with transferring the C_{60} particle from the water phase to another layer of the gel-phase DPPC system studied here,

along with liquid-crystalline DMPC and DPPC systems from other studies. The water phase was chosen as the reference therefore, region 1 corresponds to $\Delta G = 0$. For the gel-phase DPPC system, the transition from the water phase to the interfacial region results in a ΔG = -25.5 kcal/mol, which is the lowest energy state of the system. This value is significantly lower in comparison to the insertion of C_{60} into the interfacial region of a DMPC membrane at 310K shown by Bedrov, et. al [49]. However, the value of the energy minima for each system is similar, with a value of –21.8 kcal/mol in the DMPC study. The discrepancy in terms of the location of the minima in each system may be due to a variety of factors. It should be noted that the DMPC study is performed in the liquid crystalline temperature range, whereas this study is performed in the gel temperature range [50]. It is believed that this will have a significant effect on partitioning to the center of the bilayer, as the hydrophobic core in the gel phase will be significantly more rigid. The DMPC study was also sampled 10 nanoseconds, which is much longer than this study. However, the DMPC study uses a bilayer system that consists of only 52 lipid molecules, which may be too small to insert a particle as large as C_{60} without periodic effects. The transition of C_{60} to the highly ordered aliphatic region of the membrane from water is –12.1 kcal/mol, whereas the transition into the interior of the membrane is –2.1 kcal/mol. While this still indicates a favorable partitioning to the interior of the membrane, the degree of partitioning is greatly decreased from the liquid crystalline bilayer study. The relationship presented in Equation 5.2 indicates a moderate partitioning of C_{60} into a DPPC bilayer, with K(0) = 34. As with this study, most theoretical studies predict an energy minima that does not occur in the bilayer center [49, 51]. However, the depth of this minima is subject to debate, as the liquid crystalline

DMPC study only indicates a difference of about 1.8 kcal/mol from the minima to the center of the bilayer, where a very similar liquid crystalline study of DPPC [51] shows a difference of 12.4 kcal/mol, whereas the gel phase simulation in this study indicates a change of 23.4 kcal/mol.

These results seem to suggest that, for the gel phase of DPPC, C_{60} is energetically driven to the water/bilayer interfacial region. Alternatively, literature focused on liquid crystalline systems seems to suggest that C_{60} energetically prefers the zone between the high-density aliphatic carbon chain region and the decane region. The preference to the interfacial region for the gel phase study is reasonable, as the hydrocarbon region will be considerably more rigid, resulting in a greater energetic penalty when the particle is transferred to that region. Similar changes in partitioning behavior over the phase change from liquid crystalline to gel has been noted for smaller molecules, such as benzene, which exhibits a decrease in membrane/water partitioning by an order of magnitude [7, 8]. Therefore, given the relative size of C_{60}, the significant change in partitioning behavior is perhaps not so surprising

In an effort to better understand the migration of the C_{60} particle, a 1 ns simulation of a free floating C_{60} particle, initialized in the high-density-aliphatic region, was performed. Figure 5.6 shows the probability density of C_{60} occupying different depths in the vicinity of the interfacial region. The simulation indicates that C_{60} translates very minimally at the interface, with the particle predominantly occupying the region between 15Å – 19Å from the center of the bilayer.

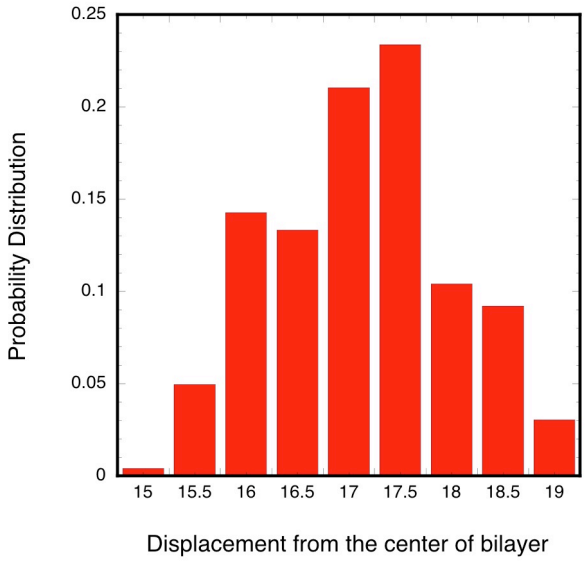

Figure 5.6: Probability of finding C_{60} at various depths about the interfacial region

This suggests that both the aliphatic region of the membrane and the bulk water region exert a significant amount of competing forces on the particle. Over the time range chosen, no explicit diffusive behavior is noted (i.e. the particle does not consistently trend towards either extreme), however, the probability distribution does indicate that C_{60} is most likely found about 17.5Å from the bilayer center. The particle will be largely segregated from the water at this depth and will be in contact with the highly-ordered alkane tail and polar head regions of the bilayer. The fact that C_{60} never fully enters the water phase again suggests that there is an energetic preference for the C_{60} to embed into the polar head rich region of the bilayer, as opposed to the water region.

Study of H-POSS in DPPC

The $\Delta G(z)$ function for the H-POSS particle along the heterogeneous axis of the DPPC bilayer is shown in Figure 5.7.

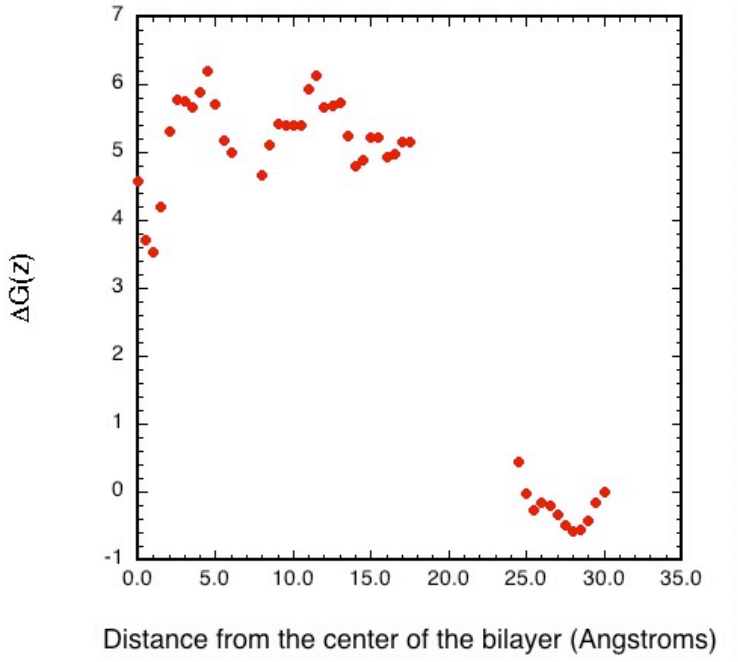

Figure 5.7: $\Delta G(z)$ of H-POSS in DPPC bilayer

Figure 5.7 shows that H-POSS energetically prefers the aqueous phase of the DPPC systems, with ΔG = -0.57 kcal/mol 28Å away from the bilayer center. The figure also shows an increase in $\Delta G(z)$ as the particle approaches the interface, as the $\Delta G(z)$ from bulk water to a depth of 24.5 Å is +0.45 kcal/mol. The partitioning of H-POSS into the hydrophobic region of the membrane is shown to be energetically unfavorable, with a transfer energy to the high-density aliphatic region of about +5 kcal/mol, whereas the core of the membrane shows a slightly less unfavorable transition energy of about +4 kcal/mol.

The favorable energy of H-POSS in water is likely due to the presence of partial atomic charges on the solute. Charges on the solute will lead to a stronger association with the polar water. These electrostatic interactions will be generally absent from the hydrophobic region, as the methyl groups in that region are relatively non-polar. The

small dips in energy seen at 28Å and at the bilayer center are likely the result of an overall lowered density in each region, as shown in Figure 5.4. The lower densities are attributed to the perturbation of the bulk water phase by the polar head groups of the DPPC molecules and the general loss of structure in the hydrocarbon chains as the center of the membrane is approached. The lowered density will provide a greater free volume available to the solute, which decreases the energetic penalty associated with creating the cavity for the particle.

A 1 ns, simulation with a free floating H-POSS in the DPPC membrane was also performed. The position of the H-POSS was initialized in the high density aliphatic regions, at a depth of about 13Å. In Figure 5.8 we present the probability density of H-POSS occupying various depths of the bilayer.

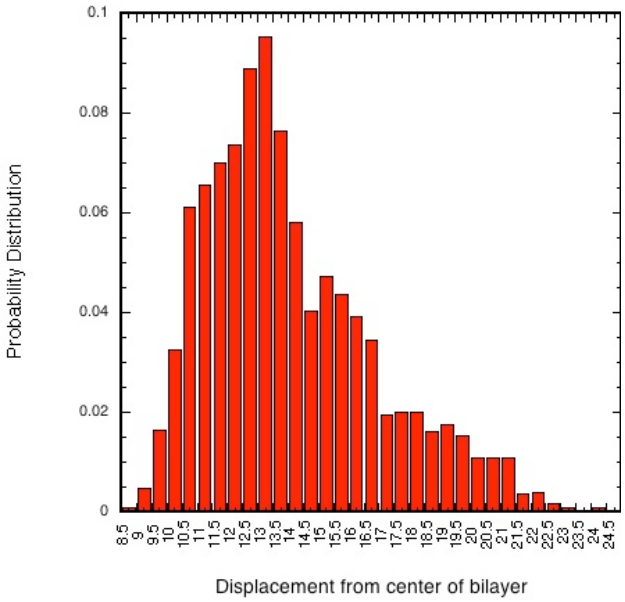

Figure 5.8: Probability of finding H-POSS at various depths in the DPPC membrane

The profile shows a maximum at 13Å, which is likely a result of the particle being initialized at this location. Given the high rigidity of the hydrophobic core, the H-POSS particle will likely spend a considerable amount of the 1 ns simulation near the depth at which it was initialized. The profile does show, however, that the probability of H-POSS occupying depths closer to the bilayer center drops off steeply, with a depth of 8.5Å being the closest to the center recorded. This observation agrees with Figure 5.7, which indicates that the insertion of H-POSS into the hydrophobic core is energetically unfavorable, making the occurrence of H-POSS in that region statistically improbable. The probability curve in Figure 5.8 does not decay very quickly as the H-POSS approaches the interfacial and perturbed water regions. Figure 5.8 shows an appreciable probability of finding H-POSS in the interfacial region between 16Å-24Å, with H-POSS being observed as far away from the center as 24.5Å. The fact that H-POSS is consistently found near the polar head region of the membrane, despite H-POSS being initialized far away from this region and the relatively short simulation time, supports the finding in Figure 5.7 that the perturbed water region of the DPPC system is the energetically favorable position for H-POSS.

Conclusions

The $\Delta G(z)$ function for C_{60} and H-POSS nanoparticles have been calculated using constraint dynamics molecular dynamics simulations. Additionally, free-floating simulations of both particles have been performed in an effort to clarify the partitioning behavior of the particles in interfacial regions. It was found that C_{60} partitions into the

organic phase of a hydrated DPPC system, particularly into the polar head region of the DPPC. The energetic preference of C_{60} to the interfacial region of the bilayer is likely a consequence of the extraordinary hydrophobicity of C_{60}. Furthermore, the gel phase of the DPPC membrane allows relatively little free volume available to the solute. Therefore, although the interior of the membrane is energetically favorable to the bulk water, the structure of the aliphatic chains of the gel phase DPPC are too rigid to allow partitioning from the interfacial region to the membrane interior.

The simulation results show that H-POSS is likely to partition into the aqueous phase of the DPPC/water system. Inserting the H-POSS into the aliphatic region of the DPPC membrane corresponds with a +5 kcal/mol penalty in the soft polymer region and a +4 kcal/mol penalty in the decane region. Like C_{60}, this penalty is likely due to the lack of free volume in the inner membrane to contain the H-POSS. Conversely, it was found that H-POSS is slightly energetically favorable in the perturbed water region of the system, with a ΔG = -0.57 kcal/mol. This is likely due to the increased free volume in the water due to the perturbation of the bulk water by the bilayer surface.

References

1. Yanganza, E.-S., Rioux, Danny, Simard, Marie, Arul, Joseph, and Tweddell, Russell J., *Ultrastructural Alterations of Erwinia carotovora subsp. atroseptica Caused by Treatment with Aluminum Chloride and Sodium Metabisulfate*. Applied and Environmenal Microbiology, 2004. **70**(11): p. 6800-6808.

2. Carranza-Rosales, P., Said-Fernandez, Salvador, Sepulveda-Saavedra, Julio, Cruz-Vega, Delia E., and Gandolfi, A. Jay, *Morphologic and functional altercations induced by low does of mercuric chloride in kidney OK cell line: ultrstructural evidence for an apoptotic mechanism of damage*. Toxicology, 2005. **210**(2-3): p. 111-121.

3. Levina, A., Harris, Hugh H., and Lay Peter A., *Binding of chromium(VI) to histones: implications for chromium(VI)-induced genotoxicity*. J Biol Inorg Chem, 2006. **11**(2): p. 225-234.

4. Devanathan, S., and Postle, Kathleen, *Studies on colicin B translocation: FepA is gated by TonB*. Molecular Microbiology, 2007. **65**(2): p. 441-453.

5. Cronin D., a.M.T., *The Role of Hydrophobicity in Toxicity Prediction*. Current Computer - Aided Drug Design. **2**(4): p. 405-413.

6. Lian, G., Chen, Longjian, and Han, Luijia, *An Evaluation of Mathematical Models for Predicting Skin Permeability*. Journal of Pharmaceutical Sciences, 2007. **91**(1): p. 584-598.

7. De Young, L.R., and Dill, Ken A., *Solute Partitioning into Lipid Bilayers*. Biochemistry, 1988. **27**(14): p. 5281-5289.

8. De Young, L.R., and Dill, Ken A., *Partitioning of Nonpolar Solutes into Bilayers and Amorphous n-Alkanes*. Journal of Physical Chemistry, 1989. **94**(2): p. 801-809.

9. Finizio, A., and Di Guardo, Antonio, *Estimating temperature dependence of solubility and octanol-water partion coefficient for organic compounds using RP-HPLC*. Chemosphere, 2001. **45**(6-7): p. 10630`070.

10. Mitragotri, S., Johnson, Mark E., Blankschtein, Daniel, and Langer, Robert, *An Analysis of the Size Selectivity of Solute Partitioning, Diffusion, and Permeation across Lipid Bilayers*. Biophysical Journal, 1999. **77**(1): p. 1268-1283.

11. Frankamp, B.L., et al., *Surface modification using cubic silsesquioxane ligands. Facile synthesis of water-soluble metal oxide nanoparticles*. Chemistry of Materials, 2006. **18**(4): p. 956-959.

12. Murakami, T. and K. Tsuchida, *Recent advances in inorganic nanoparticle-based drug delivery systems*. Mini-Reviews in Medicinal Chemistry, 2008. **8**(2): p. 175-183.

13. Da Ros, T., and Prato, Maurizio, *Medicinal chemistry with fullerenes and fullerene derivatives*. Chem. Commun., 1999: p. 663-669.

14. Tokuyama, H., Yamago, Shigeru, and Nakamura, Eiichi, *Photoinduced Biochemical Activity of Fullerene Carboxylic Acid*. J. Am. Chem. Soc., 1993. **115**(17): p. 7918-7919.

15. Fong, H., Dickens, Sabine H., and Flaim, Glenn M., *Evaluation of dental restorative composities containing polyhedral oligomeric silsesquioxane methacrylate*. Dental Materials, 2005. **21**: p. 520-529.

16. Kannan, R.Y., Salacinski, Henryk J., De Groot, Jaco, Clatworthy, Ian, Bozec, Laurent, Horton, Mike, Beutler, Peter E., and Seiffaliian, Alexander M., *The Antithrombic Potential of Polyhedral Oligomeric Silsesquioxane (POSS) Nanocomposite*. Biomacromolecules, 2006. **7**(1): p. 215-223.

17. Oberdorster, E., *Manufactured Nanmaterials (Fullerenes, C60) Induce Oxidative Stress in the Brain of Juvenile Largemouth Bass*. Environmental Health Perspectives, 2004. **112**(10): p. 1058-1062.

18. Zhao, X., Striolo, Alberto, and Cummings, Peter T., *C60 Binds to and Deforms Nucleotides*. Biophysical Journal, 2005. **89**(6): p. 3856-3862.

19. Redmill, P.S., Capps, Shannon C., Cummings, Peter T., and McCabe, Clare, *On the Calculation of the Gibbs Free Energy of Solvation for Fullerene Particles by Molecular Simulation*. Yet to be published, 2008.

20. McCusker, C., Carroll, Joseph B., and Rotello, Vincent M., *Cationic polyhedral oligomeric silsequioxane (POSS) units as carriers for drug delivery processes*. Chem. Commun., 2004: p. 996-998.

21. Marrink, S.J. and H.J.C. Berendsen, *Simulation of Water Transport through a Lipid-Membrane*. Journal of Physical Chemistry, 1994. **98**(15): p. 4155-4168.

22. Tieleman, D.P. and H.J.C. Berendsen, *Molecular dynamics simulations of a fully hydrated dipalmitoyl phosphatidylcholine bilayer with different macroscopic boundary conditions and parameters*. Journal of Chemical Physics, 1996. **105**(11): p. 4871-4880.

23. Egberts, E., S.J. Marrink, and H.J.C. Berendsen, *Molecular-Dynamics Simulation of a Phospholipid Membrane*. European Biophysics Journal with Biophysics Letters, 1994. **22**(6): p. 423-436.

24. Feller, S.E., et al., *Molecular dynamics simulation of unsaturated lipid bilayers at low hydration: Parameterization and comparison with diffraction studies*. Biophysical Journal, 1997. **73**(5): p. 2269-2279.

25. Smondyrev, A.M. and M.L. Berkowitz, *Structure of dipalmitoylphosphatidylcholine/cholesterol bilayer at low and high cholesterol concentrations: Molecular dynamics simulation*. Biophysical Journal, 1999. **77**(4): p. 2075-2089.

26. Tu, K.C., M.L. Klein, and D.J. Tobias, *Constant-pressure molecular dynamics investigation of cholesterol effects in a dipalmitoylphosphatidylcholine bilayer*. Biophysical Journal, 1998. **75**(5): p. 2147-2156.

27. Morrow, M.R., et al., *Comparison of DPPC and DPPG environments in pulmonary surfactant models*. Biophysical Journal, 2007. **93**(1): p. 164-175.

28. Bemporad, D., Luttmann, C., and Essex, J.W., *Behaviour of small solutes and large drugs in a lipid bilayer from computer simulations*. Biochemica et Biophysica Acta, 2005. **1718**: p. 1-21.

29. Tieleman, D.P., Marrink, S.J., and Berendsen, H.J.C., *A computer perspective of membranes: molecular dynamics studies of lipid bilayer systems*. Biochemica et Biophysica Acta, 1997. **1331**: p. 235-270.

30. Marrink, S.-J., and Berendsen, Herman J.C., *Simulation of water transport through a lipid bilayer*. J. Phys. Chem., 1994. **98**(15): p. 4155-4168.

31. Kubo, R., *The fluctuation-dissipation theorem*, Department of Physics, University of Tokyo, Japan. p. 255-284.

32. Chan, E.R., Striolo, Alberto, McCabe, Clare, Cummings, Peter T., and Glotzer, Sharon C., *Coarse-grained force field for simulating polymer-tethered silsesquioxane self-assembly in solution*. J. Chem. Phys., 2007. **127**(11): p. 114102(1-15).

33. Ionescu, T., Qi, Feng, McCabe, Clare, Striolo, Alberto, Kieffer, John, and Cummings, Peter T., *Evaluation of Force Fields for Molecular Simulation of Polyhedral Oligomeric Silsesquioxanes*. J. Phys. Chem. B., 2006. **110**(6): p. 2502-2510.

34. Li, H.-C., Lee, Ching-Ying, McCabe, Clare, Striolo, Alberto, and Neurock, Matthew, *Ab initio analysis of the structural properties of alkyl-substituted polyhedral oligomeric silsesquioxanes*. Journal of Physical Chemistry A, 2007. **111**(18): p. 3577-3584.

35. Lu, X., and Chen, Zhongfang, *Curved Pi-Conjugation, Aromaticity, and the Related Chemistry of Small Fullerenes (<C60) and Single-Walled Carbon Nanotubes*. Chemical Reviews, 2005. **105**(10): p. 3643-3696.

36. Kroto, H.W., *The stability of the fullerenes Cn, with n = 24, 28, 32, 50, 60, and 70*. Nature, 1987. **329**(8): p. 529-531.

37. Plimpton, S., *Fast Parallel Algorithms for Short-Ranged Molecular Dynamics*. Journal of Computational Physics, 1995. **117**: p. 1-19.

38. Berendsen, H.J.C. and B. Egberts, *Molecular Dynamics of a Bilayer Membrane with Atomic Detail*. Ehrenberg, A., Et Al. (Ed.). Springer Series in Biophysics, Vol. 1. Structure, Dynamics and Function of Biomolecules; First Ebsa (European

Biophysical Societies Association) Workshop, Saltsjobaden, Sweden, July 6-10, 1986. Xvi+302p. Springer-Verlag New York, Inc.: Secaucus, New Jersey, USA; Springer-Verlag: Berlin, West Germany. Illus, 1987: p. 275-280.

39. Feller, S.E. and R.W. Pastor, *On simulating lipid bilayers with an applied surface tension: Periodic boundary conditions and undulations*. Biophysical Journal, 1996. **71**(3): p. 1350-1355.

40. Jahnig, F., *What is the surface tension of a lipid bilayer membrane?* Biophysical Journal, 1996. **71**(3): p. 1348-1349.

41. Chiu, S.W., et al., *Incorporation of Surface-Tension into Molecular-Dynamics Simulation of an Interface - a Fluid-Phase Lipid Bilayer-Membrane*. Biophysical Journal, 1995. **69**(4): p. 1230-1245.

42. Feller, S.E., MacKerell, Alex. D. Jr., *An Improved Empiracal Potential Energy Function for Molecular Simulations of Phospholipids*. Journal of Physical Chemistry B, 2000. **104**(31): p. 7510-7515.

43. Jorgensen, W.L., Chandrasekhar, Jayaraman, Madura, Jeffrey D., Impey, Roger W., and Klein, Michael L., *Comparison of simple potential functions for simulating liquid water*. Journal of Physical Chemistry, 1983. **79**(2): p. 926-935.

44. Cruz-Chu, E., Aksimentiev, Aleski, and Schulten, Klaus, *Water-Silica Force Field of Simulating Nanodevices*. Journal of Physical Chemistry B, 2006. **110**(43): p. 21497-21508.

45. de Gennes, P.-G., Brochard-Wyatt, François, and Quéré, David, *Capillarity and Wetting Phenomena: Drops, Bubbles, Pearls, Waves*. 2002, New York: Springer.

46. Straatsma, T.P.A., E., Windus, T.L., Bylaska, E.J., de Jong, W., Hirata, S., Valiev, M., Hackler, M., Pollack, L., Harrison, R., Dupuis, M., Smith, D.M.A, Nieplocha, J., Tipparaju V., Krishnan, M., Auer, A.A., Brown, E., Cisneros, G., Fann, G., Früchtl, H., Garza, J., Hirao, K., Kendall, R., Nichols, J., Tsemekhman, K., Wolinski, K., Anchell, J., Bernholdt, D., Borowski, P., Clark, T., Clerc, D., Dachsel, H., Deegan, M., Dyall, K., Elwood, D., Glendening, E., Gutowski, M., Hess, A., Jaffe, J., Johnson, B., Ju, J., Kobayashi, R., Kutteh, R., Lin, Z.; Littlefield, R.; Long, X., Meng, B., Nakajima, T., Niu, S., Rosing, M., Sandrone, G., Stave, M., Taylor, H., Thomas, G., van Lenthe, J., Wong, A., and Zhang, Z., *NWChem, A Computational Chemistry Package for Parallel Computers*. 2004, Pacific Northwest National Laboratory: Richland, Washington.

47. Falck, E., Patra, Michael, Karttunen, Mikki, Hyvonen, Marja T., and Vattulainen, *Lessons of Slicing Membranes: Interplayy of Packing, Free Area, and Lateral Diffusion in Phospholipid/Cholesterol Bilayers*. Biophysical Journal, 2004. **87**(2): p. 1076-1091.

48. Leekumjorn, S., and Sum, Amadeu K., *Molecular Simulation Study of Structural and Dynamic Properties of Mixed DPPC/DPPE Bilayers*. Biophysical Journal, 2006. **90**(11): p. 3951-3965.

49. Bedrov, D., Smith, Grant D., Davande, Hemali, and Li, Liwei, *Passive Transport of C60 Fullerenes through a Lipid Membrane: A Molecular Dynamics Simulation Study*. J. Phys. Chem. B., 2007. **112**(7): p. 2078-2084.

50. Trahms, L., Klabe, Wolf D., and Boroske, Edwin, *H-NMR Study of the Three Low Temperature Phases of DPPC-Water Systems*. Biophysical Journal, 1983. **42**: p. 285-293.

51. Qiao, R., Roberts, Aaron P., Mount, Andrew S., Klaine, Stephen J., and Ke, Pu Chun, *Translocation of C60 and Its Derivatives Across a Lipid Bilayer*. Nano Letters, 2007. **7**(3): p. 614-619.

CHAPTER VI

CONCLUSION AND FUTURE WORK

Conclusions

The work presented in this dissertation demonstrates the feasibility of predicting of aqueous/organic partitioning data for various nanoscale building blocks (NBBs). Using molecular dynamics simulations and thermodynamic integration, it has been shown that bare fullerene materials exhibit significant hydrophobicity and organophilicity, implying that such particles partition readily into the organic phase of aqueous/organic systems. It was found that the size and shape of fullerene particles has a direct effect on hydrophobicity. Generally speaking, larger fullerene particles exhibit a higher ΔG^{solv} than their smaller counterparts. Also, the surface wettability of fullerenes has a profound effect on hydrophobicity, as open nanotubes that allow water into the interior of the tube are found to be significantly more hydrophobic than capped nanotubes, which do not allow water into the interior of the tube.

The group-contribution method, UNIFAC, was applied to systems of infinitely dilute C_{60} in water and octanol. While the values of $\gamma^{\infty}_{C_{60}}$ in a given solvent appear to be artificially high due to large negative solute-solute energies which appear in the calculation, the ratio of the activity coefficients in water and octanol provides a reasonable first approximation of $\log K_{O/W}$ for NBBs. A *b initio* supermolecule calculations were then performed to generate binary interaction parameters for H-POSS for the use in UNIFAC $logK_{O/W}$ calculations. The UNIFAC approach was further tested

by showing that the method correctly predicted the hydrophilic shift, reflected in TI studies, for a C_{60} decorated with 32 -OH groups, and H-POSS functionalized with fluorine and OH.

Finally, the partitioning of H-POSS and C_{60} in a heterogenous DPPC bilayer was evaluated using a potential of mean force calculation. These studies show that a C_{60} will readily partition into the center of the bilayer from the bulk water phase. The H-POSS particle, on the other hand, experiences a significant barrier at the DPPC/water interface, implying that H-POSS may ultimately remain in the water phase.

This work is a step towards of understanding the partitioning behavior of some basic NBBs in aqueous/organic systems. The techniques described here will hopefully inspire measurements of solubility data for NBB variants as well as additional theoretical studies. The ultimate goal is to be able to calculate solubility data for any particle, in any solution, at various degrees of accuracy depending on the desired expense of the calculation. Despite these gains, there are many phenomena of nanoparticle phase equilibria not explored in this work, that will likely prove beneficial to this goal. Below are recommendations of future studies on this subject.

Future Work

CHARMM parameterization for fullerene materials

Given the lack of potentials available for fullerene materials, particularly for functionalized varieties, and the uncertainty associated with which solvent force fields can be used with established fullerene potentials; a standardized fullerene potential for a common force field. Given its wide usage and well-documented parameterization

methodology, the CHARMM force field seems ideal for this endeavor. Ideally, the force field would be as general as possible, with the ability to model pristine and functionalized fullerenes, in a variety of solvents. Given the ambitious nature of such an endeavor, this is a goal that would likely take the contribution of several students.

Fortunately, gas phase conformations of many fullerenes, such as bare C_{60}, bare carbon nanotubes, and the hydroxylated C_{60} from this work, are readily available. The CHARMM parameterization[1] cites *ab initio* vibrational spectra as a means of fitting intramolecular force constraints, such as the bonded, angular, torsional, improper, and Urey-Bradley interactions. As per the CHARMM parameterization methodology, the HF level of theory with a 6-31G(d) basis set is to be used for vibrational spectra calculations. Vibrational spectra are common output from *ab initio* codes, and many packages, such as NWCHEM, have built in features that easily allow this computation.

For the calculation of intermolecular interactions, the partial charges of the solute atoms are determined via supermolecule calculations involving the solute and a TIP3P water molecule. In the calculations, the partial charges of the water molecule are held fixed to the TIP3P parameters, whereas the charges of the solute atoms that are interacting directly with the water molecule are parameterized using a Mulliken population analysis. The remainder of the non-BSSE interaction energy at the HF/6-31G(d) basis set energy is initially attributed to van der Waals interactions. The initial well depth of the interaction is taken as the remainder of the energy scaled by a factor of 1.16, whereas the interaction minimum radius is assumed to be 0.20Å smaller than the *ab initio* radius. The empirical scaling of ε and σ are due to the HF level of theory being unable to account appreciably for dispersion effects. Subsequently, the dispersion

interactions are optimized in a fashion, designed to reproduce experimental condensed phase properties, such as density, from an MD simulation.

UNIFAC parameterization of bare NBB units

The work presented here shows that UNIFAC is a sufficient tool for an inexpensive estimation of $\log K_{O/W}$ of fullerene systems, yet falls short of being able to predict γ in a given solvent. Ideally, it is desired that not only UNIFAC be able to more accurately estimate $\log K_{O/W}$ values, but also predict activity coefficients in a single solvent. There is a substantial body of work that compiles the solubility of fullerenes in various organic solvents[2, 3], therefore, binary interaction parameters for C_{60} in organic solvents can be optimized relative to existing phase data. Obviously, the calculation of aqueous/organic partitioning coefficients is contingent upon fullerene/water equilibria data, which is scarce. However, the solid-equilibria calculations via the density-of states/MC technique, in conjunction with accounting for aggregation effects of the fullerene solutes, would allow for the formal parameterization of fullerene/water binary interaction parameters.

References

1. MacKerell, A.D., Bashford, D., Bellott, M., Dunbrack, R.L., Evanseck, J.D., Field, M.J., Fischer, S., Gao, J., Guo, H., Ha, S., Joseph-McCarthy, D., Kuchnir, L., Kuczera, K., Lau, F.T.K., Mattos, C., Michnick, S., Ngo, T., Nguyen, D.T., Prodhom, B., Reiher, W.E., Roux, B., Schlenkrich, M., Smith, J.C., Stote, R., Straub, J., Watanabe, M., Wiorkiewicz-Kuczera, J., Yin, D., and Karplus, M., *All-Atom Empiracle Potential for Molecular Modeling and Dynamics Studies of Proteins.* J. Phys. Chem. B., 1998. **102**(18): p. 3586-3616.

2. Hansen, C.M., and Smith, Allan L., *Using Hansen solubility parameters to correlate solubility of C60 fullerene in organic solvents and in polymers.* Carbon, 2004. **42**(8-9): p. 1591-1597.

3. Marcus, Y., Smith, Allan, L., Korobov, M.V., Mirakyan, A.L., Avramenk, N.V., and Stukalin, E.B., *Solubility of C60 Fullerene.* J. Phys. Chem. B., 2001. **105**(13): p. 2499-2506.

APPENDIX A

ELECTRONIC STRUCTURE CALCULATIONS

This appendix is largely adapted from Hehre, W.J, et al[1], which offers a more thorough of treatment of sections 1, 2a, 2c, and 3a.

General Formulism

Electronic structure calculations are valuable in cases where energetic or structural attributes need to be defined. The Hamiltonian operator, shown below, describes the energy of a molecule

$$\hat{H}\Psi = E\Psi \tag{A.1}$$

where

$$\hat{H} = -\frac{1}{2}\sum_{i}^{E}\left(\frac{\partial^2}{\partial_{x_i}^2}+\frac{\partial^2}{\partial_{y_i}^2}+\frac{\partial^2}{\partial_{z_i}^2}\right)-\sum_{i}^{elec}\sum_{s}^{nuclei}\frac{Z_s}{r_{is}}+\sum_{i}^{elec}\sum_{j=i+1}^{elec}\frac{1}{r_{ij}}+\sum_{s}^{nuclei}\sum_{t=s+1}^{nuclei}\frac{Z_s Z_t}{R_{st}} \tag{A.2}$$

and Ψ is the many electron wavefunction and E is the energy eigenvalue resulting from the operation. Each term in the Hamiltonian represents an energetic contribution to the system. Namely, the first term the kinetic energy of the electrons, the second term is the Coulombic potential between electrons and nuclei, the third is the repulsive term between electrons, and the final term is the Coulombic potential between nuclei. The wavefunction is an abstract concept, and is commonly related to the probability of finding an electron within a given 3-dimensional space

$$\rho(dV_1, dV_2, \ldots dV_n) = \int\int\ldots\int \Psi^{*}\Psi dV_1 dV_2 \ldots dV_n \tag{A.3}$$

where, if integrated over all space, will return a normalization constant of 1.

$$\rho(dV_1, dV_2, \ldots dV_n) = \int_{-\infty}^{\infty}\int_{-\infty}^{\infty}\ldots\int_{-\infty}^{\infty} \Psi^{*}\Psi dV_1 dV_2 \ldots dV_n = 1 \qquad \text{(A.4)}$$

Given a perfect wavefunction, equation 1 will calculate the exact system energy. Unfortunately, exact wavefunctions only exist for the simplest systems; therefore, a large aspect of electronic structure calculations is the optimization of a many-electron wavefunction that effectively describes the system.

The many electron wavefunction can be constructed by using so-called molecular orbital wavefunctions (ψ_i), which in turn, are defined by a basis function (ϕ_i) of predefined form. The molecular orbital is defined as

$$\psi_i = \sum_{\mu=1}^{N} c_{\mu i}\phi_{\mu} \qquad \text{(A.5)}$$

where *N* is the number of one-electron basis functions and $c_{\mu i}$ is a constant to be varied in order to achieve the minimization of E. Below are the forms of common Gaussian-type basis functions[2]

$$g_s(\alpha,r)=\left(\frac{2\alpha}{\pi}\right)^{3/4}e^{-\alpha r^2}$$

$$g_x(\alpha,r)=\left(\frac{128\alpha^5}{\pi^3}\right)^{1/4}xe^{-\alpha r^2}$$

$$g_y(\alpha,r)=\left(\frac{128\alpha^5}{\pi^3}\right)^{1/4}ye^{-\alpha r^2}$$

$$g_z(\alpha,r)=\left(\frac{128\alpha^5}{\pi^3}\right)^{1/4}ze^{-\alpha r^2}$$

$$g_{xx}(\alpha,r)=\left(\frac{2048\alpha^7}{9\pi^3}\right)^{1/4}x^2e^{-\alpha r^2}$$

$$g_{yy}(\alpha,r)=\left(\frac{2048\alpha^7}{9\pi^3}\right)^{1/4}y^2e^{-\alpha r^2} \qquad \text{(A.6)}$$

$$g_{zz}(\alpha,r)=\left(\frac{2048\alpha^7}{9\pi^3}\right)^{1/4}z^2e^{-\alpha r^2}$$

$$g_{xy}(\alpha,r)=\left(\frac{2048\alpha^7}{9\pi^3}\right)^{1/4}xye^{-\alpha r^2}$$

$$g_{xz}(\alpha,r)=\left(\frac{2048\alpha^7}{9\pi^3}\right)^{1/4}xze^{-\alpha r^2}$$

$$g_{yz}(\alpha,r)=\left(\frac{2048\alpha^7}{9\pi^3}\right)^{1/4}yze^{-\alpha r^2}$$

where the function g_s has the s–type atomic orbital symmetry and g_x, g_y and g_z have the p-type atomic orbital symmetry. A combination of these orbitals yields two additional d-type atomic orbitals

$$g_{3zz-rr} = \frac{1}{2}\left(2g_{zz} - g_{xx} - g_{yy}\right)$$

$$g_{xx-yy} = \left(\frac{3}{4}\right)^{1/2}\left(g_{xx} - g_{yy}\right)$$

and an additional s-type atomic orbital.

$$g_{rr} = 5^{-1/2}\left(g_{xx} + g_{yy} + g_{zz}\right)$$

Assuming each electron can have an "up" (α) or "down" (β) spin, where the spin wavefunctions take the form

$$\begin{aligned} \alpha\left(+\frac{1}{2}\right) &= 1; \alpha\left(-\frac{1}{2}\right) = 0 \\ \beta\left(+\frac{1}{2}\right) &= 0; \beta\left(-\frac{1}{2}\right) = 1 \end{aligned} \tag{A.7}$$

where the argument is the spin number of the electron in question. The complete wavefunction, or spin orbital, for an electron is the product of the molecular orbital and the spin function

$$\begin{aligned} \chi(x,y,z,\xi) &= \psi(x,y,z)\alpha(\xi) \\ \chi(x,y,z,\xi) &= \psi(x,y,z)\beta(\xi) \end{aligned} \tag{A.8}$$

Many-body electron wavefunctions must exhibit the property of antisymmetry, in which the exchange of electrons produces the original wavefunction, multiplied by -1.

$$\Psi(i\cdots j\cdots n) = -\Psi(j\cdots i\cdots n) \tag{A.9}$$

While a product of all the spin orbitals does result in a simple representation of a many electron wavefunction, it does not necessarily have the required property of antisymmetry.

$$\Psi_{product} = \chi(1)\chi(2)\cdots\chi(n) \neq (-1)\chi(2)\chi(1)\cdots\chi(n) \tag{A.10}$$

Therefore, in order to ensure antisymmetry, the spin orbitals are arranged in a determinantal wave function

$$\Psi_{determinant} = \begin{vmatrix} \chi_1(1) & \chi_2(1) & \cdots & \chi_n(1) \\ \chi_1(2) & \chi_2(2) & \cdots & \chi_n(2) \\ & & \vdots & \\ \chi_1(n) & \chi_2(n) & \cdots & \chi_n(n) \end{vmatrix} \tag{A.11}$$

where the elements of the 1st row of the determinant contain the assignations of election 1 to all of the spin orbitals calculated in equation 8. Exchanging electrons i and j is the equivalent of exchanging rows i and j in the determinant, which by definition, changes the sign of the determinant. With a closed-shell (i.e. all orbitals doubly occupied), equation 10 can be written in the form of the *Slater determinant*[3]

$$\Psi = (n!)^{-\frac{1}{2}} \begin{vmatrix} \psi_1(1)\alpha(1) & \psi_1(1)\beta(1) & \psi_2(1)\alpha(1) & \cdots & \psi_{n/2}(1)\beta(1) \\ \psi_1(2)\alpha(2) & \psi_1(2)\beta(2) & \psi_2(2)\alpha(2) & \cdots & \psi_{n/2}(2)\beta(2) \\ & & & \vdots & \\ \psi_1(n)\alpha(n) & \psi_1(n)\beta(n) & \psi_2(n)\alpha(n) & \cdots & \psi_{n/2}(n)\beta(n) \end{vmatrix} \tag{A.12}$$

where $(n!)^{-1/2}$ is the normalization constant where n is the number of electrons in the system. As all orbitals doubly occupied, there are, of course, *n/2* molecular orbitals.

Levels of Theory

Hartree-Fock

A so-called full electron configuration energy can be built upon the many electron wavefunction, determinantal wavefunction using a linear combination of determinantal wavefunctions

$$\Psi = a_o \Psi_o + \sum_{s>0} a_s \Psi_s \qquad \text{(A.13)}$$

where Ψ_s denotes a many body electron wavefunction that puts electrons in promoted electronic energy states. The further equation 13 is extended, the more accurate the value of E becomes, which, of course, corresponds with a substantial computational costs.

Truncating equation 13 at the 0^{th} term is known as the *Hartree-Fock* (HF) level of theory. While this level of theory has recently been largely abandoned in favor of higher levels of theory, such as DFT or MP2, HF can often predict accurate molecular structures and reaction energies. Furthermore, the optimization of the HF system provides a template for many higher-level theories.

Given the imperfect nature of the HF many electron wavefunction, the energy calculated follows the strict rule

$$E' = \int \Phi^* \hat{H} \Phi dV < E \qquad \text{(A.14)}$$

where Φ is the HF many electron wavefunction, E' is the HF energy, and E is the actual system energy. Equation 14 once again indicates that any non-perfect wavefunction will produce energy higher than the actual energy; therefore, all calculations provide an upper bound to the actual energy.

The Roothaan-Hall equations[4, 5], shown below, are used to optimize the coefficients of the closed-shell HF formulation

$$\sum_{\nu}^{N}\left(F_{\mu\nu}-\varepsilon_i S_{\mu\nu}\right)c_{\nu i}=0 \tag{A.15}$$

$$\sum_{\mu=1}^{N}\sum_{\nu=1}^{N}c_{\mu i}S_{\mu\nu}c_{\nu i}=1 \tag{A.16}$$

where N is the number of basis functions in a molecular orbital, ε_i is the one-electron orbital in molecular orbital ψ_i , $S_{\mu\nu}$ are elements of a NxN matrix termed the overlap matrix

$$S_{\mu\nu}=\int \phi_\mu^*(1)\phi_\nu dV_1 \tag{A.17}$$

and $F_{\mu\nu}$ is an element in another NxN matrix, called the Fock matrix.

$$F_{\mu\nu}=H_{\mu\nu}^{core}+\sum_{\lambda=1}^{N}\sum_{\sigma=1}^{N}P_{\lambda\sigma}\left[(\mu\nu\,|\,\lambda\sigma)-\frac{1}{2}(\mu\lambda\,|\,\nu\sigma)\right] \tag{A.18}$$

The 1st in the Fock matrix represent the one-electron energy in a field of "bare" nuclei, which takes the following form

$$H_{\mu\nu}^{core}=\int \phi_\mu^*(1)\hat{H}_{core}(1)\phi_\nu(1)dV_1 \tag{A.19}$$

$$\hat{H}_{\mu\nu}^{core}(1)=-\frac{1}{2}\left(\frac{\partial^2}{\partial_{x_1}^2}+\frac{\partial^2}{\partial_{y_1}^2}+\frac{\partial^2}{\partial_{z_1}^2}\right)-\sum_{A=1}^{M}\frac{Z_A}{r_{1A}} \tag{A.20}$$

where Z_A is the atomic number of atom A. The 2nd term, $P_{\lambda\sigma}$ is the one-electron density matrix

$$P_{\lambda\sigma}=2\sum_{i=1}^{occ}c_{\lambda i}^{*}c_{\sigma i} \tag{A.21}$$

which is summed over only the occupied orbitals. The leading factor of 2 indicates that there are 2 electrons per orbital. The final terms are the so-called two-electron repulsion integrals.

$$(\mu\nu \mid \lambda\sigma) = \int\int \phi_\mu^*(1)\phi_\nu(1)\left(\frac{1}{r_{12}}\right)\phi_\lambda^*(2)\phi_\sigma(2)dV_1dV_2 \tag{A.22}$$

The total system energy can now be expressed in terms of the electronic energy, E^{ee}, and the internuclear repulsion, E^{nr}.

$$E^{ee} = \frac{1}{2}\sum_{\mu=1}^{N}\sum_{\nu=1}^{N} P_{\mu\nu}\left(F_{\mu\nu} + H_{\mu\nu}^{core}\right) \tag{A.23}$$

$$E^{nr} = \sum_{A}^{N}\sum_{B=A+1}^{N}\frac{Z_A Z_B}{R_{AB}} \tag{A.24}$$

Obviously, the Roothaan-Hall equations are non-linear, therefore, and iterative scheme must be invoked for their solution. Commonly used iterative schemes in *ab initio* software are the Jacobi-Davidson[6] and Newton-Raphson[7] methods.

Density Functional Theory

This section has been largely adapted largely from Argaman, N. et al[8], where a more rigorous treatment of the subject material may be found.

Density Functional Theory (DFT) is an extension to the simple HF theory, which, while maintaining the same low computational expense, computes some molecular attributes such as vibrational frequencies and IR spectra of closed-shell molecules, more accurately. This is due to the inclusion of an empirical function that accounts for exchange and correlation effects.

The basis of DFT is the Kohn-Sham equation[9], which can be applied as an alternative form of the standard Hamiltonian

$$E = -\frac{1}{2}\sum_{i=1}^{n}\int \psi_i(\mathbf{r})\nabla^2\psi_i(\mathbf{r})d\mathbf{r} + \sum_{A=1}^{M}\int \frac{Z_A}{|\mathbf{R_A}-\mathbf{r}|}\rho(\mathbf{r})d\mathbf{r} + \frac{1}{2}\int \frac{\rho(\mathbf{r})\rho(\mathbf{r}')}{|\mathbf{r}-\mathbf{r}'|}d\mathbf{r}d\mathbf{r} + E_{XC} \quad \text{(A.25)}$$

where the 1st term is the kinetic energy of n non-interacting particles, the 2nd term is the energy due to the electron-nuclei attraction, the 3rd term is the electron-electron repulsion term, and the 4th term is the exchange-correlation (XC) term. The electron density, $\rho(\mathbf{r})$, can be expressed in terms of the single-electron wavefunction, ψ_i, in the following fashion.

$$\rho(\mathbf{r}) = \sum_{i=1}^{n}|\psi_i(\mathbf{r})|^2 \quad \text{(A.26)}$$

The main difference between DFT and *ab initio* methods is the usage of a simple, 3-dimensional density function describing *n* non-interacting electrons in an effective field in DFT, versus the cumbersome 3N-dimensional many-electron wavefunction used in ab intio methods. Density functional theory also adds an empirical function to describe the exchange and correlation effects on a molecular system, an attribute that the HF level lacks. Therefore, if the E_{xc} term in equation 25 is omitted, the HF result is obtained. Furthermore, the E_{xc} term adds little computational expense over HF, as both scale on the order of N^4.

The exchange energy represents the energy associated with swapping the spatial coordinates of two exclusive electrons. Whereas the correlation energy corresponds to energy that results from the perturbations of electron cloud $\rho(\mathbf{r}')$ due to interactions with a changing position of $\rho(\mathbf{r})$. Many empirical XC functionals are

available, and the subject remains an active area of research in quantum chemistry calculations. The simplest XC functional is the Local Density Approximation (LDA), as suggested by Kohn and Sham

$$E_{xc}[\rho(\mathbf{r})] = \int \varepsilon_{xc}(\rho(\mathbf{r}))\rho(\mathbf{r})d\mathbf{r} \tag{A.27}$$

where $\varepsilon_{xc}(\rho(\mathbf{r}))$ is the exchange-correlation energy per particle of a uniform interacting gas, which as been measured to great accuracy with literature.

Møller-Plesset Perturbation Theory

The closed-shell, single-determinant many electron wavefunction used in the Hartree-Fock level of theory has many qualitative deficiencies due to its lack of correlation between electrons. Primarily, HF and DFT methods fail to reproduce accurate dispersion interactions between two particles.

The Møller-Plesset perturbation theory (MPn)[10] accounts, in part, for this deficiency by taking the extended form of equation 13, which has multiple secular determinants based upon the ground and excited states of the molecule.

The generalized operator, $\hat{H}_\lambda$, defines Møllet-Plesset models,

$$\hat{H}_\lambda = \hat{H}_0 + \lambda\hat{V} \tag{A.28}$$

where $\hat{H}_o$ is the sum of the one-electron Fock operators (which produces the Fock matrix, in equation 18) and $\hat{V}_o$ is the system perturbation, defined as

$$\lambda\hat{V} = \lambda\left(\hat{H} - \hat{H}_o\right) \tag{A.29}$$

with λ being a dimensionless parameter and $\hat{H}$ being the Hamiltonian. Accordingly, the many-electron wavefunction and energy take the following form

$$\Psi_\lambda = \Psi^o + \lambda\Psi^{(1)} + \lambda^2\Psi^{(2)}\ldots \tag{A.30}$$

$$E_\lambda = E^{(o)} + \lambda E^{(1)} + \lambda^2 E^{(2)} \cdots \tag{A.31}$$

where the 0th term is simply the HF level of theory. Furthermore, the singly excited state term (1st term) give a mathematically trivial addition to the HF level of theory, so the wavefunction is never expressed as simply two terms. Truncation at the 2nd order term is referred to as the MP2 level of theory, with is a widely used post-HF electronic structure method. Truncation after later terms is denoted as MP3, MP4, etc., however, these methods are used much more rarely, as they represent a great computational expense.

Electronic Structure Parameterization Techniques

Mulliken Population Analysis

First-principles techniques offer the unique opportunity to parameterize force-field potentials for molecular systems that have experimentally unknown properties. Long-range electrostatic potentials are crucial for the accurate modeling of many systems within a MD context. Fortunately, the resulting molecular orbitals from electronic structure calculations can be utilized by several different techniques, to produce atomistic point charges; which demand little additional computational expense.

One such technique is known as the Mulliken population analysis[11]. This technique assigns a distinct point charge to an atomistic position by integrating the electron density over space, as in equation 26, and allocating electron populations to the atoms and bonds of the molecule. Integration over the electron density yields

$$\int \rho(r) dr = \sum_{\mu}^{N} \sum_{\nu}^{N} P_{\mu\nu} S_{\mu\nu} = n \tag{A.32}$$

where $P_{\mu\nu}$ is the one-electron density matrix described in equation 21 and $S_{\mu\nu}$ is the overlap matrix, which describes the inter-relationship between basis functions μ and ν. Accordingly, the electron population of orbital volumes occupied by both basis functions μ and ν is as follows

$$Q_{\mu\nu} = 2P_{\mu\nu}S_{\mu\nu} \quad (\mu \neq \nu) \tag{A.33}$$

where the coefficient of 2 reflects that there are two electrons in each orbital. Furthermore, the electronic population of a basis function can be estimated by adding the one-electron density and half of the overlap density, summed over all other basis functions, shown below.

$$q_\mu = P_{\mu\mu} + \sum_{\mu \neq \nu} P_{\mu\mu}P_{\mu\nu} \tag{A.34}$$

In order to find the Mulliken population about atom A, the electron populations of orbitals centered about atom *A* are summed.

$$q_A = \sum_{\mu}^{A} q_\mu \tag{A.35}$$

Counterpoise Correction[12]

Commonly, it is desired to obtain intermolecular interactions between two molecules from ab intio calculations. However, errors arise due to the fact that many molecular orbitals on one molecule overlap with oribitals on the opposing molecule. This is called the basis set superposition error. The interaction energy of a cluster of particles *A* and *B* is simply the following expression

$$\Delta E_{A \cdot B} = E_{A \cdot B} - (E_A + E_B) \tag{A.36}$$

where $\Delta E_{A\cdot B}$ is the interaction energy, $E_{A\cdot B}$ is the energy of cluster A and B, and E_A and E_B are the energies of molecules A and B in vacuo.

Orbitals from molecule A will overlap with orbitals on molecule B, and vice versa. As a result, ab initio calculations will optimize the coefficients in orbitals from molecule A to refine orbitals in molecule B, and likewise from B to A. This results in an artificially low energetic state for the individual molecules and can lead to dramatically overestimated interaction energies.

One projected solution to this problem is the counterpoise correction, where the interaction energy is expressed with an additionally calculated correction.

$$E_{A\cdot B}^{CP} = E_{A\cdot B} + CP \tag{A.37}$$

$$CP = \left(E_A - E_A^*\right) + \left(E_B - E_B^*\right) \tag{A.38}$$

where E_A^* and E_B^* are the energies for individual molecules A and B calculated using all of the basis functions used in the $A\cdot B$ cluster energy calculation, but with all the nuclei and electrons of the opposing molecule omitted. This calculation produces a molecule with orbitals having a high resolution, similar to that of the overlapping orbitals in the original ab intio calculation. Subtracting these energies from the original single molecule energies screen outs the superposition error inherent in the $A\cdot B$ cluster.

References

1. Hehre, W.J., Radom, Leo, Schleyer, Paul v.R., and Pople, John A., *Ab Initio Molecular Orbital Theory*. 1986: John-Wiley.

2. Boys, S.F., *Electronic wave functions I. A general method of the calculation for the stationary states of any molecular system.* Proc.. Roy. Soc., 1950. **A200**: p. 542-554.

3. Slater, J.C., *The Theory of Complex Spectra.* Phys. Rev., 1929. **34**: p. 1293-1322.
4. Roothann, C.C.J., *New Developments in Molecular Orbital Theory.* Rev. Mod. Phys., 1951. **23**(2): p. 69-89.

5. Hall, G.G., *The molecular orbital theory of Chemical Valency. VIII. A Method of Calculating Ionization Potentials.* Proc. Roy. Soc., 1951. **A205**(1083): p. 541-552.
6. Sleijpen, G.L.G., Booten, Albert G.L, Fokkema, Diederik R., and van der Vorst, Henk. A, *Jacobi-Davidson Type Methods for Generalized Eigenproblems and Polynomial Eigenproblems: Part I.* BIT, 1996. **36**(3): p. 595-630.

7. Press, W.H., Flannery, Brian P., Teukolsky, Saul A., and William T. Vetterling, *Numerical Recipes in FORTRAN 77*. 2nd ed. 1992: Cambridge University Press.
8. Argaman, N., and Makov, Guy, *Density functional theory: An introduction.* American Journal of Physics, 2000. **68**(1): p. 69-79.

9. Kohn, W., and Sham, Lu Jeu, *Self-consistent equations including echange and correlation effects.* Phys. Rev., 1965. **140**: p. A1133-A1138.

10. Møller, C., and Plesset, M.S., *Note on an Approximation Treatment for Many-Electron Systems.* Phys. Rev., 1934. **46**: p. 618-622.

11. Mulliken, R.S., *Electronic Population Analysis on LCAO-MO Molecular Wave Functions.* J. Chem. Phys., 1955. **23**(1841): p. 1833, 1841, 2338, 2343.

12. Simon, S., Draun, Miquel, and Dannenberg, J.J., *How does basis set superposition error change the potential surfaces for hydrogen-bonded dimers?* J. Chem. Phys., 1996. **105**(24): p. 11024-11031.

APPENDIX B

FUNDAMENTAL TOOLS FOR BULK MD SIMULATIONS

Ewald Summation

This section is largely adapted from section Frenkel and Smit, section 12.1[1], for a more rigorous, treatment of Ewald summations, that section may be consulted.

Many intermolecular interactions can be calculated easily and efficiently by applying a simple, finite cutoff radius, beyond which interactions are assumed to be zero. This is a suitable assumption for many types of interactions, as they decay rapidly with respect to r_{ij}. However, this does not apply to Coulombic interactions, which decay on the order of $1/r_{ij}$. Applying a simple cutoff to these type interactions is almost always insufficient. Therefore, a special technique that considers interactions in periodic images is required to treat these situations. For an *N* particle, periodic system, the electrostatic potential for ion *i* can be described in the following fashion

$$\phi(\mathbf{r}_i) = \sum_j \sum_{\mathbf{n}} \frac{q_j}{\left|\mathbf{r}_{ij} + \mathbf{n}L\right|} \tag{B.1}$$

where q_j is the charge of atom *j,* **n** is the unit vector describing the period image, and *L* is the MD unit cell length. Note that equation 1 does not apply when $j = i$ and $\mathbf{n} = \mathbf{0}$. While equation 1 is theoretically sound, it exhibits poor convergence and is unsuitable for the use in MD simulations. Applying a screening, diffuse opposing charge leads to a calculation that decays much more rapidly with respect to $\mathbf{r}_{ij}$. In turn, the screening

function must be accounted for, so an additional set of diffuse functions are added to offset the effect of the screening function. Figure B.1 shows the form of the point charges in terms of the rapidly decaying, screened and diffuse functions.

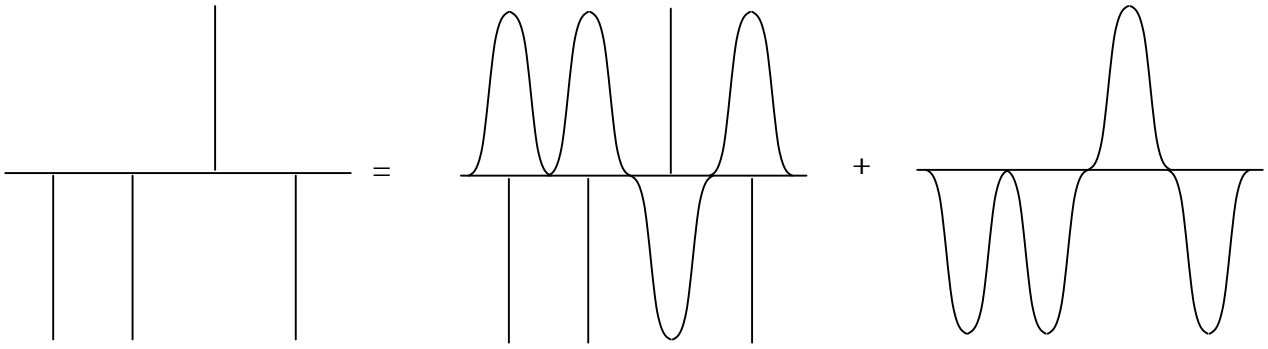

Figure B.1: Diffuse charge representation of point charges

Therefore, a quickly decaying, long range electrostatic calculation will consist of three contributions: the point charge due to q_j, the screening, diffuse charge of $-q_j$, and the compensating cloud charge of q_j. The diffuse electron clouds will be defined by the density function, $\rho_{Gauss}(r)$,

$$\rho_{Gauss}(r) = -q_j\left(\frac{\alpha}{\pi}\right)^{3/2}\exp^{\left(-\alpha r^2\right)} \qquad \text{(B.2)}$$

where α is a constant, which typically is correlated with the MD cell size, and is chosen in a way that optimizes computational efficiency.

Fourier Contribution to Ewald Sum

The inherent problem in the Ewald summation is the solution of the Poisson equation, which defines the charge distribution in terms of the potential

$$-\nabla^2\phi(\mathbf{r}) = 4\pi\rho(\mathbf{r}) \tag{B.3}$$

noting that the Fourier transform of the potential and charge density over *N* particles in a periodic box take the following forms

$$\phi(\mathbf{r}) = \frac{1}{V}\sum_{\mathbf{l}=-\infty}^{\infty}\tilde{\phi}(\mathbf{k})\exp^{-i\mathbf{k}\cdot l} \tag{B.4}$$

$$\rho(\mathbf{r}) = \frac{1}{V}\sum_{\mathbf{k}}\tilde{\rho}(\mathbf{k})\exp^{i\mathbf{r}\cdot\mathbf{k}} \tag{B.5}$$

where $\mathbf{k} = (2\pi/L)\mathbf{l}$ and $\mathbf{l}$ is the periodic lattice vector (l_x,l_y,l_z). In Fourier space, equation 3 takes a much more explicit form.

$$-\nabla^2\phi(\mathbf{r}) = -\nabla^2\left(\frac{1}{V}\sum_{\mathbf{k}}\tilde{\phi}(\mathbf{k})\exp^{i\mathbf{r}\cdot\mathbf{k}}\right) = \frac{1}{V}\sum_{\mathbf{k}}k^2\tilde{\phi}(\mathbf{k})\exp^{i\mathbf{r}\cdot\mathbf{k}} \tag{B.6}$$

If equations 5 and 6 are substituted into equation 3, the following equality is produced

$$k^2\tilde{\phi}(\mathbf{k}) = 4\pi\tilde{\rho}(\mathbf{k}) \tag{B.7}$$

where, for a point charge, the right side of the equation is simply the charge of the ion at the center of the cloud. Therefore, the solution for the Poisson equation for a point charge is,

$$\tilde{\phi}(k) = \frac{4\pi z}{k^2} \tag{B.8}$$

alternatively, when taken as a diffuse electron cloud and summed over all periodic images, the right-hand side of equation 5 takes the form

$$4\pi\tilde{\rho}(\mathbf{k}) = 4\pi\sum_{i=1}^{N}q_i\exp^{-i\mathbf{k}\cdot\mathbf{r}_i}\exp^{\left(-k^2/4\alpha\right)} \tag{B.9}$$

and finally,

$$\tilde{\phi}(\mathbf{k}) = \frac{4\pi}{k^2}\sum_{i=1}^{N} q_i \exp^{-i\mathbf{k}\cdot\mathbf{r}_i} \exp^{\left(-k^2/4\alpha\right)} \tag{B.10}$$

where the expression only holds for $\mathbf{k} \neq \mathbf{0}$. Noting that the potential energy between two particles is

$$U_1 = \frac{1}{2}\sum_i q_i \phi_i(\mathbf{r}) \tag{B.11}$$

the Fourier term can be expressed by utilizing the various equations derived thusfar to produce the potential energy in its final state.

$$U_F = \frac{1}{2}\sum_i q_i \phi_i(\mathbf{r}) = \frac{1}{2V}\sum_{\mathbf{k}\neq 0} \frac{4\pi}{k^2} \left| \sum_{i=1}^{N} q_i \exp^{(i\mathbf{k}\cdot\mathbf{r}_i)} \right|^2 \exp^{\left(-k^2/4\alpha\right)} \tag{B.12}$$

Correction for self-interaction

Equation 12 constants a term that calculates the interaction between charge q_i, and it's own electron cloud, which is an unrealistic consequence of the formulation. To account for this, the self-interaction term must be subtracted from both the real space and Fourier space terms in the Ewald summation. This correction can be solved by simply integrating the Poisson equation in polar coordinates

$$-\frac{1}{r}\frac{\partial^2 r\phi_{Gauss}(r)}{\partial r^2} = 4\pi\rho_{Gauss}(r) \tag{B.13}$$

$$-\frac{\partial r\phi_{Gauss}(r)}{\partial r} = \int_{\infty}^{r} dr 4\pi\rho_{Gauss} = -2q_i\left(\frac{\alpha}{\pi}\right)^{1/2} \exp^{\left(-\alpha r^2\right)} \tag{B.14}$$

$$\phi_{Gauss} = 2\frac{q_i}{r}\left(\frac{\alpha}{\pi}\right)^{1/2} \int_0^r dr \exp^{\left(-\alpha r^2\right)} = \frac{q_i}{r} erf\left(\sqrt{\alpha} r\right) \tag{B.15}$$

And then simply taking the self-correction term as eqn 15 at r = 0.

$$\phi_{Gauss}(r=0) = 2q_i\left(\frac{\alpha}{\pi}\right)^{1/2} \tag{B.16}$$

By combining equations 11 and 16, the self correction tern can be quantified.

$$U_{self} = \left(\frac{\alpha}{\pi}\right)^{1/2}\sum_{i=1}^{N} q_i^2 \tag{B.17}$$

Real space term

Finally, the interactions due to the point charges with oppositely charged, diffuse screening charges must be calculated. The short-ranged potential can be expressed simply as the point-point electrostatic potential subtracted by the same potential in diffuse terms, as defined by equation 15

$$\phi_{short-range} = \frac{q_i}{r} - \frac{q_i}{r}erf\left(\sqrt{\alpha}r\right) \tag{B.18}$$

therefore

$$U_{short-range} = \frac{1}{2}\sum_{i\neq j}^{N}\frac{q_i q_j}{r_{ij}}erfc\left(\sqrt{\alpha}r_{ij}\right) \tag{B.19}$$

and finally, the total Ewald potential energy is defined as.

$$U_{Coul} = U_F - U_{self} + U_{short-ranged} \tag{B.20}$$

<u>Nosé-Hoover thermostat/barostat</u>

In order to control the temperature and pressure in the MD simulations in this work, a Nosé-Hoover thermostat/barostat was employed[2]. This controller allows the

system temperature and pressure to be held constant, allowing the simulation box vary in size. This is accomplished by damping the equations of motion with temperature and pressure friction coefficients, χ and η, respectively. The equations of motion are modified thusly

$$\frac{d\mathbf{r}(t)}{dt} = \mathbf{v}(t) + \eta(t)\left(\mathbf{r}(t) - \mathbf{R}_o\right) \tag{B.21}$$

$$\frac{d\mathbf{v}(t)}{dt} = \frac{\mathbf{F}(t)}{m} - \left[\chi(t) + \eta(t)\right]\mathbf{v}(t) \tag{B.22}$$

where $\mathbf{R_o}$ is the center of mass for the system. The friction coefficients and volume fluctuation are defined by further differential equation

$$\frac{d\chi(t)}{dt} = \frac{1}{\tau_T^2}\left(\frac{\mathsf{T}}{T_{ext}} - 1\right) \tag{B.23}$$

$$\frac{d\eta(t)}{dt} = \frac{1}{\mathsf{N}\, k_B T_{ext} \tau_P^2} V(t)(\mathsf{P} - P_{ext}) \tag{B.24}$$

$$\frac{dV(t)}{dt} = \left[3\eta(t)\right]V(t) \tag{B.25}$$

Where N is the number of particles in the system, T is the dynamic system temperature, P is the dynamic system pressure, T_{ext} is the temperature of the external bath, P_{ext} is the pressure of the external bath, and τ_T and τ_P are the temperature and pressure control constants, which are in units of time and typically have values ~1ps. Obviously, many of

the equations are coupled, therefore, several iterations of each must be performed to reach self-consistency.

References

1. Frenkel, D., and Smit, Berend, *Understanding Molecular Simulations: From Algorithms to Applications*. Computational Science Series. Vol. 1. 2002: Academic Press.

2. Melchionna, S., Ciccotti, Giovanni, Holian, Brad Lee, *Hoover NPT dynamics for systems varying in shape and size*. Molecular Physics, 1993. **78**(3): p. 533-544.

APPENDIX C

$C_{60}(OH)_{32}$ OPTIMIZED STRUCTURE

Please contact patrickredmill@gmail.com for a text-based copy of this optimization.

```
124

   C    -1.26296111    -2.81191787    -1.01780165
   C    -2.39996446     1.76156920    -2.70085471
   C     2.86455579     2.84669315    -0.13560048
   C     1.84943060     3.51780838     0.92175019
   C     2.01026425     2.61594509    -1.34849440
   C     0.00769228     1.82650737    -3.09990458
   C     2.10926968    -1.41975543     1.96782073
   C    -2.20356200    -2.28838794    -0.14063185
   C     3.10710249     0.49846804    -2.00891278
   C     1.53342458    -0.11855550    -3.82508208
   C     1.36658223    -3.06367829    -2.41736881
   C    -3.02726316     2.26570624     0.34738565
   C    -2.14274054    -2.91265332     1.21227344
   C    -0.39793257    -3.85725789    -0.41680970
   C    -1.73387598     3.05216313    -1.95730952
   C     1.51026082    -2.49096149     1.31395803
   C     0.53675837     3.97015407    -0.01001574
   C    -2.76808862    -0.60040482    -1.74619998
   C     3.41972050     0.79297177     1.71174938
   C     0.75618011     3.20032079    -1.26939691
   C    -0.25707309     2.80628396    -2.13314924
   C    -2.01692615     1.70781980     1.28085242
   C     2.78024942    -0.67721204    -2.95087207
   C    -1.81732443    -1.12080357    -2.61283237
   C     2.64363806    -2.09410569    -2.18451815
   C    -0.74106152    -3.71081280     1.19746591
   C     3.25045627    -0.83586108    -0.05028079
   C     0.18794242     2.03703098     2.12894223
   C    -1.19133884     1.05457270    -3.33034260
   C    -3.80060918    -0.37496602     0.40901183
   C     3.54642794     0.39068429    -0.73977681
   C     0.21282334    -1.01303707    -3.94890400
   C     0.11334685    -2.45543495    -3.15827318
   C    -3.82024893     1.10903696    -0.37220345
   C     0.44513329    -3.15582575     2.11734702
   C     2.45960316     1.46357072     2.75115924
   C    -2.09303309     0.51203418     1.95445867
   C     0.10509120     0.83650774     2.80457690
   C    -2.96943351    -1.19395317    -0.51503670
   C     0.15479145    -2.09002154     3.28978015
   C     1.52258961    -1.12765435     3.29871321
   C     2.26412532     1.63372473    -2.31490216
   C    -2.15647988     3.38112284    -0.47918632
   C     1.08462231    -3.69053579    -0.89648617
   C     1.26538915     1.23674624    -3.20065339
   C    -2.46527032    -1.86936530     2.36237296
   C     1.79933983    -2.73433741    -0.01766182
   C    -0.90453154     3.69816899     0.55467162
   C     2.96528060    -0.57594619     1.28865655
   C    -1.22438632    -1.31487058     3.22889993
   C     1.36187318     0.43081296     3.46260630
   C    -1.02704855     0.06146018     2.70255408
   C    -0.87962764     2.47854633     1.38578616
   C     2.65746028    -1.90584854    -0.70360080
   C    -3.19861636    -0.45764035     1.85078719
   C     3.69835519     1.52925479     0.27486691
   C    -3.37106364     0.76290453    -1.87928966
   C    -1.05497169    -2.23078053    -2.24807758
   C     1.51692316     2.68911718     2.23080987
   C    -1.05195695    -0.27643258    -3.49204680
   O    -0.30868484    -3.40996666    -4.18401060
```

```
H     0.38545569    -4.11270277    -4.21620950
O     0.08265217    -1.30413600    -5.36424151
H    -0.21891158    -2.24900625    -5.41665372
O     2.05413452     0.07953395    -5.17085013
H     1.44601052    -0.41142569    -5.78081050
O     3.89856333    -0.84351855    -3.86080179
H     3.59515033    -0.48645473    -4.73570763
O     3.80251422    -2.89461577    -2.56010410
H     4.28832096    -2.37235482    -3.24774795
O     1.79461479    -4.14096150    -3.25771982
H     2.77039326    -4.22566598    -3.13730543
O    -1.03914866    -5.05077794     1.65800029
H    -0.26816266    -5.31853850     2.22948865
O    -3.20821647    -3.92420115     1.29607881
H    -2.77421178    -4.77769857     1.52572959
O    -3.33589727    -2.51115688     3.29739009
H    -3.77946431    -3.25045442     2.81728704
O    -1.67234068    -1.26555860     4.62615941
H    -2.61979493    -1.53009596     4.64120899
O     0.17925193    -2.82767368     4.53207326
H    -0.57014846    -2.45230628     5.07705388
O     1.00042290    -4.35377803     2.77326507
H     0.88350958    -4.22384748     3.74378180
O     4.73993418     0.65442715     2.32822805
H     4.69842419     1.11011905     3.20206790
O     5.08889910     1.94354212     0.27748547
H     5.50048627     1.50854857     1.06972035
O     3.85537856     3.89071398    -0.41697120
H     4.74483067     3.46559261    -0.29609615
O     2.46357594     4.75434502     1.36208364
H     3.31175968     4.82720900     0.83504215
O     1.48318332     3.62453786     3.35020546
H     1.88421337     4.46570545     3.03674222
O     3.31863455     1.98052161     3.76930975
H     2.79329662     2.63404216     4.28095171
O    -2.96416319     4.55657497    -0.58360660
H    -3.47161852     4.62921383     0.25467617
O    -2.08721520     4.19885367    -2.79914684
H    -2.56490807     4.84167345    -2.22210055
O    -3.21812615     2.27365445    -3.78569296
H    -3.01579298     3.24504903    -3.84169767
O    -4.62328900     0.69038344    -2.63433453
H    -4.49730847     1.27044225    -3.43061269
O    -5.20780393     1.51410336    -0.42424574
H    -5.48313152     1.38220599    -1.37643832
O    -3.98606024     3.04836835     1.11945537
H    -4.88431904     2.78828834     0.81679704
O     1.30889359     0.74402992     4.85976116
H     1.96992036     0.16110673     5.29155239
O     2.37176863    -1.57184117     4.38342711
H     1.86543221    -2.24511953     4.89158837
O    -5.15861487    -0.85763289     0.49024697
H    -5.74096924    -0.10912499     0.22552288
O    -4.20605908    -0.10091187     2.80431666
H    -5.01450915    -0.59496755     2.55760345
O     1.74734786    -4.95699422    -0.80475532
H     1.13416775    -5.61768697    -1.18934569
O    -0.82342357    -5.17353402    -0.85336664
H    -1.06508274    -5.68021344    -0.04598821
O     0.62434690     5.39517525    -0.24375022
H     1.37343159     5.72587722     0.30459333
O    -1.28777431     4.81334394     1.37396671
H    -0.95074384     5.61165244     0.91178787
```

APPENDIX D

SAMPLE INPUT FILES

DL_POLY TI input files

CONTROL

```
CONTROL file generated by DL_POLY/java utility

temperature      298.15
pressure         0.0010
ensemble npt hoover   1.0000  1.0000

steps           600000
equilibration   100000
scale              1000
print              1000
stack               100
stats               500
trajectory      100000    5000       2
rdf                  10

timestep         0.002
cutoff           10.0000
delr width       0.5000
rvdw cutoff      10.0000
ewald precision   1e-4

shake tolerance  1.0E-5

quaternion tolerance  1.0E-5

print rdf



job time              3000000.

close time            200.00



finish
```

FIELD

```
Thin Nanotube
UNITS kcal
MOLECULES 2
B_S model of C60/water
NUMMOLS 1
ATOMS     180
       C  12.0110000  0.00000000  180    1
FINISH
Water
NUMMOLS 2989
ATOMS 3
       O     15.9994   -0.8476
       H       1.008    0.4238
       H       1.008    0.4238
RIGID 1
    3    1    2    3
FINISH
vdw 3
       O       O  lj       0.1553      3.1660
       C       C  lj       0.0951       3.473
       C       O tab       0.0747      3.1900
CLOSE
```

NWChem supermolecule input files

```
start POSS_water
title "POSS/water cluster optimization, ab initio, mp2"
#
geometry
    Si    -0.16327260    -2.04700048    -1.60954640
    Si    -0.16407861    -2.04472470     1.61238725
    Si     2.30410473     0.10755092     1.61797242
    Si     2.30498950     0.10537713    -1.61665501
    Si     0.16327721     2.54933013    -1.63240353
    Si    -2.30109164     0.42538701    -1.62035249
    Si    -2.30198496     0.42772814     1.61867409
    Si     0.16230701     2.55159619     1.62917205
    O      1.45038997     1.51831397     1.93061536
    O     -1.25570550     1.70245288     1.92523318
    O     -1.45132738    -1.00022320     1.85493426
    O      1.24856624    -1.17860864     1.83681341
    O      2.75114539     0.11959829     0.00076863
    O      1.24918247    -1.18069918    -1.83452726
    O     -0.21671652    -2.57676706     0.00180012
    O      0.19050003     2.94451469    -0.00187319
    O      1.45171385     1.51589923    -1.93174784
```

```
    O     -2.73744063     0.49053850    -0.00099253
    O     -1.45065724    -1.00308971    -1.85415272
    O     -1.25453390     1.69964546    -1.92784078
    H     -3.48399206     0.49050534     2.48667880
    H      0.24213624     3.75431844     2.46675196
    H      3.47653631    -0.00769437     2.49294052
    H     -0.24242674    -3.20159477     2.51258680
    H     -0.24078502    -3.20508361    -2.50821812
    H     -3.48258121     0.48715847    -2.48913504
    H      3.47793574    -0.01125959    -2.49074865
    H      0.24335279     3.75088313    -2.47163952
    O      0.10336203    -5.62612358     0.00076949
    H     -0.06998096    -4.66744737     0.00163935
    H     -0.72591336    -6.12853337     0.00393440
end
basis
Si library 6-311++G(2d,2p)
O library 6-311++G**
C library 6-311++G**
H library 6-311++G**
bqO library O 6-311++G**
bqC library C 6-311++G**
bqH library H 6-311++G**
bqSi library Si 6-311++G(2d,2p)
end
bsse
mon first  1 2 3 4 5 6 7 8 9 10 11 12 13 14 15 16 17 18 19
20 21 22 23 24 25 26 27 28
mon second 29 30 31
end
mp2
   tight
   scratchdisk 512
end
task mp2 energy
```

LAMMPS lipid bilayer input file

```
# 288 DPPC molecules in 3655 SPC water molecules

units          real
atom_style     full

pair_style  hybrid   lj/expand   2.0     lj/charmm/coul/long  8.0  10.0
bond_style     harmonic
angle_style    charmm
dihedral_style charmm
improper_style harmonic
kspace_style   ewald  0.01

read_restart   save.dppc288

group bead type 13
group c60  type 14

restart  100000 save.dppc288

pair_coeff      1       1     lj/charmm/coul/long              0.07     3.563594873
pair_coeff      2       2     lj/charmm/coul/long              0.12     3.029055642
pair_coeff      3       3     lj/charmm/coul/long             0.055     3.875409424
pair_coeff      4       4     lj/charmm/coul/long             0.022     2.351972616
pair_coeff      5       5     lj/charmm/coul/long              0.08     3.670502719
pair_coeff      6       6     lj/charmm/coul/long               0.2     3.296325257
pair_coeff      7       7     lj/charmm/coul/long             0.585     3.830864488
pair_coeff      8       8     lj/charmm/coul/long              0.12     3.029055642
pair_coeff      9       9     lj/charmm/coul/long            0.1521     3.153781462
pair_coeff      10     10     lj/charmm/coul/long              0.02     4.053589168
pair_coeff      11     11     lj/charmm/coul/long        0.15210298     3.160610000
pair_coeff      12     12     lj/charmm/coul/long                 0             0.0
pair_coeff      13     13     lj/charmm/coul/long              0.00             0.0
pair_coeff      14     14     lj/charmm/coul/long              0.07     3.550053212


neighbor       2.0  bin

timestep    1.0

thermo_style   multi
thermo         1000

fix            1   all   shake   0.0001   10   100   b    15   17   a   30   31   32
fix            2   all   npt  298.15 298.15 1000  aniso   NULL  NULL  NULL  NULL  1.0
1.0  1000
fix            3   all   temp/rescale  100   298.15   298.15   2   0.75
fix            4   bead  setforce  NULL   NULL   0

#dump           1   all   custom 2000   dump.dppc288 tag type  q   x   y   z

run           1000000

unfix         3

dump           1   all   custom 10000   dump.dppc288 tag type  q   x   y   z   fx  fy  fz
dump           2   c60   custom 100     dump.forces  tag type  z  fz
run          1000000
```